The spatial landscape of progression and immunoediting in primary melanoma at single cell resolution

Ajit J. Nirmal[1,2,3†], Zoltan Maliga[1,2†], Tuulia Vallius[1,2†], Brian Quattrochi[4], Alyce A. Chen[1,2], Connor A. Jacobson[1,2], Roxanne J. Pelletier[1,2], Clarence Yapp[1,2], Raquel Arias-Camison[1,2,4], Yu-An Chen[1,2], Christine G. Lian[4], George F. Murphy[4], Sandro Santagata*,[1,2,4] and Peter K. Sorger[1,2,5]*

[†]These authors contributed equally

*These authors contributed equally

Human Tumor Atlas Network

[1]Laboratory of Systems Pharmacology, Harvard Medical School, Boston, MA, 02115, USA.

[2]Ludwig Center at Harvard, Boston, MA, 02115, USA.

[3]Department of Medical Oncology, Dana-Farber Cancer Institute, 450 Brookline Avenue, Boston, MA 02215, USA.

[4]Department of Pathology, Brigham and Women's Hospital, Harvard Medical School, 75 Francis Street, Boston, MA 02115, USA.

[5]Department of Systems Biology, Harvard Medical School, 200 Longwood Avenue, Boston, MA 02115, USA.

**Correspondence: peter_sorger@hms.harvard.edu*

Keywords
Melanoma, tumor microenvironment, tumor evolution, immune suppression, tumor-stromal crosstalk, spatial tumor heterogeneity, multiplex imaging, spatial proteomics, spatial transcriptomics, subcellular

Highlights

- Multiplexed single-cell atlas combines imaging and micro-region RNA sequencing
- Evidence of functional interactions from high-resolution imaging of immune synapses
- PDL1-mediated CTL suppression is dominated by myeloid not tumor cells
- Highly localized domains of immunoediting and immune suppression co-exist

SUMMARY

Cutaneous melanoma is a highly immunogenic disease, surgically curable at early stages, but life-threatening when metastatic. Here we integrate high-plex imaging, 3D high-resolution microscopy, and spatially-resolved micro-region transcriptomics to study immune evasion and immunoediting in primary melanoma. We find that recurrent cellular neighborhoods involving tumor, immune, and stromal cells change significantly along a progression axis from precursor states to melanoma *in situ* to invasive tumor. Hallmarks of immunosuppression are detectable by the precursor stage, and when tumors become locally invasive, a consolidated and spatially restricted suppressive environment forms along the tumor-stromal boundary. This environment is established by cytokine gradients that promote expression of MHC-II and IDO1 and by PDL1-expressing macrophages and dendritic cells engaging activated T cells. However, a few mm away, T cells synapse with melanoma cells in fields of tumor regression. Thus, invasion and immunoediting can co-exist within a few millimeters of each other in a single specimen.

INTRODUCTION

Cancer progression commonly involves a progressive failure of the immune system, particularly T cells, to detect tumor cells as they accumulate mutations that promote growth, invasive phenotypes, and metastatic capabilities (Swann and Smyth, 2007). The competition between cancer and the immune system generates a complex cellular ecosystem within a tumor. The physiologic states and physical relationships of tumor and stromal cells determine disease outcomes and responsiveness to therapy (O'Donnell et al., 2019). A prominent example of these phenomena is found in sun-damaged skin, which is subject to a high mutational burden but also contains abundant immune cells. Interactions between melanoma cells and both skin-resident and circulating immune cells strongly influence tumor initiation and progression. The importance of the immune system in restraining malignant cutaneous melanomas is demonstrated, in part, by the success of anti-PD1 and anti-CTLA4 immunotherapies in both metastatic and adjuvant settings (Larkin et al., 2015, 2019).

DNA sequencing has helped to define mutations in genes such as BRAF, NRAS, PTEN, and TP53 that accompany melanoma progression (Hodis et al., 2012; Lian and Murphy, 2016; Shain et al., 2015), and dissociative single-cell RNA sequencing (scRNA-Seq) has identified progression-associated tumor cell states (Tirosh et al., 2016). However, cells in morphologically normal skin also have a high mutational burden, estimated in Caucasians to be >100 driver mutations per cm^2 by late middle age (Martincorena et al., 2015), making it difficult to distinguish passenger from driver mutations. Thus,

despite the importance of BRAF mutations in guiding the use of RAF/MEK therapy in a metastatic setting, sequencing assays are of limited diagnostic utility in early melanoma and histopathological assessment of hematoxylin and eosin (H&E) stained formaldehyde fixed paraffin embedded (FFPE) skin biopsies, complemented by immunohistochemistry (IHC), remains the primary means of staging disease (Smoller, 2006).

Normal skin is characterized by evenly spaced melanocytes, which are neural crest-derived melanin-producing cells (Cichorek et al., 2013) located between cuboidal basal keratinocytes on the apical face of the dermal-epidermal junction (Moreci and Lechler, 2020). Fields of melanocytic atypia, the earliest signs of transformation, are characterized by an increase in melanocyte number and density, enlargement, and irregularity of melanocyte nuclei, movement of melanocytes away from the dermal-epidermal junction (Elder, 2006), and loss of 5-hydroxymethylcytosine (5hmC) epigenetic marks (Lian and Murphy, 2016; Lian et al., 2012). These precursor fields can develop into melanoma *in situ* (MIS), a proliferation and confluence of malignant melanocytes within the epidermis but without invasion into the underlying dermis (Higgins et al., 2015). MIS can spread within the epidermis and focally invade the superficial dermis without either mitotic activity or expansile growth (giving rise to radial growth phase melanoma) and has an excellent prognosis upon complete excision. However, invasive growth into the dermis that is both expansile and mitotically active (vertical growth phase melanoma) is potentially lethal (Guerry et al., 1993). Vertical growth phase melanomas can be endophytic or exophytic (corresponding to vertical growth down into the dermis or upwards above the skin), at times resulting in clinically polypoid lesions (Hikawa et al., 2014).

Because localized primary melanoma can be cured by relatively minor surgery, removal of dysplastic nevi with higher grades of atypia is standard clinical practice (Bergman et al., 1997). However, the majority of primary cutaneous melanomas are not thought to derive from nevi (Damsky and Bosenberg, 2017) and the precise sequence of genetic events and immunosuppressive features that occur during progression from precursor lesions to invasive melanoma remains unknown. In addition to the standard Tumor-Node-Metastasis (TNM) system used for melanoma staging (Keung and Gershenwald, 2018) the depth of tumor invasion into the dermis (Breslow thickness) is a particularly critical parameter (Swetter et al., 2019). The number and location of tumor-infiltrating lymphocytes (TILs) also have prognostic value (Fu et al., 2019). The Clark scoring system recognizes three distinct patterns for TILs: absent, non-brisk, and brisk (Mihm and Mulé, 2015). Absent describes both the absence of TILs and their failure to infiltrate tumor; non-brisk describes the restriction of TILs to scattered foci in the vicinity of the tumor; and brisk describes infiltration throughout vertical growth

phase tumors or widely distributed along the invasive tumor front (Maibach et al., 2020). The greater the TIL number, and the brisker the response, the more favorable the prognosis (Clark et al., 1989; Thomas et al., 2013). In some tumors, regions of inflammatory regression are observed in which T cells are actively eradicating malignant melanocytes, leading to fields of fibrosis, vascular proliferation, and pigment incontinence indicative of terminal regression (Aung et al., 2017). Inflammatory regression represents an example of successful and ongoing immunoediting and generates fields of terminal regression in which tumor cells are absent.

The great majority of studies on immune surveillance in primary and metastatic melanoma have involved histologic analysis of H&E or IHC images, which are restricted to one to three markers per section, or sequencing of genomic mutations or mRNA in bulk tumor or single cells. However, several recent studies have demonstrated the potential for multiplexed imaging to provide greater insight into spatially restricted tumor and immune programs in melanomas at different stages (Bosisio et al., 2020; Fattore et al., 2019). In the current work, we focus on the identification of molecular, cell state, and morphological features that are significantly associated with histologic characteristics used to diagnose and stage melanoma and determine treatment strategy. We used specimens where early precursor stages as well as regions of inflammatory regression (which are often incidental to diagnosis(and of unknown prognostic significance (Guitart et al., 2002) were intimately associated with zones of evolving melanoma, thus providing insight into tumor evolution and immune editing. This was accomplished by histology review of specimens in the Brigham and Women's Hospital dermatopathology tissue bank using H&E-stained tissue sections complemented in some cases by IHC.

The spatial organization of the tumor microenvironment (TME) was analyzed using both conventional and high-resolution (wide-field deconvolution) 20 to 30-plex fluorescence microscopy (CyCIF) (Lin et al., 2018) in combination with transcriptional profiling of selected micro-regions using micro-region transcriptomics (mrSEQ: GeoMx and PickSeq) (Demirkan et al., 2020; Maliga et al., 2021). The resulting molecular and morphological data were then analyzed with respect to histopathology annotations. CyCIF and H&E imaging were performed on whole slides, not tissue microarrays (TMAs) or small fields of view (FOVs) (Baharlou et al., 2019), to preserve the spatial relationships of different histologies and to provide sufficient statistical power (Lin et al., 2021). Multiple computational approaches were used to analyze the resulting data. Differential expression analysis and unsupervised clustering of mrSEQ data - which quantified 1,800-4,000 genes per micro-region of interest (mROI – a 40-200 μm diameter region extracted for sequencing) - revealed genes and pathways enriched in specific disease stages. Clustering of single-cell CyCIF data (in some cases, using

multiple panels on serial sections) provided insight into correlated changes in tumor and immune states. Spatial lag analysis (Rey, 2001) made it possible to identify subtle differences among tumor cells in a single patient with respect to location and state whereas Latent Dirichlet Allocation (LDA) (Jackson et al., 2020; Valle et al., 2014) enabled the assembly of a single spatial model encompassing cells of different types (tumor, stromal and immune subsets) across all patients. Using these methods, we identified recurrent differences in the TME with disease progression and found large differences between precursor and MIS fields in which they arose as well as more limited differences between MIS and invasive melanoma. Effective immune editing by activated T cells was observed in regions of inflammatory regression adjacent to areas of PDL1-mediated T-cell suppression by myeloid cells and near-complete immune exclusion from invasive melanoma. This demonstrates that immunosuppressive niches are highly localized, in some cases only a few cells thick. Within these niches, high-resolution imaging demonstrates direct cell-to-cell contact and polarized receptor-ligand interactions, confirming cytotoxic T cell function in some cases and T cell suppression in others.

RESULTS

Multimodal profiling of spatially distinct regions within cutaneous melanoma

Fixed (FFPE) specimens of primary cutaneous melanoma from 11 patients, one locoregional metastasis, and one distant skin metastasis (for comparison) were selected based on having multiple histologic features associated with cancer initiation, progression, and immune surveillance (specimens MEL1 to MEL13; **Tables S1 and S2**). Analysis of H&E specimens by board-certified dermatopathologists confirmed the presence of two to five distinct, spatially separated tumor and immune environments comprising precursor fields, melanoma in situ and invasive melanoma as well as active immune editing ~5 -20 mm apart from each other (summarized in **Figure S1A**). To obtain molecular data on these specimens, serial sections (5 µm thick) were subjected to whole slide, subcellular-resolution, 20-30 plex CyCIF, and 70 tissue regions having distinctive morphologies or locations were annotated (hereafter histological ROIs; average 5.5 per specimen; **Figures 1A-1C, S1A, Table S3**).

Serial sections were stained with different combinations of antibodies to generate overlapping but complementary sets of data (**Table S4**). Labeling of keratinocytes in the epidermis was performed with antibodies against pan-cytokeratin (panCK); of normal melanocytes, atypical melanocytes, and tumor cells with antibodies against SOX10 and MITF (supplemented with antibodies against 5hmC and other progression markers) (**Figure S1B**); and of stromal cells and vasculature with antibodies against

smooth muscle actin (αSMA) and CD31. Immune cells were imaged and identified using a variety of lineage-specific cell surface proteins and functional markers (e.g., PD1) as described in **Figure S1C, Tables S5, and S6**. Whereas lineage markers such as CD4, CD8, CD163, SOX10, etc., could reliably be binarized into positive and negative states, enabling hierarchical clustering to identify cell types (**Figures 1D, S1C**), other markers such as S100B or MITF were observed to vary continuously in expression over the dataset and different computational methods (e.g., spatial lag) were used for quantification. Cell types were then mapped back to their positions in the tissue for spatial analysis (**Figures 1E-1F).**

Spatial correlation, proximity analysis, and similar methods have been widely used to identify cells sufficiently close to each other to make contact (Stoltzfus et al., 2020). However, these methods do not reveal whether contacts have functional consequences. The formation of immune synapses and the resulting polarization of vesicle trafficking and receptor-ligand interaction (Calvo and Izquierdo, 2018) have been extensively analyzed using fluorescence microscopy, primarily in tissue culture conditions. To look for functional interactions between cells in microanatomically intact tissues, we used 3D CyCIF imaging at a resolution sufficient to localize cell surface receptors and ligands (~220 nm laterally, with optical deconvolution; **Figures 1C and S1D-S1G)**. For example, **Figures 1G** and **H** show a $SOX10^+$ tumor cell in contact with two $CD8^+$ cytotoxic T lymphocytes (CTLs) and one $CD4^+$ regulatory T cell (Treg) at different positions along the cell perimeter (the Treg was found to be $FOXP3^+$ in other imaging channels; **Figures S1E-S1F**). Polarization of CD8 (a co-receptor for the T-cell receptor) at the site of contact between the tumor cell and one of the CTLs is consistent with formation of an immune synapse. In this CTL, some TIM3 and LAG3 were partially localized to the synapse, although the majority of these proteins were sorted to the opposite side of the cell (**Figures 1H-I** and **S1H**). TIM3 and LAG3 are co-inhibitory receptors that function to regulate the activity of CTLs (Anderson et al., 2016) and their presence on $PD1^+$ CTLs show that these cells are "terminally exhausted." Focusing on the point contact between the CTL marked with the double asterisk and the tumor cell (orange rectangle in **Figure 1H)**, and using anti-HLA-A to identify relevant membranes, we observed localization of CD8 to the point of contact as well as uniform membrane staining for CD3 and punctate intracellular staining of SOX10 (**Figure 1I**). The distribution of these three proteins along a dashed line perpendicular to the cell-cell contact confirmed that the majority of CD8 (red line in the plot in **Figure 1I**; **Figure S1G** and **S1I**) was found on the membrane of the $CD3^+$ lymphocyte (green line) and approximately 0.5 μm away from the membrane of the adjacent $SOX10^+$ tumor cell. Optical sectioning through the point of contact between the tumor cells and the Treg also revealed an extended contact (**Figures 1J and S1H**) which may be

associated with programming of tolerogenic activity. Elsewhere in this paper we show that polarized interactions between PD1 receptor and PDL1 ligand can also be imaged. High resolution imaging of tissues therefore provides a means of confirming whether cells in proximity to each other make functional contacts.

Micro-regional transcript profiling identifies spatially distinct immune, mitogenic, and survival programs

We performed the most extensive molecular analysis on specimen MEL1, which had the greatest number of distinct histologies (and spanned three tissue blocks MEL1-1, MEL1-2, and MEL1-3) as well as exome sequencing data consented for research purposes. MEL1 was an NF1-mutant, $BRAF^{wt}$ tumor, which is one of four recurrent cutaneous subtypes identifiable in TCGA data (Cirenajwis et al., 2017). MEL1 was characterized with 80 different antibodies on five serial sections using standard CyCIF (~500 nm resolution) and also with 21 antibodies using 3D high-resolution deconvolution microscopy (~100 nm resolution) (Hiraoka et al., 1991). 3D image stacks were collected from a total of 42 FOVs, each 110 x 110 µm, selected to provide details of cellular interactions in regions of tumor regression, MIS, and invasion (**Figure 1C** and **S1D**). Micro-region transcriptomics (mrSEQ) was performed on a total of 292 mROIs using PickSeq, which recovers smaller regions of tissue, and GeoMX, which is commercially available and samples larger tissue regions (Maliga et al., 2021; Zollinger et al., 2020); Key findings were concordant between the two methods, increasing confidence in these recently developed approaches.

Histopathologic annotation of MEL1 using H&E sections demonstrated the presence of a polypoid tumor with three distinct malignant morphologies comprising invasive melanoma (IM), exophytic melanoma (EM), and melanoma in situ (MIS) (**Figure S1A;** histological features and annotations are described in **Table S3**). Polypoid melanoma is a relatively rare variant of a nodular growth pattern with poor long-term survival (Manci et al., 1981). However, the patient from whom MEL1 was excised developed loco-regional recurrence but was alive at the time of last follow-up. The MIS was co-extensive with regions of inflammatory and terminal regression in which immune editing had reduced or eliminated tumor cells (**Figures 1B** and **1C**). A region of invasive disease was found ~20 mm away from the MIS and was observed to project both upward to form the exophytic component and downward to form the nodular component whose invasive boundary (IB) had reached a depth of 4-5 mm and was surrounded by a domain of immune-rich stroma that scored as a brisk TIL (bTIL) response.

A total of 292 mROIs from MEL1 were selected for mrSEQ (222 PickSeq mROIs and 70 GeoMX; **Figure 1B** and **S2A**). PickSeq recovered 5-20 cells per 40 µm mROI and transcript profiling was performed using cDNA sequencing (Maliga et al., 2021); GeoMX recovered ~200 cells per ~200 µm mROI and transcript profiling was performed by hybridization to a panel of ~1,800 cancer-related genes (Zollinger et al., 2020). Principal Component Analysis (PCA) of the resulting data revealed three primary clusters corresponding to (i) MIS, (ii) malignant tumor (EM plus IM), and (iii) regions of active immune response (IR – which was adjacent to the MIS or a bTIL region adjacent to the invasive boundary of the nodular melanoma) (**Figure 2A**). Markers commonly used to detect and subtype malignant melanoma (PMEL, MLANA, TYR, MITF, and CSPG4) were strongly and consistently expressed in mROIs from the invasive tumor, sporadically in MIS and not in immune-rich regions (IR, bTIL) confirming the annotation of these regions (**Figure 2B;** gene names are listed in **Table S6**). Single-sample gene set enrichment analysis (ssGSEA) confirmed high enrichment of melanocyte signatures in tumors but not in immune mROIs, and conversely, immune signatures in IR and bTIL regions. Keratinocyte signatures were enriched in skin adjacent to MIS and IR (**Figure 2C**).

Strong enrichment of interferon-gamma (IFNG or IFN□) related signatures was observed in both immune-rich regions and tumor and mrSEQ data showed that expression of IRF1 was highest in mROIs from the IB (**Figure S2B**). IRF1 is a master regulator of the acute response to IFN□ and can induce PDL1 expression (Murtas et al., 2013); as discussed below, however, PDL1 expression by tumor cells was rare in our dataset. Imaging of IM showed that strong nuclear staining of IRF1 in tumor cells was restricted to a narrow band of cells lying along the invasive boundary (**Figure 2D)**. By integrating intensities across this boundary, we found that the half-maximal width for IRF1 staining was ~40 µm. (**Figure 2E**). Staining for nuclear IRF1 and IRF5 in $CD11C^{+}$ myeloid cells was greater directly adjacent to the tumor boundary than elsewhere in the stroma **(Figure 2D,** lower panels). Moreover, mrSEQ revealed higher expression of IFN□ in bTIL and IB regions than elsewhere (**Figure 2F**). Thus, mrSEQ and imaging are consistent with a paracrine signaling mechanism in which IFN□ arising in the peritumoral stroma (including the bTIL region) activates interferon response elements in tumor and immune cells at the invasive front (Smithy et al., 2017). We show below that the resulting tumor and stromal states, which are spatially restricted to a few cell diameters in width, express immunosuppressive programs.

To identify genes differentially expressed (DE) with tumor progression, we compared mrSEQ data of tumor (EM plus IM) and MIS; this yielded 1,327 DE genes (FDR < 0.05) (**Table S6**). A complicating factor (made clear by imaging) was a substantial difference in cellular composition: EM

and IM contained few immune cells, but MIS was rich in tumor and immune cells and keratinocytes. To correct for this effect, we first searched for a gene shown by imaging and mrSEQ to be present in $SOX10^{+}$ tumor cells from EM and IM but not in MIS and then constructed a correlation-based gene network to identify genes co-expressed with that gene (see STAR methods). The calcium-binding protein S100B, whose serum levels are a diagnostic marker of metastatic melanoma (Hauschild et al., 1999), was found to be an ideal candidate (epidermal Langerhans cells also stain positive for S100B, but they were too infrequent to affect the analysis; **Figure 2G**). The resulting S100B correlation module comprised 35 genes (at r = 0.6) all of which exhibited statistically significant DE between MIS and EM-IM (FDR < 0.05) (**Figures 2H** and **2I; Table S6**). The module included: (i) genes such as SERPINE2 (Wu, 2016), CTSL (Sudhan et al., 2016; Sui et al., 2016), TBC1D7 (Qi et al., 2020), and NRP2 (Moriarty et al., 2016) implicated in metastasis or invasion in diverse cancers; (ii) MITF-regulated genes such as the SCD (Vivas-García et al., 2020) and CDK2 (Du et al., 2004); (iii) oncogenes, such as ETV5, an oncogenic transcription factor in prostate cancer (Jané-Valbuena et al., 2010; Mus et al., 2020). Elevated expression of multiple genes in the S100B module (BRI3, CDK2, MT-ND2, PMEL, SOX10, TBC1D7, TSPAN10, TYR) was associated with lower survival in the TCGA melanoma dataset (P <0.05) (**Figure S2C**). Thus, half of the genes in the S100B module and differentially expressed between MIS and EM-IM have established roles in oncogenesis, invasion or progression in one or more cancers and ~25% are associated with lower survival in melanoma.

Regions of exophytic and endophytic invasive melanoma contained abundant tumor cells with relatively few infiltrating immune or stromal cells, and thus comparing gene expression in these two domains of malignant disease was not complicated by compositional differences. DE analysis showed 81 genes to be upregulated in mROIs from IM and 69 genes to be upregulated in mROIs from EM (FDR < 0.05) (**Figure 2J; Table S6**). These differences represent heterogeneity within a contiguous malignant tumor ~1 cm in diameter. GSEA showed that KRAS signaling was significantly enriched in IM relative to EM as were downstream targets such as NF-κB and MYC (**Figures 2K** and **2L**). Upregulation of the KRAS pathway is expected in a tumor such as MEL1 that is mutant in NF1, which functions as a RAS GTPase-activating protein (GAP) (Cirenajwis et al., 2017). The insulin-like growth factor receptor IGF-1R and the IGF binding protein IGFBP2, which is a mitogenic factor in multiple cancers (Li et al., 2020), were significantly upregulated in EM relative to IM. BCL2A1 (Haq et al., 2013), an antiapoptotic pro-survival member of the BCL2 gene family, was another gene upregulated in IM relative to EM **(Figure 2L**). Genes implicated in an epithelial to mesenchymal transition (EMT) were also differently expressed: the S100A4 metalloproteases, β-catenin, and vimentin (DMKN, MMP2, CTNNB1, and VIM

genes) were upregulated in IM and GSEA analysis confirmed enrichment of an EMT signature within this region (**Figures 2M** and **S2D**). EMT-related genes are known to promote invasion and metastasis in many human neoplasms (Fei et al., 2017), consistent with the observed invasion of this vertically growing melanoma into the underlying dermis. In contrast, the RNA sensing protein DDX58/RIG-I implicated in suppression of cancer migration (Liu et al., 2015) was upregulated in EM ($P < 0.05$) (**Figure S2E**). Thus, even though IM and EM are contiguous and both in the vertical/tumorigenic growth phase, they exhibited significant differences in mitogenic, survival, and signaling pathways; the downward growing component (IM) was also characterized by higher expression of programs associated with invasion and EMT.

To study proliferation in EM and IM, two adjacent FFPE sections were stained with antibodies against four cyclins (A2, B1, D1, E1), five proliferation markers (phosphorylated RB - pRB, KI67, PCNA, MCM2, phosphorylated Histone H3: pHH3) and three members of the p21 family of CDK inhibitors (p21, p27, p57) (**Figures 2N** and **S2F-S2H**) (Gookin et al., 2017). Overall, we found that IM contained ~3-fold more proliferating cells than EM but that atypical cell cycle states similar to those we have observed in other tumors were also present (Gaglia et al., 2021). In IM, ~10% of cells were positive for Cyclin D1, and of these, 25% were positive for KI67 and ~43% were positive for the replication factors MCM2 and PCNA, placing them in G1/S; ~ 6% were positive for the Cyclins A2 and/or B1, placing them in S-G2-M); and ~0.2% were positive for pHH3, placing them in mitosis. This yielded a proliferative fraction of ~17%. In EM, 31% of cells were Cyclin $D1^+$ but of these only 1% were $KI67^+$ and ~10% $PCNA^+$ or $MCM2^+$; ~2% were positive for Cyclins A2 and B1 and 0.01% were $pH3^+$ (**Figure S2G**). Thus, a substantial fraction of the Cyclin $D1^+$ cells in EM were non-replicative and we estimate a proliferative fraction of 3-6%. In both EM and IM, ~25% of Cyclin $D1^+$ cells expressed the cyclin-dependent kinase inhibitors p21 or p27, but this was not sufficient to explain the difference between EM and IM with respect to proliferation. However, we found that the majority of non-proliferating Cyclin $D1^+$ cells in EM had elongated nuclei and were found in clusters surrounding small $CD31^+$ vascular structures (CD31 labels vascular endothelium). Thus cell cycle progression has non-canonical aspects in EM.

Single-cell analysis of invasive tumor reveals large scale gradients in lineage, immune, and proliferation markers

To study tumor programs at single-cell resolution, CyCIF data on ~5 x 10^5 malignant single cells in MEL1-1 were analyzed using PCA and unsupervised clustering (**Figure 3A**). PC1 and PC2 explained

40% of variance and Score Plots showed that the top loadings were the proliferation marker KI67, the S100A and S100B proteins, and the MITF transcription factor (**Figure S3A**). MITF is a master regulator of melanocyte differentiation (Levy et al., 2006) widely studied as a melanoma oncogene (Garraway et al., 2005) and a determinant of drug resistance (Bai et al., 2019a). An $MITF^{low}$ state has been associated with de-differentiation and resistance to RAF/MEK therapy (Konieczkowski et al., 2014). NGFR (CD271) and the AXL receptor tyrosine kinase are two other proteins widely studied for their roles in melanoma state switching and drug resistance (Shaffer et al., 2017) but we detected only sporadic NGFR expression in MEL1 tumor cells by either mrSEQ or imaging. AXL was detected only on the plasma membranes of keratinocytes and immune cells, not tumor cells (Bauer et al., 2012). Unsupervised clustering (with k=5; see STAR methods) yielded two $MITF^{low}$ clusters (T1 and T2; comprising 59% of tumor cells) and three $MITF^{high}$ clusters (T3 to T5; 41% of tumor cells in total) (**Figures 3A** and **3B**). Spatial proximity analysis (see STAR methods) showed that tumor cells in clusters T1 to T4 are not within 20 µm of immune cells, consistent with a lack of immune infiltration. In contrast, cells in T5, which made up 7% of tumor cells exhibited significant co-occurrence with multiple immune cell types ($P < 0.05$; **Figure 3C**). Thus, differences in cell states T1 to T4 are likely to be dominated by cell-type intrinsic programs whereas local tumor-immune interactions are also possible for T5 cells.

T1 cells expressed high levels of S100A and S100B and T2 cells expressed low levels of both proteins. T1 cells were widely distributed in EM and IM (**Figure 3D**). Across the whole tumor, S100A, S100B, and MITF exhibited a striking gradient in the expression on both longer and shorter length scales, with the highest levels at the invasive margin where T1 cells were found, and lowest in the middle of the EM (**Figures 3E, 3F** and **S3B**). Thus, whereas clustering of single-cell CyCIF or scRNA-Seq data (Tirosh et al., 2016) emphasizes the presence of dichotomous MITF or S100 high and low states, direct inspection of marker expression levels in images reveals continuous changes in protein levels. Spatial gradients involving morphogens have been widely studied in tissue development (Rogers and Schier, 2011) but infrequently in cancer (Oudin and Weaver, 2016).

Across all tumor cells, KI67 and PCNA levels were positively correlated with MITF expression (PCNA: r=0.63, KI67: r=0.46; p-value=0), consistent with a role for MITF in promoting tumor cell proliferation (the opposite of its function in normal melanocytes) (Goding and Arnheiter, 2019). $MITF^{high}$ T3 cells were broadly distributed whereas T4 cells were primarily found in the IM (with an additional focus on the left EM margin; **Figure 3D**). T5 cells were divisible into a $CCND1^{high}$, $MHC\text{-}II^{low}$ subcluster (T5a; 4%) and a $CCND1^{low}$ $MHC\text{-}II^{high}$ subcluster (T5b; 3%), each with distinctive

localization patterns. At low magnification, patches of CCND1^{high} T5a cells were broadly distributed across the invasive tumor (**Figure 3D**) but at higher magnification, they colocalized with the margins of perivascular spaces that also contained several types of myeloid cells, T cells, and other as-yet-unidentified cells (**Figure S3C**). The spatial distribution of MHC-II (HLA-DPB1) expressing T5b cells was restricted to a tumor margin, with the great majority found at the invasive boundary, where they formed a band of cells roughly twice as wide as the IRF1 band (i.e., ~ 100 µm or 4 cell diameters; **Figure 3G** and **S3D**). MHC-II is primarily expressed on antigen-presenting immune cells but MHC-II is also expressed in a subset of melanomas, where it can interact with Tregs, promoting their activation (Paluskievicz et al., 2019). MHC-II can also bind LAG3-expressing T cells, promoting melanoma persistence by upregulating MAPK/ PI3K signaling and facilitating immune escape by suppressing FAS-mediated apoptosis (Hemon et al., 2011).

Expression of MHC-II in melanoma cell lines is induced by the inflammatory cytokine IFN□ (Propper et al., 2003). In the IB region, GSEA of mrSEQ data revealed significant and localized upregulation of IFN□ (**Figure 2F**), JAK-STAT signaling (**Figures S3E** and **S3F**), and *CXCL10* and *CXCL11* expression (**Figure 3H**). These chemokines (along with CXCL9 and the CXCR3 receptor) have diverse roles in regulating immune cell migration, differentiation, and activation, and may play a role in response to immune checkpoint inhibitor therapy (House et al., 2020). The metabolic enzyme IDO1 was also enriched at the invasive boundary (**Figure 3H**) (Metzemaekers et al., 2017) and has previously been reported to inhibit CTL activation (Brody et al., 2009; Zhai et al., 2020) and promote recruitment of regulatory T cells and myeloid-derived suppressor cells (MDSCs) (Holmgaard et al., 2015). Thus, a unique microenvironment exists at the IB involving IFN□ expression and induction of the JAK-STAT-IDO1 pathway (Mojic et al., 2017) leading to hallmarks of immune recruitment and activation but also suppression. Expression of the interferon-stimulated genes (ISGs) MX1 and IFI16 was also detected by mrSEQ in mROIs near the IM core, with MX1 mRNA expression higher in EM than in IM (**Figure S3G**); this difference was confirmed by CyCIF (**Figure S3H**). The reasons for differential ISG expression are unknown, but the biological effects of IFN□ in the TME are concentration-dependent (Jorgovanovic et al., 2020). We speculate that IFN□ produced by CTLs and other immune cells found near the IB diffuses into the tumor, inducing MHC-II and IDO1 at the boundary and other ISGs elsewhere in the tumor.

A reciprocal mechanism was detected involving the macrophage migration inhibitory factor (MIF). MIF is an inflammatory cytokine overexpressed by a variety of cancers (Balogh et al., 2018) and was more abundant in tumors (MIS, IM, EM) than in immune-rich regions (bTIL, IR; DE with $p < 0.05$)

(**Figure 3H).** The MIF receptor CD74 was also most abundant in immune-rich (bTIL) regions but detectable in IM and EM, consistent with IFN□-mediated induction of CD74 (Tanese et al., 2015)(**Figure 3H)**. The binding of MIF to CD74 in melanoma cells promotes PI3K/AKT activation and cell survival. We detected elevated expression of a second MIF receptor, CXCR4, and of another cognate ligand, CXCL12, in the bTIL region; CXCR4 activation leads to expansion of immunosuppressive Tregs (Noe and Mitchell, 2020). CXCR4 is the chemokine receptor most commonly found on cancer cells, and binding to CXLC12 is thought to promote invasive and migratory phenotypes leading to metastasis (Sun et al., 2010). However, mrSEQ showed that CXCR4 levels were low in IM and EM. (**Figure 3I**). Thus, mrSEQ data are most consistent with autocrine stimulation of tumor cells by MIF, suppression of immune cells by MIF acting in a paracrine manner, and overlapping regulation by CXCL12 in the stromal but not the tumor compartment.

Spatial organization of cells in tumor domains

To identify subtle but recurrent spatial patterns within tumor domains, we computed spatial lag using CyCIF data. Spatial lag is a common spatial statistic used in geography and ecology (Rey, 2001) that we used to identify sets of contiguous cells (communities) having similar protein expression levels when expression varies continuously through space. When spatial lag vectors were clustered, 10 distinct tumor cell communities (TCC) were identified (see STAR methods; **Figures S4A** and **S4B)**. As expected, some communities corresponded to cell types identified above by conventional (non-spatial) clustering; for example, TCC1 corresponded to the S100A^{high} MITF^{low} pattern in T1 in and TCC4 corresponded to MHC-II^{high} in T5b. At the invasive boundary, seven tumor communities were identified in ~3,800 tumor cells, with each community forming a narrow layer of cells separated from the central core. For example, TCC8 was found internal to TCC3, which constituted the invasive front, and TCC1 and TCC2 were primarily found at the trailing edge. In general, TCCs differed in hyperdimensional features but in some cases, their single markers dominated: MHC-II positivity for TCC3 and a MITF^{high} KI67^{low} state for TCC8 (**Figures 4A**, **4B** and **4C**). To our knowledge, melanoma has not previously been reported to involve such a layered arrangement of tumor cells.

Invasiveness by melanoma cells is commonly described as involving a MITF^{low} slowly-cycling state (Bai et al., 2019a) but across all tumor cells in the IM, 85% were MITF^{high} and 15% were MITF^{low} with KI67^{low} and KI67^{high} states intermixed spatially (**Figures 4D** and **4E**), as expected for a proliferation marker. The MHC-II^{+} TCC2 community found at the invasive front was comprised of 70 to 85% MITF^{high} KI67^{high} cells and a subset of which stained positive for cyclin A2, cyclin B1 and pHH3

in the expected proportions based on data in **Figure S2G,** confirming a high proliferation index. The invasive state is reported to involve upregulation of EMT and anti-apoptotic programs (Bai et al., 2019b) and we observed both in IM (**Figure 2M** and **S2D**). Thus, the cells at the IB in MEL1 have molecular properties associated with invasion but are neither $MITF^{low}$ nor slowly proliferating (relative to the rest of the tumor). Analysis of additional tumors will be required to more fully understand the relationship between MITF levels, cell cycle progression, markers of EMT and invasion, and depth of invasion.

Recurrent cellular neighborhoods associated with melanoma progression

Experience with scRNA-Seq has shown that subtle intra-tumor differences among single cells are difficult to generalize across tumors using a single unified computational model (Fan et al., 2020). In contrast, models based on discrete differences among cells of different types are more robust. We, therefore, used Latent Dirichlet Allocation (LDA) (Blei et al., 2003) to identify recurrent features of the TME across patients and histologies (**Figure S5A**). LDA is a probabilistic modeling method that reduces complex assemblies of intermixed entities into distinct component communities and is used in biodiversity studies because it can detect both gradual and abrupt changes in the composition and arrangements of natural elements (cells in a tissue or trees in a forest) while effectively accounting for uncertainty and missing data (Jackson et al., 2020; Valle et al., 2014). To identify recurrent cellular neighborhoods (RCNs), cell types were first assigned to one of 12 basic classes based on patterns of expression of cell type and state markers (e.g., proliferating, regulatory, exhausted) using 22-plex CyCIF data from 1.7×10^6 single cells in MEL1-MEL13 (**Figures 5A** and **S5B**). These data derived from all patients and histologies and exhibited good signal to noise across multiple markers (**Figure 5B**). Moreover, when we quantified progression markers, we observed the expected increase in positivity from adjacent normal skin, to fields annotated across all specimens as melanoma precursors, MIS, and invasive melanoma; this provides molecular confirmation of the histological assignment (**Figure 5C**) (Xiong et al., 2019). We trained a spatial-LDA model using a 20 μm proximity radius so that RCNs would be enriched for cells in physical contact and latent weights then grouped using k-means clustering (k=30) into ten informative meta-clusters (see methods**)**. The RCNs corresponding to meta-clusters were annotated based on cellular composition, frequency of occurrence in 71 ROIs annotated for disease-relevant histology, and mapped to physical positions in the original specimens (**Figure 5D**).

RCNs could be grouped into five major classes (epidermis, myeloid, T, melanocytic, and immune-suppressed) based on cellular composition (**Figures 5E**). RCN1 was rich in Langerhans cells and keratinocytes (70% of cells in the RCN1) and co-extensive with the epidermis (**Figure S5C**).

RNC10 contained the largest number of cells (38% of all cells quantified in MEL1-MEL13), 90% of which were SOX10$^+$ and found in regions of vertical growth phase melanoma (EM and IM) (**Figure 5D**); in these regions, tumor cells were densely packed together with few infiltrating cells (**Figures 6A** and **6B)**. In contrast, RCN9 (comprising ~6.4% of all cells) contained equal numbers of SOX10$^+$ and immune cells (36% and 34%, respectively) and corresponded to the interface between solid tumor and the dermis (red; **Figure 5D, 6A-B**). 80% of the immune cells in RCN9 were CD11C$^+$ macrophages and dendritic cells (some examples of RCN9 and RCN10 were also found in adjacent normal skin and regions of melanocytic atypia where SOX10$^+$ cells were close to each other; **(Figure 6C, S6A**)). The frequency of RCN9 communities increased significantly from precursor to MIS to invasive tumor, highlighting the formation of a myeloid enriched tumor boundary, with RCN10 becoming predominant in EM (**Figures 6D**, **S6A,** and **S6B**). As a confirmation of the LDA approach, we independently quantified the proximity of tumor and CD11C$^+$ myeloid cells (the constituents of RCN9) using a 10 µm cutoff and found that the volume scores increased from precursor to MIS to IM stages, mirroring the progressive increase in RCN9 frequency (**Figure S6B** and **S6C**).

Seven RCNs were highly enriched in immune cells and these fell into three classes: enriched for myeloid cells (RCN2-4), enriched for T cells (RCN6-7), and immune-suppressed (RCN5, 8). RCN2-4 contained overlapping sets of cells, with tissue-resident macrophages predominating in RCN2, and CD11C$^+$ cells in RCN3 and 4 (unlike RCN9, RCN2-4 did not contain tumor cells) (**Figure 5D**). RCN2 was found throughout the dermis with a distribution similar to that of tissue-resident macrophages while RCN3 and 4 were found close to the invasive tumor (**Figure S6D**). RCN6 was rich in CD4$^+$ T helper and regulatory T cells (Treg) and RCN7 was enriched for CTLs. RCN5 and 8 had high proportions of activated PD1$^+$ CTLs as well as Tregs and PDL1$^+$ myeloid cells, which are immunosuppressive (Peng et al., 2020). Five of the seven immune enriched niches (RCN3-7) significantly ($P < 0.05$) increased in frequency between precursor and MIS, while only one (RCN4) significantly increased between normal and precursor fields, reflecting recruitment of myeloid cells. Two significant changes were observed between MIS and IM and this involved RCN9, which increases in abundance due to the formation of the PDL1$^+$ sheath at the IB, and RCN1, which falls in abundance due to a lack of keratinocytes in IM (**Figure S6E**). Thus, the most dramatic differences in cellular communities occur between precursor and MIS stages, as opposed to MIS and invasive tumors.

When we quantified the proximity of immune rich RCNs (RCN2-8) to SOX10$^+$ cells in RCN10 (i.e., melanocytes or tumor cells) we found that myeloid-enriched (RCN2, 4) and PDL1-enriched (RCN5) communities were significantly closer to RCN10 in precursor ROIs than adjacent normal skin

or later disease stages. In contrast, a cytotoxic community (RCN7) was closer to RCN10 in precursor samples than in MIS or IM (**Figure 6E**). To confirm this finding, we measured the distance between melanocytic cells and the nearest PDL1$^+$ myeloid cell or CTLs. We observed a significant decrease in distances for both cell types between normal and precursor stages. Tregs also showed a significant decrease in proximity to melanocytic cells in precursor fields **(Figure 6F**). Thus, at the precursor stage, recruitment of cytotoxic T cells was accompanied not only by immune resolution but also the first signs of immunosuppression by myeloid cells.

When RCNs were mapped back to the highly characterized landscape of MEL1-1, we found that the community of tumor cells near CD11C$^+$ myeloid cells (RCN9) was sporadically present in association with MIS but well established as a nearly continuous sheath at the invasive boundary of IM (**Figures 6A-6C**). Immediately adjacent to this we observed RCN3 and 4 myeloid niches in a mosaic pattern with RCN6 (T helper and Treg) and RCN5 (PDL1$^+$ immune-suppressive) neighborhoods. The density of immunosuppressive niches was also highly variable even between nearby locations **(Figure 6A, B**). RCNs containing cytotoxic T cells (RCN7) and PD1$^+$ CTLs (RCN8) were also intermingled, consistent with local activation of T-cells. Moreover, whereas intermixing of tumor cells (RCN10) and multiple immune-rich RCNs was evident in MIS, in EM and IM myeloid and immunosuppressive RCNs were largely confined to the area immediately surrounding the CD31$^+$ vasculature described above. These patterns were repeated across patients, with increasingly complex immune environments with lesion evolution.

PDL1 mediated immune suppression

The importance of PD1-PDL1 interaction in melanoma is demonstrated by the success of anti-PD1 therapy. Across all 13 specimens, ~70% of CTLs expressed the activation marker PD1 but we detected very few tumor cells expressing significant levels of PDL1, even in regions of the tumor where IFN was expressed (IFN is a known inducer of PDL1). 3D deconvolution imaging proved to be more sensitive than conventional CyCIF in detecting PDL1, but even in MIS, in which immune and tumor cells were intermixed, only 5 of 106 tumor cells imaged across 12 high-resolution FOVs were judged to be PDL1 positive. In these cases, imaging showed that PDL1 ligand on tumor cells and PD1 receptor on CTLs were co-localized, consistent with ligand-receptor binding (**Figures 7A** and **S7A**). In contrast to the paucity of PDL1$^+$ tumor cells across all patients, a significant co-occurrence ($P < 0.05$) was observed between PD1$^+$ CTLs and PDL1$^+$ macrophages and dendritic cells in 44 of 70 annotated histological domains; the frequency of this co-occurrence also increased with disease stage (**Figure 7B**).

To confirm functional interaction, we performed high-resolution 3D imaging of FOVs spanning the invasive melanoma front in patient MEL1-1 and observed frequent contact between $PD1^+$ CTLs and either $PDL1^+$ macrophages or dendritic cells with a concentration of PD1 and PDL1 at the site of cell-to-cell interaction (**Figures S7B** and **S7C**). In some cases, macrophages formed presumed inhibitory synapses with CTLs via cellular processes that extended at least one cell diameter (10 μm) from the macrophage (**Figure 7C, Supplementary Video**). A substantial subset of $PDL1^+$ myeloid cells expressed TIM3, which is also associated with immune suppression (**Figure 7D** and **7E**).

We conclude that the repressive cells most frequently in contact with $PD1^+$ CTLs are $PDL1^+$ dendritic cells and/or macrophages. Recent data from the MC38 murine syngeneic model of colorectal cancer suggests that dendritic cells, not macrophages, are the relevant myeloid cell type for PDL1-mediated immunosuppression of activated CTLs (Oh et al., 2020). Whereas these investigators reported that $PDL1^+$ macrophages greatly outnumber $PDL1^+$ dendritic cells in human and mouse cancers, we find that these two types of myeloid cells were similar in abundance in primary melanoma (1.2 to 1.4% of all cells). By high-resolution imaging of the invasive front, we also found multiple fields in which tumor cells, CTLs, dendritic cells, and other immune cell types, a subset of which expressed PD1 or PDL1, were all in direct contact with each other as part of extended networks (**Figure 7E**). Sorting out the significance of these multi-dentate interactions will require imaging additional regulatory molecules in the B7-CD28 superfamily.

Co-existence of activated and suppressed T cell microenvironments within the TME

Successful immune editing and clearance of $SOX10^+$ tumor cells at regions of inflammatory and terminal regression in MEL1 were observed adjacent to MIS. In these regions, we found dense infiltrates of CTLs, the majority of which were $PD1^+$ and thus activated, as well as Tregs. The greatest concentration of $PD1^-$ CTLs in MEL1 was also found in the IR (**Figure 7F** and **S7D)** and $MHC\text{-}II^+$ APCs were abundant, consistent with ongoing Treg activation (**Figure 7G** and **S7D)**. Imaging showed that a significant fraction of the $PD1^+$ CTLs expressed LAG3 and/or TIM3, suggesting that they were terminally exhausted. mrSEQ confirmed expression of PDL1, LAG3, TIGIT, and CTLA4 in regions of inflammatory regression at levels similar to those observed at the immunosuppressed bTIL region in front of IM (**Figure 7H)**. We speculate that in regions of regression, antigens are cross-presented by APCs to CTLs which become activated ($PD1^+$), engage tumor cells, and subsequently become exhausted ($TIM3^+$ and/or $LAG3^+$ expressing) as part of a normal anti-tumor immune response. In contrast, in the bTIL region apposed to the vertical growth phase tumor, an abundance of $PDL1^+$ macrophages and

dendritic cells leads to a higher level of exhaustion in the absence of tumor cell killing. Thus, a concentration of terminally exhausted T cells near tumor cells is not *prima facie* evidence of an absence of active cell killing.

DISCUSSION

In this paper, histological features routinely used to stage primary cutaneous melanoma were used as a framework for placing multiplexed imaging and mrSEQ data along an axis of tumor progression from precursor fields to melanoma *in situ*, to invasive melanoma. We also examined immune-rich regions near the dermal-epidermal junction in which immunoediting was ongoing or had reached a resolution with no tumor cells present. Molecular evidence of progression was obtained using protein markers (by CyCIF) and oncogenic programs (by mRNA expression) both within specimens comprising several distinct histologies, and also across the patient cohort. Conventional CyCIF yielded data on morphological features ranging in length scale from 0.5 µm (organelles) to 20 mm (invasive fronts) and high-resolution 3D imaging revealed immune synapses and PD1-PDL1 co-localization on the plasma membranes of neighboring cells; we interpret these as evidence of functional cell-to-cell interaction. We found that imaging the entirety of specimens up to ~1 cm in length – not a TMA or a small region of interest – was essential for retaining information on tissue context and for the success of our approach.

The use of Latent Dirichlet Allocation (LDA) made it possible to identify recurrent combinations and arrangements of cell types across 13 specimens. The frequency of these recurrent cellular neighborhoods (RCNs), and their proximity to each other, changed with disease progression (**Figure 7I**). Relative to adjacent normal skin, significant changes in the immune environment were already detectable in fields of melanocytic atypia (precursor fields) but the largest overall difference along the progression axis was observed between precursor fields and MIS and involved recruitment of CTLs, many of which were $PD1^{+}$, and thus activated, as well as suppressive Tregs and PDL1-expressing myeloid cells. The immunosuppressive environment became more consolidated between the MIS and invasive stages. For example, in MEL1, a community of cells involving tumor and $PDL1^{+}$ myeloid cells (macrophages and dendritic cells in roughly equal proportion) formed a thin and continuous sheath along the invasive front. TILs were largely excluded from the tumor at this stage, except in the immediate proximity of small vascular structures that were found throughout the EM.

Whereas LDA was effective at identifying neighborhoods involving different types of cells, spatial lag modeling on CyCIF data identified recurrent patterns involving continuous differences in

protein levels, most on a scale of 10 to 100 cell diameters. Spatial gradients on similar scales were also observed for several marker proteins – MITF or S100B for example. Thus, whereas LDA and clustering of transcriptional data highlight discrete differences in cell states, imaging demonstrates the presence of gradients reminiscent of those in developing tissues (Oudin and Weaver, 2016; Rogers and Schier, 2011). In general, significant differences among cancer cell communities involved hyperdimensional features (combinations of markers instead of single proteins) consistent with the current understanding of the molecular determinants of cellular morphology (Bray et al., 2016). Thus, gradients in MITF or S100B are likely to be illustrative of large-scale tumor organization, not underlying causes. One unexpected finding involved the "invasive" state of melanoma cells, which is often described as being $MITF^{low}$ with slow proliferation. Spatial lag modeling showed that $MITF^{high}$ $KI67^{high}$ cells were common in MEL1 in the immediate proximity of the invasive front and mrSEQ showed that these cells were significantly enriched in EMT programs, which are common along invasive tumor boundaries. Future studies on paired primary and metastatic tumors will be required understand how these data related to previous analysis of MITF high and low states, which has largely been performed in cell lines.

CyCIF and mrSEQ revealed a pattern of cytokine production and receptor expression at the invasive boundary of MEL1 consistent with paracrine regulation of both tumor and immune cells (**Figure 7J**). The dermis in this region was rich in TILs (corresponding to a brisk TIL response in the Clark grading system) and was the site of highest IFN□ production. A band of cells ~2 cell diameters wide in the adjacent invasive melanoma stained positive for nuclear-localized IRF1, the master regulator of interferon response (orange cells in **Figure 7I**); mrSEQ showed that JAK-STAT signaling was active in this region and IDO1 differentially expressed. IDO1 converts tryptophan into kynurenine, which activates Tregs and MDSCs, and is known to be immunosuppressive in melanoma (Spranger et al., 2013). MHC-II was also expressed in both immune and tumor cells at the invasive boundary, in a band roughly twice as wide as IRF1, and can function in this context by binding to LAG3 on TILs, leading to inhibition of TCR signaling and T cell activation (Hannier et al., 1998; Huard et al., 1997). MIF1 was another inflammatory cytokine found at the invasive front and was expressed primarily in invasive tumors; responsive CXCR4-expressing immune cells were found in the stroma. MIF1 may also have an autocrine activity since expression of the MIF1 receptor CD74 was detected in the tumor itself. CXCR4-expressing immune cells are also responsive to CXCL12, which was expressed in the TIL-rich stroma. CXCR4 is the cytokine receptor most commonly found on melanoma and other types of cancer cells, and CXCR4-CXCL12 signaling is thought to promote metastasis (Sun et al., 2010), but we did not observe CXCR4 expression in MEL1 by mrSEQ. We conclude that the immunosuppressive activity of

IFN manifests itself in MEL1 in a spatially restricted manner involving a sheath of tumor and myeloid cells surrounding the invasive tumor and is one aspect of reciprocal cytokine signaling between tumor and immune cells.

Performing spatial proximity analysis on imaging data (with a 10-20 µm cutoff) makes it possible to identify cells that are sufficiently close to each other that physical contact is probable. We were able to visualize these contacts and infer function using high-resolution 3D imaging of ~5 $x10^3$ cells. The most informative images were those involving cytotoxic T and melanoma cells that resulted in the polarization of CD8 (a co-receptor for the T-cell receptor) at the point of contact, consistent with the formation of a functional synapse. $PD1^+$ CTLs cells were also observed in contact with PDL1-expressing macrophages and dendritic cells resulting in receptor-ligand co-localization. In some cases, these contacts involved surprisingly extended processes (>10 µm) in which macrophages appeared to stretch towards T cells. In other cases, multiple CTLs, T helper, and myeloid cells were found to be in physical contact with each other and with tumor cells with evidence of receptor or ligand polarization. The functional significance of these clusters awaits further analysis using a greater diversity of immune markers but they are presumably a physical manifestation of the competing activating and inhibitory effects of other immune cells on CTLs.

Overall, we found evidence of at least six immunosuppressive mechanisms operating near the invasive front. Particularly striking was the overlap in the binding of $PD1^+$CTLs to $PDL1^+$ macrophages and dendritic cells and tumor cell-intrinsic phenotypes such as MHC-II and IDO1 expression. Unexpectedly we did not detect high expression of PDL1 on tumor cells by either whole-slide imaging or high-resolution microscopy (even when IFN expression was detected). We, therefore, conclude that myeloid cells are likely to be the predominant source of PDL1 in the tumors in our cohort. The results obtained by Oh et al (Oh et al., 2020) also indicate that the functionally significant cell type is likely to be $PDL1^+$ dendritic cells.

CTLs were found to actively engage tumor cells in a region of inflammatory regression adjacent to MIS in MEL1. The additional presence of an adjacent region of complete regression, which was rich in immune cells but free of tumor cells, suggests that immune editing was successful. However, these regions also had a preponderance of terminally exhausted CTLs, showing that the characteristics of a successful and self-limiting anti-tumor immune response superficially resemble those of immunosuppression in invasive melanoma. The primary difference we observed between regions of regression and invasion with immunosuppression was a substantially lower level of $PDL1^+$ myeloid cells, but further research will be required to determine if this is generally true.

Limitations of this study

One challenge encountered in molecular analysis of primary melanoma is that, as a diagnostic necessity, specimens are available only in FFPE form, complicating single-cell mRNA sequencing for research purposes. A second challenge is that meaningful outcome analysis requires long follow-up: all patients whose tumors were analyzed in this study were diagnosed between 2017 and 2019 and were alive at the time of the last follow-up; ~75% were disease-free. We, therefore, used histologic progression not outcomes to organize the data in a biologically meaningful fashion. Despite the scope of the current data collection effort, we were unable to fully characterize the spatial diversity of the 13 specimens in our data set, in part because the friability of precursor fields and adjacent normal skin made very highly multiplexed imaging challenging; we expect that this problem can be overcome in future studies. Thirteen specimens are also too few to be representative of the diversity of cutaneous melanoma. We estimate that data collection will need to be scaled up 5 to 10-fold to determine whether many of the features observed in MEL1 are significantly associated with progression in other specimens. Spatially resolved mRNA expression and high-plex imaging data support each other in many cases, but this was not always true. This is not unexpected because mRNA and protein expression are known to be uncorrelated in many cases (Maier et al., 2009) and cell morphology represents a hyper-dimensional feature in gene expression space (Bray et al., 2016). 3D image data has provided valuable insight into cell-to-cell interactions, but automated segmentation of these data remains difficult and most conclusions were derived from a human inspection of images. More generally, the greatest limitation in the current work is related to the underdevelopment of software tools for characterizing large high-plex tissue images. Much therefore remains to be discovered from the images we have collected. Full resolution Level 3 images and associated single-cell data are therefore being released in their entirely, without restriction, for follow-on analysis.

ACKNOWLEDGEMENTS

We thank David Liu, Genevieve Boland, Jeremy Muhlich, David Weinstock, Robert Krueger, Jared Jessup, and Simon Warchol for their help in multiple stages of this project. This work was supported by NIH grants U2C-CA233262 (PKS, SS), K99-CA256497 (AJN), the Ludwig Center at Harvard (PKS, SS), R50-CA252138 (ZM), and by grants from the Finnish Medical Foundation and the Relander Foundation (TV). Access to the GeoMX mrSEQ platform was kindly provided by NanoString Inc. as part of their Technology Access Program. (TAP). All HTAN consortium members are named at

(humantumoratlas.org). We thank Dana-Farber/Harvard Cancer Center for the use of the Specialized Histopathology Core, which provided histopathology services supported by P30-CA06516. Imaging at the HMS Neurobiology Imaging Facility (of H&E specimens) was supported by NINDS Core Center Grant P30-NS072030.

AUTHOR CONTRIBUTIONS

AJN, ZM, TV, BQ, CGL, GFM, SS, and PKS developed the concept for the study. CAJ, AJN, RJP, CP, YC, TV, CY and ZM collected and processed data and performed computational analysis. CAJ, CY, YC, and TV developed MINERVA stories and other visualizations; AAC and RAC processed and annotated clinical data. All authors wrote and edited the manuscript. CGL, GFM, SS, and PKS provided supervision and funding.

DECLARATION OF INTERESTS

PKS is a member of the SAB or BOD member of Applied Biomath, RareCyte Inc., and Glencoe Software, which distributes a commercial version of the OMERO database; PKS is also a member of the NanoString SAB. In the last five years, the Sorger lab has received research funding from Novartis and Merck. Sorger declares that none of these relationships have influenced the content of this manuscript. SS is a consultant for RareCyte Inc. ZM is a consultant for Verseau Therapeutics Inc.

FIGURE LEGENDS

Figure-1: Multimodal profiling of cutaneous melanoma

(A) Conceptual framework of sample processing for cyclic immunofluorescence (CyCIF), high-resolution CyCIF, and micro-region transcriptomics: GeoMx and PickSeq (mrSEQ). Abbreviations for annotated histologies are shown below with color-coding used in subsequent figure panels.

(B) A 30-plex CyCIF image of a section of specimen MEL1-1 showing selected markers for epidermis (PanCK: cyan) and tumor cells (SOX10: red), highlighting annotated histologies and microregions (mROIs) that were subjected to mrSEQ (white +s). This specimen was likely torn during slide processing and thus, spatial arrangements in the region marked with a blue dashed boundary are not considered reliable. Other mrSEQ sites are shown in Supplementary Figure 2A.

(C) CyCIF image of MEL1-1 corresponding to the MIS and adjacent regions of inflammatory and terminal regression (IR and TR, respectively; outlined by dashed white lines). Rectangles depict the

positions of 110 x 110 µm regions of interest (ROIs) in which high-resolution 3D deconvolution microscopy was performed. The region highlighted with orange is magnified in panel G.

(D) Uniform manifold approximation and projection (UMAP) of single-cell data derived from CyCIF of patient MEL1 labeled by cell type (upper panel) and the signal intensities of individual markers (lower panels). Markers used for cell-type calls are shown in Supplemental Figure 1C. The UMAP plot was built using 50,000 single-cells that were randomly sampled from the full data set ($n = 1.1 \times 10^6$).

(E) Cell type assignments (with data points representing the centroids of cells) mapped to their physical locations in a portion of the bTIL region lying just beyond the IM in MEL1-1

(F) H&E image of the same region as in Panel E. Regions of tumor and stroma are `separated by dashed black lines.

(G) A 21-plex high-resolution CyCIF image of a MEL1-1 MIS region (orange square in panel C) with selected markers shown as a maximum intensity projection staining for DNA (blue), tumor (SOX10: white), and T cells (CD4: green, CD8: red). The dermal-epidermal junction is denoted with a white dashed line and all $FOXP3^+$ cells (as determined from other image channels; see Supplemental Figure 1F) are denoted with an asterisk. Scale bar, 25 µm. Note that all images in panels G to J derive from a single multiplex CyCIF 3D image stack.

(H) Magnified regions from panel G (outlined with a yellow box) showing staining of DNA (blue) and CD4 (green), CD8 (red), and TIM3 (white). Four cell types are labeled including a regulatory T cell (Treg, green box – shown in panel 1J) and two $CD8^+$ CTLs interacting with a tumor cell (shown in the panel I). The dashed line follows the axis of immune synapse polarization and gives rise to the intensity plot in the panel I. The orange box depicts the locations of representative images in panel I. Scale bar, 10 µm.

(I) Single optical section images of the immune synapse in panel H showing staining of tumor (SOX10: white), DNA (blue), and cell membrane (HLA-A: magenta) along with a series of single-channel images of functional T cell markers. The right panel shows the quantified spatial distribution of CD8 and CD3 along the dashed line in panel H.

(J) Inset from panel H (outlined with a green square). Single optical section images of a tumor cell interacting with a Treg. Upper panels: staining for tumor (SOX10: white), cell membrane (HLA-A: magenta), and DNA (blue); lower panels: staining for Treg (ICOS: cyan). The two z-sections shown are spaced 2.2 µm apart.

Figure-S1 (Related to Figure 1):

(A) Representative examples of the histopathological features annotated in samples MEL1-MEL13. H&E-stained section of MEL1-1 with three major histologic regions indicated: melanoma in situ (MIS), invasive melanoma (IM), and exophytic melanoma (EM). H&E and the corresponding CyCIF staining of normal, precursor, MIS, IM, and EM regions.

(B) CyCIF images of MIS, IM, and EM regions (from top to bottom row) of MEL1-1 stained in a composite image (left column) for DNA (blue), the epidermis (PanCK: cyan), and tumor (SOX10: red, MART1: green). Individual grayscale images for staining with S100A, NGFR, and MITF are shown in the right panel. The tumor boundary of EM is indicated by a dotted line. Scale bar, 50 µm.

(C) Flowchart used in CyCIF experiment 1 indicating strategy used for cell type calling.

(D) CyCIF of MEL1-1 stained for tumor (SOX10: blue), T-cells (CD3D: purple) and macrophage (CD163: green) markers and epidermis (panCK: white). High-resolution 3D deconvolution microscopy images were obtained from MIS and IM regions. Imaging regions for MIS are presented in panel 1C. Regions within IM1 (green box) and IM2 (red box) are indicated with squares (bottom panel). The invasive front is indicated by a dashed white line.

(E) CyCIF image of MEL1-1 (same region shown in panel 1G) stained for melanocytes (MITF: white), T cells (CD3: yellow), macrophages (CD163: red), myeloid cells (CD11C: magenta), and keratinocytes (PanCK: cyan). Epidermis, dermis, and dermal-epidermal junction (dashed line) and region of panel 1I (white box) are marked. Scale bar, 50 µm.

(F) CyCIF of the region shown in panels E and 1G stained for DNA (white) and T-regs (FOXP3: blue, marked with asterisks). Scale bar, 50 µm.

(G) Composite high-resolution CyCIF inset from panel 1H stained for DNA (blue), SOX10 (white), LAG3 (green) and TIM3 (red). Scale bar, 10 µm.

(H) Single optical section CyCIF images depicting the interaction between a Treg (CD4: red and ICOS: cyan), a melanocyte (SOX10: white), and a CTL (CD8: magenta and CD3: green). z=0 µm (left panel; also shown in panel 1I) and z = -2.0 or +2.4 µm (second to left panel; shown also in panel 1J). Magnified regions (green boxes) show co-staining for CD3 (green) or CD4 (red) in each optical section (right panel). Scale bar, 10 µm (left panel) or 5 µm (right panel).

(I) Quantified spatial distribution of CD8 (red) relative to HLA-A (black) and functional T cell markers ICOS (green), LAG3 (blue), PD1 (magenta), and TIM3 (gold) based on images in panel 1I.

Figure-2: Micro-regional transcript profiling

(A) Principal component analysis (PCA) plot of melanoma mrSEQ transcriptomes (GeoMX). Colors indicate regional histopathology: brisk TIL (bTIL: pink), inflammatory regression (IR: brown), MIS (green), invasive front (IB: light green), exophytic melanoma (EM: grey), and center of invasive melanoma tumor (IM: yellow). EM and IM are enriched for tumor cells in this analysis and IB contain mostly tumor cells with marginal immune infiltration.

(B) Expression of selected melanoma-related marker genes in mrSEQ data (PickSeq) split into three broad groups based on the PCA of GeoMx data (panel A). Data is mean ± SEM. ***P<0.001; ns = not significant.

(C) Single-sample gene set enrichment analysis (ssGSEA) on mrSEQ data (PickSeq). ssGSEA scores highlight enrichment of melanoma-related gene signatures in tumor mROIs (primarily IB, IM, and EM) and immune-related signatures in the immune-rich mROIs (IR, bTIL).

(D) CyCIF of specimen MEL1-1; (top) zoomed out view of invasive front stained for melanocytes (SOX10: blue), myeloid cells (CD11C: red), and interferon signaling (IRF1: green); (bottom left) zoomed-in view of invasive front apex stained for melanocytes (SOX10: blue), myeloid cells (CD11C: red) and interferon signaling (IRF5: yellow); (bottom right) zoomed-in view of invasive front apex stained for melanocytes (MART1: green), myeloid cells (CD11C: blue) and interferon signaling (IRF1: red). Scale bar, 50 μm.

(E) Line plot showing scaled fluorescence intensity of SOX10 (blue) and IRF1 (pink) within (tumor; left of the dashed blue line) and outside (stroma; right of the dashed blue line) the invasive tumor front seen in panel D.

(F) Expression of IFNG in mrSEQ data (GeoMX). Data is mean ± SEM; **P<0.01.

(G) CyCIF image showing a field of view in MIS (top panel) and EM (bottom panel) regions. The tissue is stained for melanocytes (SOX10: yellow), endothelial cells (CD31: green), keratinocytes (PanCK: white), and tumor cells (S100B: magenta). Arrows mark examples of melanocytes and tumor cells. Scale bar, 20 μm.

(H) Correlation network sub-graph genes associated with S100B expression in mrSEQ data (PickSeq). Nodes represent genes, and the edges correspond to the correlation between them. Brown nodes represent the genes that belong to the S100B module. Selected genes are annotated.

(I) Mean expression of 35 genes identified within the S100B module in mrSEQ data (PickSeq). X-axis represents the mROIs grouped into the histopathological annotation category from which they were isolated.

(J) Fold-difference (log2) and significance (log 10 P_{adj}) for expression of 19,500 genes between EM (n=34) and IM (n=16) mROIs (Pick-Seq). DEGs above (brown) and below (blue/grey) a significance threshold (P-adjusted = 0.05) and above a fold change threshold (log2 fold change = 10) are indicated.

(K) GSEA for upregulation of KRAS pathway in IM (n=16) compared to EM (n=34) mROIs (PickSeq). FDR < 0.05.

(L) Expression (log2) of MYC, NFKB1, IGFBP2, IGF1R, and BCL2A1 in IM and EM mROIs (PickSeq). Data is mean ± SEM; *P<0.05, **P<0.01, ***P<0.001.

(M) Heatmap showing expression of genes (listed on the y-axis) known to play a role in epithelial to mesenchymal transition (PickSeq). All genes showed a significant difference between their mean expression in IM vs. EM mROIs (P<0.05).

(N) CyCIF image of MEL1-1 IM and EM regions stained for DNA (blue) tumor (SOX10: green), and KI67 (red). (left panel). The magnified regions (white boxes) are also stained for DNA (blue), p21 (green), p27 (red), cyclin D1 (D1: green), cyclin B1 (B1: white), and pRB (red). Scale bars, 100 µm.

Figure-S2 (Related to Figure 2)

(A) Location of mrSEQ specimens (PickSeq and GeoMX). The left panel shows whole slide CyCIF images of specimen MEL1-1 to MEL1-3 stained for epidermis (PanCK: cyan) and tumor cells (MART1: red). mrSEQ was performed in areas marked with a color-coded 'X' representing regions profiled by GeoMX (yellow), PickSeq (cyan), and both GeoMX and PickSeq (white). The top right panel shows a close-up view of the IM region where mROIs within the tumor (IM), invasive front (IB), and outside the tumor (bTIL) were extracted. The holes show tissue after PickSeq was performed. The bottom right panel shows the number of mROIs extracted by PickSeq and GeoMX between the histological regions. Scale bars, 5 mm.

(B) Expression of IRF1 between bTIL, IB, and IM (PickSeq). Data is mean ± SEM; **P<0.01.

(C) Kaplan-Meier plots showing survival difference between patients expressing high and low levels of BRI3, CDK2, MT-ND2, PMEL, SOX10, TBC1D7, TSPAN10, TYR in the TCGA melanoma dataset. All highlighted genes showed a significant difference in survival (P<0.05).

(D) Gene set enrichment analysis for upregulation of the EMT pathway in IM (n=16) compared to EM (n=34) mROIs. Derived using PickSeq data.

(E) Expression of DDX58 between EM and IM mROIs (GeoMX). Data is mean ± SEM; *P<0.05, **P<0.01.

(F) Density plot for the intensity (log2) of cyclin D1 and A2 protein expression in tumor cells. Dashed lines indicate log2 intensity gates for single-cell phenotyping.

(G) Pie charts (left panel), categorized by exophytic (top) or invasive (bottom) melanoma, showing the percent of tumor cells that stained positive for selected cyclin proteins. Bar plots (right panel) compare the percent of tumor cells in the EM versus IM region that positively stained for phospho-histone H3 (pHH3), phospho-RB1 (pRB), KI67, MCM2, and PCNA (positive: top decile for PCNA or MCM2 staining) as a function of cell cycle: no cyclins (early G1 or G0), cyclin D1 (G1), E2 (G1/S), A2 (early S), A2 co-staining B1 (late S), and B1 alone (G2/M). Co-expression of cyclin D1 with S/G2/M cyclins is depicted in an additional group and suggests a non-cell cycle role for cyclin D1. Cyclin E1-positive cells in the IM region were rare, and this phenotype was not analyzed further (asterisk).

(H) Bar plot showing the percent of tumor cells from the exophytic or invasive tumor region that stained for p21 and p27 organized into groups that expressed (i) no cyclin, (ii) cyclin D, (iii) a combination of A2 and/or B1, or (iv) KI67.

Figure-3: Single-cell analysis of invasive tumor

(A) t-distributed stochastic neighbor embedding (tSNE) of tumor cells derived from specimen MEL1-1, labeled by cluster assignment (T1-T5b). Out of 516,000 cells, 50,000 single-cells were randomly sampled to build the plot.

(B) Violin plots showing expression levels of protein markers across the six defined tumor clusters (T1-T5b). Color represents the scaled median expression of the indicated marker (y-axis) within the group. The fraction of total tumor cells within each cluster is indicated on top of the plot.

(C) Cell-to-cell proximity heatmap showing the presence of significant ($P < 0.01$) co-occurrence (yellow) or avoidance (violet) between cell types in specimen MEL1-1.

(D) Scatter plots mapping the physical location of the derived tumor clusters (T1-5b) in MEL1-1 (T1: purple, T2: green, T3: brown, T4: dark grey, T5a: red, T5b: blue).

(E) CyCIF images of MEL1-1 stained for S100A (top panel), MITF (middle panel) and S100B (bottom panel). Boxes represent regions highlighted in panel F. Scale bars, 3 mm.

(F) Insets from panel E of tumor region (IM) showing gradient expression patterns for MITF (top panel) and S100B (bottom panel). Contours describe averaged quantified marker expression.

(G) CyCIF field of view of MEL1-1 highlighting the spatial arrangement of MHC-II^{+} tumor cells at the invasive front found in tumor cluster T5b. Tumor cells were stained with SOX10 (cyan), MHC-I (HLA-A: green), and MHC-II (HLADPB1: red). Magnified regions outlined in magenta and yellow squares

illustrate MHC-II^{+} and MHC-II^{-} staining of tumor cell membranes. Scale bars, 25 µm (main image) or 5 µm (insets).

(H) Expression of CXCL10, CXCL11, IDO1, MIF, and CD74 among histological sites (PickSeq data). Values represent mean ± SEM; *P<0.05, **P<0.01, ***P<0.001, ns = not significant.

(I) Heatmap showing expression of CXCL12 and CXCR4 (GeoMX). Both genes showed a significant difference in their mean expression (P<0.05) of IR/bTIL compared to IM region.

Figure-S3 (Related to Figure 3):

(A) Principal Component analysis variance plot, showing the degree of variance captured by each principal component (PC) within the tumor cells (0.5M cells) in specimen MEL1-1. The plots to the right show the top loadings within PC1 and PC2.

(B) Regions of EM showing gradient expression patterns of S100B, MITF, and S100A. Contours represent averaged cell expression of the markers and are overlaid on single-cell data.

(C) CyCIF image at low (left panel) and higher magnification (right panel) showing CCND1^{high} (CCND1: purple) tumor cells (S100B: blue) in cluster T5a restricted to surrounding vascular features (CD31: green) in the EM and lining the perivascular space, co-extensive with myeloid cells (CD11C: cyan). Scale bars, 500µm (main image) or 50 and 20 µm (insets).

(D) CyCIF image of the MEL1-1 invasive tumor front stained for tumor (SOX10: purple), MHC-II positive (HLADPB1: yellow), and myeloid cells (CD11C: blue) (left). Line plot showing scaled fluorescence intensity of MHC-II (HLADBP1), SOX10, and CD11C within the tumor shown to the left, at, and outside the invasive tumor boundary. The locations of these boundaries are represented by dashed and solid grey lines. Scale bar, 100 µm.

(E) Gene set enrichment analysis for upregulation of JAK-STAT pathway (from Hallmark gene set) in bTIL region (n=16) compared to tumor regions (EM and IM) (n=50) mROIs. Derived using PickSeq data. P<0.05.

(F) Single-sample gene set enrichment analysis (ssGSEA) of JAK-STAT related pathways showing enrichment of the pathway in the bTIL region using mrSEQ data (GeoMX).

(G) Expression of MX1 and IFI16 between MIS, EM, and IM mROIs (PickSeq). Data is mean ± SEM; **P<0.01, ***P<0.001.

(H) CyCIF field of view of IM (left) and EM (right) stained for melanocytes (SOX10: cyan), macrophages (CD163: grey), and interferon signaling (MX1: red). Exposure and contrast settings are identical in both regions. Scale bar, 200 µm.

Figure-4: Spatial organization of cells within invasive tumor domains

(A) Scatter plot (left panel) showing a field of view of the IM region. Cells are colored based on their tumor cell community (TCC1-10). The yellow circle highlights the region in panel B. The right panel is a CyCIF image of the same field of view (from specimen MEL1-1) stained for CD163 (green), MITF (yellow), KI67 (red), and MHC-II (HLADPB1: blue). Scale bar, 200 µm.

(B) Voronoi diagram generated from a field of view at the apex of the invasive front (inset in panel A). Cells are colored based on the tumor cell community (TCC1-10) that they belong to.

(C) Bar plots showing the percentage of S100B, S100A, MITF, KI67, and MHC-II (HLADPB1) positive cells within each tumor cell community (TCC1-10).

(D) Scatter plot showing the scaled expression of KI67 and MITF of tumor cells in the IM region. The overlayed contour illustrates the density of the points. The stacked bar graph shows the proportion of cells that falls into each quadrant.

(E) CyCIF field of view of IM region of MEL1-1 stained for melanocytes (SOX10: blue) and myeloid cells (CD11C: green). The magnified regions indicated with yellow, purple, and red boxes highlight the $KI67^{+}$ (blue) and $MITF^{+}$ (red) tumor cells within these regions. Scale bar, 200 µm (main image) or 20 µm (magnified regions).

Figure-S4 (Related to Figure 4)

(A) Heatmap showing median expression of protein markers identified within TCC1-10 tumor cell communities. The bar plot on top of the heatmap shows the proportional estimate of the TCCs within histological annotations (EM, IM, or IB). The heatmap at the bottom shows the properties related to the shape of the cells (area, solidity, extent, and eccentricity) derived from the segmentation masks.

(B) Scatter plot mapping the physical location of the derived tumor cell clusters (TCC1-10: dark blue) in MEL1-1. Each subplot represents the location of cells within a tumor cell community and other cells in grey.

Figure-5: Recurrent cellular neighborhoods associated with melanoma progression

(A) UMAP of single-cell data from 70 ROIs in 12 patients. The plot was generated using 50,000 single-cells that were randomly sampled from the full dataset of $1.5x10^{6}$ cells. The UMAP is colored based on the phenotype (left), disease progression stage (center), and patient ID (right).

(B) UMAPs (shown also in panel A) representing feature plots of expression of selected protein markers.

(C) The percentage of $SOX10^{+}$ melanocytes or tumor cells expressing S100A within each stage of progression.

(D) Heatmap showing the abundance of cell types within the 30 LDA-based cellular neighborhood clusters (numbers to the right of the plot); these were then reduced to the 10meta-clusters (RCNs) shown to the left of the plot. The bar chart to the right of the heatmap depicts the distribution of progression stages within each cluster, and the bar chart to the left of the heatmap represents the distribution of patients within each cluster.

(E) Bar plot depicting the detailed breakdown of cell-type proportions within each RCN (RCN1-10; x-axis). Pie charts depicting a simplified breakdown of cell types in each RCN; myeloid (green; dendritic cells, CD11C+ macrophages, macrophages, and Langerhans cells), lymphoid (light orange; cytotoxic T cell: CTL, regulatory T cells: Treg and helper T cell: T helper), immune-suppressive (dark orange; PDL1+ DCs, PDL1+ Macs, PD1+ CTL), melanocytes (dark blue) and keratinocytes (yellow).

Figure-S5 (Related to Figure 5)

(A) Schematic of the Latent Dirichlet Allocation (LDA) analysis to identify RCNs. Single-cell data from 22-plex CyCIF of 71 ROIs annotated for the stage of melanoma progression from patients MEL1-MEL13 was used for cell type calling to identify 12 distinct cell phenotypes. A spatial-LDA model was trained with a 20 µm proximity radius and the latent weights were subsequently grouped using k-means clustering (k=30) into ten informative meta-clusters (RCN1-10**)** based on the cellular composition and the frequency of occurrence within the ROIs.

(B) Flowchart used in CyCIF experiment 2 depicting the strategy used for cell type calling.

(C) Voronoi diagram of RCN1 (top), CyCIF image (middle) with keratinocytes (PanCK: white), melanocytes (SOX10: cyan) and T cells (CD3: red), and the corresponding H&E (bottom) of the same region showing enrichment of RNC1 to the $panCK^{+}$ epidermis (marked with white arrows).

(D) Heatmap showing the abundance of cell types within the 30 (numbers to the right of the plot) derived cellular neighborhood clusters; as described in methods, a complementary approach was used to that shown in main panel 5D but the results were substantially the same. The clusters are grouped into meta-clusters shown to the left of the plot. The bar chart to the right of the heatmap depicts the distribution of progression stages within each cluster and the left bar chart represents the distribution of patients within each cluster.

(E) Line plot showing the decay of heterogeneity score with an increasing number of clusters (KMeans) in the x-axis. The latent space vectors of the LDA model were used for generating this plot.

Figure-6

(A) Scatter plot (top) showing a field of view of the IM region (specimen MEL1-1). The cells are colored based on recurrent cellular neighborhoods (RCN1-10) that they belong to. The yellow and blue boxes represent regions that are magnified in the bottom panel (left and right, respectively) depicted as Voronoi diagrams.

(B) Exemplary CyCIF images highlighting RCNs in the invasive front of specimen MEL1-1. The top panel shows an overall view of the invasive front stained for tumor cells (S100B: blue), macrophages (CD163: cyan), T cells (CD3: red), and dendritic cells (CD11C: green). The inset squares correspond to magnified panels at the bottom. The bottom left panel (yellow) highlights RCN9 enriched for dendritic cells (CD11C: green) at the tumor-stroma junction; the bottom center panel (blue) highlights RCN5/8 enriched with $PD1^+$ CTLs (CD8: green; PD1: red) and bottom right panel (red) highlights RCN3/4 enriched with myeloid cells (CD163: magenta; CD11C: green). Scale bar, 100 μm; the dashed grey line represents the tumor-stroma boundary.

(C) Voronoi diagrams of a representative field of views compiled from regions of N, P, and MIS. Each cell is colored based on the recurrent cellular neighborhood (RCN1-10) to which it belongs (as in panel A). Examples of corresponding CyCIF images from one patient in each case are provided at the bottom row. A magnified view is available in panel S6A.

(D) Bar plot depicting the proportional distribution of RCNs (RCN1-10) among the disease progression stages (N, P, MIS, IM, and EM).

(E) Box plots of the distribution of the shortest distance between cells in RCN 2-7 and RCN10 grouped based on progression stages. T-test (*$P<0.05$) depicts significant changes in mean distances between the compared stages. The comparison made is described on the upper right corner of each plot (e.g., N vs P).

(F) Shift plot shows the distance between melanocytes and CTLs, $PDL1^+$ myeloid cells, and Tregs in normal (top) and precursor (bottom) regions. Significance is calculated for each percentile (10, 20, 30, 40, 50, 60, 70, 80, 90) using the robust Harrell-Davis quantile estimator. Red indicates a significant difference ($P<0.05$) and grey represents non-significance for each percentile.

Figure-S6 (Related to Figure 6)

(A) The corresponding H&E images (left column) for normal (MEL11), precursor (MEL1) and MIS (MEL8) ROIs are shown in panel 6C. Four of the CyCIF images presented in panel 6C are magnified in the middle and right columns (MEL11 top left, MEL1 top right, MEL8 bottom panel). The highlighted cell types are melanocytes (SOX10: cyan), keratinocytes (PanCK: white), T cells (CD3: orange), macrophages (CD163: green), dendritic cells (CD11C: purple), $PD1^+$ CTLs (PD1: yellow, CD8: red) and $PDL1^+$ myeloid cells (PDL1: cyan). Scale bar, 50 µm.

(B) Swarm plot showing the percent frequency (number of cells belonging to RCN9 divided by the total number of cells within the ROI) of RCN9 between the progression stages. *P<0.05.

(C) Bar plot of the proximity volume scores across progression stages calculated between $CD11C^+$ myeloid cells and melanocytes.

(D) Scatter plots highlighting cells within RCN2 (top panel) and RNC3 and 4 (bottom panel). RCN2 is spatially restricted to the dermis, while RCN3/4 is more prevalent surrounding the tumor and in the vascular spaces within the tumor.

(E) Heatmap showing the differences in the frequency of RCN1-10 between progression stages. The significant comparisons (P <0.05) in the RCN frequency between the stages compared are indicated in cyan or red, non-significant comparisons in grey. The comparisons made for each RCN are indicated at the top of the heatmap.

Figure-7

(A) Field of MIS from a whole slide CyIF image of MEL1-1. A $PDL1^+$ melanocyte (SOX10: white, PDL1: green) and CTLs (CD8: red) are being highlighted with an orange box (left panel). The right panel illustrates the polarization of PD1 (red) and PDL1 (green) to the point of contact between the interacting cells. Scale bar, 5 or 10 µm.

(B) Line plot showing the percentage of ROIs that displayed significant (P<0.05) co-occurrence based on proximity analysis performed between $PDL1^+$ CD11C+ CD163- dendritic cells and $PD1^+$ CTLs.

(C) Field of IM from a whole slide CyCIF image of MEL1-1 stained for tumor (SOX10: red), macrophages (CD163: green), and CTLs (CD8: white), with three fields of macrophage-CTL contacts (yellow boxes). Maximum-intensity projections imaged at high-resolution in fields 1 and 2 are stained for DNA (blue), PDL1 (red), and PD1 (green) with cells labeled as myeloid cells (M) and engaged T-cells (T); field 3 shows tumor cells (SOX10: red), CTLs (CD8: white) and a macrophage (CD163; green). Inset white boxes in the bottom right panel show concentration of PD1 (red) and PDL1 (red) to

the point of contact and the long connection between a macrophage (CD163: white) and a CTL is shown in a 3D reconstruction of the field 3. Scale bar, 25 µm, 10 µm or 4 µm.

(D) Left panel shows the same CyCIF field of view as in panel C, stained for DNA (blue), TIM3 (red), and CD8A (green). The white inset box illustrates the staining of one $CD163^{+}$ $CD11C^{+}$ $TIM3^{+}$ myeloid cell next to a CTL (right panel). Scale bar, 25 µm.

(E) Maximum intensity projection from bTIL region (upper left panel) stained for DNA (blue), macrophages (CD163: green), and T cells (CD3D: white). The white inset is magnified and stained for T cell polarity (CD4: green, CD8: red), PD1-PDL1 axis (PD1: green, PDL1: red), and exhaustion markers (TIM3: red, LAG3: green). A Treg in this field is indicated with a label Tr. Scale bars, 20 and 10 µm.

(F) Stacked bar graph showing the proportions of lymphoid and myeloid cells between the histological regions (IR, MIS, bTIL) in specimen MEL1-1.

(G) CyCIF maximum-intensity projection images of MEL1-1 of the region of inflammatory regression (shown in panel 1C). Fields are stained for DNA (blue), PD1 (green), and MHC-II (HLA-DPB1: magenta). The dermal-epidermal junction is indicated with a dashed white line. The bar plot shows the proportions of all cell types in the epidermis (upper plots), with lymphocyte and myeloid subset further highlighted, and in the dermis (lower plots); color code is as in panel F. Scale bar 25 µm.

(H) Heatmap showing expression of genes related to immune checkpoints and T cell activation between histological mROIs in patient MEL1 (GeoMX). Significant upregulation in comparison to the EM region ($P<0.05$) is highlighted in red, non-significant in grey.

(I) Schematics of remodeling of the tumor microenvironment with disease progression; see text for details.

(J) Summary of mechanisms of immune suppression detected in sample MEL1-1.

Figure-S7 (Related to Figure 7)

(A) CyCIF image of MIS region of MEL1-1 (top left; same as in panels 1G and S1E), stained for DNA (blue), tumor (MITF: magenta), and T cells (CD3: yellow). A single-optical section (z: 0 µm) of high-resolution CyCIF stained for tumor (SOX10: white) and T cells (CD3: green, CD8: red) is shown in the panel top right (magnification of the inset from the left panel). Below, magnified region of the cell-to-cell interaction (cyan box) with three optical sections (z: -0.2, 0, +0.2 µm) stained for PD1 (red) and PDL1 (green) and a composite image. Scale bars, 50 µm, 10 µm or 3 µm.

(B) CyCIF image of IM region of MEL1-1 stained for tumor (MITF: white), T cells (CD3: yellow), and myeloid markers (CD163: red, CD11C: magenta). Regions of high-resolution imaging (orange, red, and

cyan boxes) and tumor margin (white dashed line) shown in panel C are being indicated. Scale bar, 100 µm.

(C) CyCIF whole slide (10x; the five panels on the left) and maximum-intensity projection high-resolution (60x; the three panels on the right) images of regions in panel B (orange, red, and cyan boxes). The tumor margin is indicated with a dashed line. Scale bar, 50 µm.

(D) CyCIF maximum-intensity projection images of MEL1-1 corresponding to fields of MIS, IR, and terminal regression as indicated in panel 1C. Fields are stained for DNA (blue), PD1 (green), and HLA-DPB1 (magenta). The dermal-epidermal junction, identifying the epidermis and dermis, is indicated with a dashed white line. Scale bar, 50 µm. The bar graph shows the cell type composition for the corresponding histologic regions indicated in panel 1C.

STAR Methods

Contact for reagent and resource sharing

This manuscript does not contain any unique resources and reagents; all data is provided for download without restrictions. Any questions should be directed to the lead contact Peter Sorger (peter_sorger@hms.harvard.edu).

EXPERIMENTAL MODEL AND SUBJECT DETAILS

Clinical samples

Using medical records and pathological review of hematoxylin and eosin (H&E) stained diagnostic specimens, we retrospectively identified 13 patients with tissue samples containing various stages of melanoma progression (**Table S1 and S2**). The samples were retrieved from the archives of the Department of Pathology at Brigham and Women's Hospital and collected under the Institutional Review Board approval (FWA00007071, Protocol IRB18-1363), under a waiver of consent. Fresh formalin fixed paraffin embedded (FFPE) tissue sections were cut from each tumor block. The first section of each block was H&E stained and used to annotate regions of interest (ROIs; **Table S3**). The remaining subsequent FFPE slides were used for cyclic multiplex immunofluorescence imaging (CyCIF) experiments to characterize markers of melanoma progression and the features of the immune microenvironment within various stages of melanoma. A specimen from a single patient MEL1 (samples

MEL1-1, MEL1-2 and MEL1-3) was selected for a deeper profiling with CyCIF and high-resolution imaging, in addition to microregion transcriptomics (PickSeq, GeoMX).

Based on the melanoma diagnostic criteria, the histopathological annotations included normal skin (N), melanoma precursor lesions (P: melanocytic atypia, dysplasia, and hyperplasia), melanoma in situ (MIS), vertical growth phase of melanoma (VGP), radial growth phase of melanoma (RGP), invasive (IM) and nodular melanoma (NM); the exophytic component polypoid melanoma was labeled as exophytic melanoma (EM). These ROIs were further classified and subdivided based on the presence of immune infiltrate (brisk TIL (bTIL), inflammatory regression (IR), none) and various histologically distinct structures (epidermis, dermis, invasive front (IB)). The bTIL region was defined as a dense lymphocytic infiltrate in the stroma adjacent to the invasive tumor. IB was defined as the tumor region extending ~20 μm from the tumor-stroma interface.

METHOD DETAILS

Imaging (H&E and t-CyCIF)

H&E stained FFPE slides were digitized using an Olympus VS-120 automated microscope using a 20x objective (0.75 NA) at the Neurobiology Imaging core at Harvard Medical School. CyCIF was performed as-described in (Lin et al., 2018) and at protocols.io (dx.doi.org/10.17504/protocols.io.bjiukkew). In brief, the BOND RX Automated IHC Stainer was used to bake FFPE slides at 60°C for 30 min, dewax using Bond Dewax solution at 72°C, and perform antigen retrieval using Epitope Retrieval 1 (Leica^{TM}) solution at 100°C for 20 min. Slides underwent multiple cycles of antibody incubation, imaging, and fluorophore inactivation. Antibodies were incubated overnight at 4°C in the dark; in contrast to the protocol.io method, this was performed using a solution that also included Hoechst 33342 for DNA staining. Before imaging, glass coverslips were wet-mounted using 100 μL of 70% glycerol in 1x PBS. Images were acquired using a CyteFinder® slide scanning fluorescence microscope (RareCyte Inc. Seattle WA) with a 20x/0.75 NA objective. Slides were soaked in 42°C PBS to facilitate coverslip removal; then fluorophores were inactivated by incubating slides in a solution of 4.5% H_2O_2 and 24 mM NaOH in PBS and placing them under an LED light source for 1 hr. The list of all antibody panels used in the experiments is presented in **Table S4**.

One FFPE section from sample MEL1-1 was imaged with CyCIF at high-resolution using a DeltaVision ELITE microscope (Cytiva; formerly GE Sciences) equipped with a 60x/1.42NA oil-immersion objective and an Edge 4.2 (PCO) sCMOS camera. For accurate deconvolution, an oil

refractive index of 1.524 was selected through optimizing multiple acquired point-spread functions as it provided the highest image quality. The slide was wet-mounted with a high-precision 1.5-grade coverslip (ThorLabs CG15KH1) using 105 µL of 90% glycerol. The fields for image acquisition were selected by evaluating SOX10 staining to locate and identify melanocytes and tumor cells, yielding a total of 42 fields across the annotated regions (**Figures 1C** and **S1D**). Images were acquired in 5 µm Z-stacks at 200 nm step size to create a 3D representation of the sample. Excitation wavelengths were: 632/22 nm, 542/27 nm, 475/28 nm, 390/18 nm for four-channel imaging.

Microregion transcriptomics

the microregion transcriptomic profiling (mrSEQ) using PickSeq and GeoMX, we identified micro-regions (mROIs) of MIS, EM, IM, IB, IR, and bTIL from samples MEL1-1, -2, and -3 based on the corresponding H&E-stained sections. Freshly cut serial sections from the corresponding tissue blocks were used for the mrSEQ experiments.

PickSeq processing and library preparation

PickSeq is a method by which 40 µm mROIs of interest is physically extracted using a robotic arm followed by mRNA extraction and RNA sequencing (Maliga et al., 2021). 222 ROIs representing five morphologically distinct sites (MIS, IM, IB, bTIL, EM; **Figure S2A**) were selected for collection and library preparation. The FFPE sections were deparaffinized and rehydrated using the Histogene Refill Kit (Arcturus). Slides were immersed in xylene for 5 min, a second jar of xylene for 5 min then incubated in a series of ice-cold solutions with 0.0025% RNasin Plus (Promega): 100% ethanol for 1 min, 95% ethanol for 1 min, 75% ethanol for 1 min, 1X PBS for 1 min, and another tube of 1X PBS for 1 min. Slides were stained with 50 µM DRAQ5™ a Far-Red DNA Dye (ThermoFisher) in PBS, with 0.1% RNasin Plus for 2 min on ice. Sections were dehydrated in a series of ice-cold solutions with 0.0025% RNasin Plus: 1X PBS for 1 min, 1X PBS for 1 min, 75% ethanol for 1 min, 95% ethanol for 1 min, 100% ethanol for 1 min. Slides were left in ice-cold 100% ethanol before mROI retrieval.

For mROI retrieval, the slides were loaded into a CyteFinder instrument (RareCyte) and retrieved using the integrated CytePicker module with 40 µm diameter needles. The retrieved tissue mROIs were deposited with 2 µl PBS into PCR tubes containing 18 µl of lysis buffer: 1:16 mix of Proteinase K solution (QIAGEN) in PKD buffer (QIAGEN), with 0.1% RNasin Plus. After deposit, tubes were immediately placed in dry ice and stored at -80°C until ready for downstream RNA sequencing workflow.

PCR tubes containing tissue microregions in the lysis buffer were removed from the freezer, allowed to thaw at room temperature for 5 min, and incubated at 56°C for 1 hr. Tubes were briefly vortexed, spun down, and placed on ice. Dynabeads Oligo(dT)25 beads (ThermoFisher) were washed three times with ice-cold 1X hybridization buffer (NorthernMax buffer (ThermoFisher) with 0.05% Tween 20 and 0.0025% RNasin Plus), and resuspended in original bead volume with ice-cold 2x hybridization buffer (NorthernMax buffer with 0.1% Tween 20 and 0.005% RNasin Plus). A volume of 20 µl of washed beads was added to each lysed sample, mixed by pipette, and incubated at 56°C for 1 min followed by room temperature incubation for 10 min. Samples were placed on a magnet and washed twice with an ice-cold 1X hybridization buffer, then once with ice-cold 1X PBS with 0.0025% RNasin Plus. The supernatant was removed, and the pellet was resuspended in 10.5 µl nuclease-free water. Samples were incubated at 80°C for 2 min and immediately placed on a magnet. The supernatant was transferred to new PCR tubes or plates, and placed on ice for subsequent whole transcriptome amplification or stored at -80°C.

Reverse transcription and cDNA amplification were performed using the SMART-Seq v4 Ultra Low Input RNA Kit for Sequencing (Takara Bio, Kusatsu, Shiga, Japan). The resulting amplified cDNA libraries were assessed for DNA concentration using the Qubit dsDNA HS Assay Kit (ThermoFisher) and for fragment size distribution using the BioAnalyzer 2100 High Sensitivity DNA Kit (Agilent). The sequencing libraries were prepared with ThruPLEX DNA-seq Kit (Takara Bio). The resulting libraries were characterized by using the Qubit dsDNA HS Assay Kit and BioAnalyzer 2100 High Sensitivity DNA Kit, pooled at equimolar ratios, and sequenced using a MiSeq (Illumina) or NextSeq (Illumina) sequencer.

GeoMX processing and data collection

NanoString GeoMx gene expression analysis utilizing the cancer transcriptome array (CTA) probe set was performed by the Technology Access Program at NanoString using previously described methods (Demirkan et al., 2020). Briefly, a 5 µm section of FFPE melanoma was dewaxed and stained overnight with antibodies targeting melanocytes (PMEL), epithelial (pan-cytokeratin), and immune cells (CD45) defining cell morphology and highlighting regions of interest. The section was hybridized with the CTA probes before being loaded into the instrument. Seventy ROIs representing five morphologically distinct sites (MIS, IM, IB, bTIL, EM; **Figure S2A**) were selected for collection and library preparation. All sample processing and sequencing were performed by the Technology Access Program at NanoString. Probe measurements, and quality control data were provided by NanoString.

QUANTIFICATION AND STATISTICAL ANALYSIS

3D image processing, alignment, and visualization

Acquired images were deconvolved using constrained iterative in SoftWorx to reassign photons to the focal plane and increase image contrast. Maximum intensity projections were also generated. Subsequently, cycles were aligned using a custom script written in MATLAB (Mathworks). Briefly, 2D image registration was first carried out using the Hoechst channel maximum intensity projections. This was followed by registration along the z-axis. The registered 3D datasets were visualized in Imaris (Bitplane) and surface rendered for visualization.

PickSeq data Alignment and expression matrix generation

The raw FASTQ files were examined for quality issues using FastQC (http://www.bioinformatics.babraham.ac.uk/projects/fastqc/) to ensure library generation and sequencing were suitable for further analysis. The reads were processed using the *bcbio* pipeline v.1.2.1 software (Guimera, 2011). Briefly, reads were mapped to the GRCh38 human reference genome using *HISAT2* and Salmon. Length scaled transcripts per million (TPM) derived from *Salmon* were used for the downstream analysis.

Differential gene expression and pathway analysis

DESeq2 R package was used to generate the normalized read count table based on their estimateSizeFactors() function with default parameters by calculating a pseudo-reference sample of the geometric means for each gene across all samples and then using the "median ratio" of each sample to the pseudo-reference as the sizeFactor for that sample. The sizeFactor was then applied to each gene's raw count to get the normalized count for that gene. *DESeq2* (Love et al., 2014) was used for differential gene expression analysis. A corrected P-value cut-off of 0.05 was used to assess significant genes that were up-regulated or down-regulated using Benjamini-Hochberg (BH) method. Principal component analysis (PCA) was performed using the *prcomp* R package. A compendium of biological and immunological signatures was identified from publicly available databases or published manuscripts for performing enrichment analysis. To perform gene set enrichment analysis, two previously published methods (Gene Set Enrichment Analysis (GSEA) and single-sample GSEA (ssGSEA)) were primarily used. The R package *clusterProfiler* was used to perform GSEA and the R package *GSVA* was used to perform ssGSEA which calculates the degree to which the genes in a particular gene set are coordinately

up- or down-regulated within a sample. The KRAS and JAK-STAT were curated from MSigDB (Subramanian et al., 2005), and immune cell-related and melanoma-related signatures were curated from published studies (Nirmal et al., 2018; Shih et al., 2017; Tirosh et al., 2016).

Network analysis to identify genes within S100B module

The normalized expression matrix (PickSeq data) was loaded into the network analysis tool BioLayout (Theocharidis et al., 2009). Within the tool, a Pearson correlation matrix was generated, i.e., an all versus all comparison of expression profiles across all samples. A gene correlation network (GCN) was then generated using a correlation threshold value 0.6. In the context of a GCN, nodes represent genes and edges represent the correlations between them. A single-step neighbor walk was performed within the tool from S100B to determine the S100B module.

CyCIF image preprocessing and quality control

The complete preanalytical CyCIF image processing (stitching, registration, illumination correction, segmentation, and single-cell feature extraction) was performed using the MCMICRO pipeline (Schapiro et al., 2021), an open-source multiple-choice microscopy pipeline, versions 60929d5b82 and 7547d0c42a (full codes available on GitHub https://github.com/labsyspharm/mcmicro). For the generation of probability maps and the nuclei segmentation, a trained U-Net model UnMicst v1 was used followed by a marker-controlled watershed used for single-cell segmentation (Yapp et al., 2021). A diameter range of 3 to 60 pixels was used for nuclei detection. The cytoplasmic area was captured by expanding the nuclei mask by 3 pixels. After generating the segmentation masks, the mean fluorescence intensities of each marker for each cell were computed, resulting in a single-cell data table for each acquired whole-slide CyCIF image. The X/Y coordinates of annotated histologic regions on the whole-slide image were used to extract the quantified single-cell data of cells that lie within the ROI range.

Multiple approaches were taken to ensure the quality of the single-cell data. On the image level, the cross-cycle image registration and tissue integrity were reviewed; regions that were poorly registered or contained severely deformed tissues and artifacts were identified, and cells inside those regions were excluded. Antibodies that gave low confidence staining patterns by visual evaluation were excluded from the analyses. The quality of the segmentation was assessed and the segmentation parameters were iteratively modified to improve the accuracy of the segmentation masks. On the single-cell data level,

correlations of DNA staining intensities in different cycles were used to filter out cells that were lost in the cyclic process with a threshold of correlation coefficient less than 0.8.

Single-cell phenotyping

We first applied unsupervised graph-based clustering approaches such as Leiden and Phenograph on the derived single-cell data (data not shown) to identify cell types discernable in the CyCIF dataset. However, unlike single-cell RNASeq data, many cell types (especially immune cells) do not form distinct clusters (likely owing to low dimensionality) leading to ambiguity in cell type assignment especially for cells that lay at the boundaries between clusters. Therefore, we developed a gating-based phenotyping approach to classify cells (Baker et al., 2020). First, an open-source OpenSeadragon based visual gating tool (https://github.com/labsyspharm/cycif_viewer) was used to derive gates (the cut-off value that distinguishes cells that express and do not express a particular marker). The identified gates for each marker were subsequently used to rescale the single-cell data between 0 and 1 such that the values above 0.5 identify cells that express the marker and vice-versa (*rescale* function within *scimap*). We repeated this process on every image and merged them into a single large single-cell dataset. The scaled single-cell data was used for cell type calling. We built an algorithm (*phenotype_cells* function within *scimap* python package) that assigns phenotype labels to individual cells based on a sequential probability classification approach. An input to this algorithm is a relationship chart (phenotyping workflow, **Figure S1C**, **S5B,** and **Table S5**) between markers and cell types (phenotypes). Each cell wasis binned into a phenotype class based on the probable expression of a given marker (e.g., if a cell expresses higher levels of CD8versus CD11Cit is classified as a T cell rather than a cell of myeloid lineage). If a cell does not express any of the markers (i.e., < 0.5) in the phenotyping workflow sheet, it is assigned to an unknown class. By using “AND, OR, ANY, ALL” as parameters, in combination with “POS or NEG” expression patterns, we were able to define the desired cell types identified via unsupervised clustering and manual inspection of the images. The assigned cell types were then verified by overlaying the phenotypes onto the image using Napari (*image_viewer* function within *scimap*). In total, we assigned phenotype labels to $1.7*10^6$ single cells from 70 CyCIF ROIs corresponding to all progression stages (specimens MEL2-MEL13) and a whole slide dataset from specimen MEL1-1.

K-means clustering of tumor cells to define intra-tumor heterogeneity

The tumor cells from MEL1-1 (0.51M) were clustered using the K-means algorithm (k=10) based on the expression of 30 protein markers (shown in panel 1 in **Table S4**) using the *sklearn.cluster.KMeans* function in python. The clusters were then manually grouped (hierarchical clustering assisted) into meta-clusters based on the similar expression pattern of melanocyte and functional markers (SOX10, S100B, MITF, KI67, PCNA, S100A, CCNA2, CCND1, CD63).

Phenotype co-occurrence analysis

For each cell in the CyCIF dataset, its local neighborhood was captured by querying a radius of 20 µm from the cell centroid as measured by Euclidean distance between X/Y coordinates. The phenotypes of these cellular neighbors were mapped to generate a neighborhood matrix containing the neighbor phenotype for every cell. We then randomly permutated (1,000 times) the neighborhood phenotypes without changing the number of neighbors (to maintain the tissue structure) and generated 1,000 random cell-cell neighborhood matrices. The frequency of all cell-to-cell pairwise proximity from the real neighborhood matrix was compared with the 1,000 randomly generated neighborhood matrices to identify significant proximity or avoidance between pairs of cell types. The p-values were derived for every pairwise proximity according to the following formulas:

$$z_{ij} = \frac{(c_{ij} - \mu_{ij})}{\sigma_{ij}}$$

cij is the number of times the *ith* cell type was found proximal to the *jth* cell type. Its associated P-value *pij* was calculated by

$$p_{ij} = \operatorname{erfc}\left(\frac{z_{ij}}{\sqrt{2}}\right)$$

where erfc is the complementary error function calculated using the python function '*scipy.stats.norm.*sf'. The method is implemented under the *spatial_interaction* function in the *scimap* python package.

Spatial lag analysis to define tumor cell communities

For each tumor cell in the CyCIF dataset (MEL1-1), its local neighborhood was captured by querying a radius of 20µm from the center cell as measured by Euclidean distance between X/Y coordinates. A spatial lag vector was derived for each neighborhood by taking the product of the

expression matrix and a weighted proximity matrix. The weights were assigned such that the closest cell within a neighborhood received the highest weight (weight = 1) and the farthest received the lowest weight (weight = 0). The weights were then normalized to account for the number of cells within each neighborhood. The spatial lag matrix was then clustered using Python's *scikit-learn* implementation of *KMeans* with k = 20 and manually grouped (hierarchical clustering assisted) into meta-clusters (10 clusters) based on similar expression patterns visualized using a heatmap. The method is implemented under the *spatial_expression* function in *scimap* python package.

Proximity volume scoring

To quantify the abundance of cell-to-cell proximity between cell types of interest (COI) observed in CyCIF images, we developed a scoring system that weighs user-defined proximity patterns. The proximity volume score is defined as the proportion of COI found in proximity to each other (10 µm) compared to the total number of cells within that image. We calculated the spatial volume score between cell types of interest (tumor and $CD11C^{+}$ myeloid cells) for each image and averaged them across images belonging to the same stage. The scoring is implemented under the *spatial_pscore* function in *scimap* python package.

Recurrent cellular neighborhood (RCN) analysis to identify microenvironmental communities

For every single cell from specimens MEL1 to MEL13, its local neighborhood was captured by querying a radius of 20µm from the center cell as measured by Euclidean distance between X/Y coordinates. The cells within each neighborhood were mapped to the cell-type assignment made and their frequency within each neighborhood was computed. The frequency matrix was then used for microenvironment modeling using a method called Latent Dirichlet Allocation (LDA) which is commonly used in the natural language processing (NLP) and information retrieval (IR) community. Python's *gensim* (https://pypi.org/project/gensim/) implementation of LDA model estimation was used to train the algorithm. The number of latent motifs to be extracted from the training corpus was determined empirically (motifs = 10). The latent vectors (weights) were recovered from the model and clustered using *scikit-learn* implementation of *KMeans* with k = 30. The optimal number of *KMeans* clustering was determined by looking for the elbow point in the computed cluster heterogeneity during convergence. A fairly lenient elbow point (k = 30) was used to capture the maximal variance in our dataset and to account for smaller communities. The clusters were then manually grouped (hierarchical

clustering assisted) into meta-clusters (11 clusters) based on similar microenvironmental community patterns. To validate the RCN assignment, these meta-clusters were overlaid on the original tissue H&E-stained and fluorescent images. For example, RCN1 generally mapped to the epidermis capturing structural components of the data whereas RCN8 mapped to regions of immune suppression (with a high abundance of $PD1^{+}$ T cells) capturing communities of functional importance. In parallel, we also derived RCNs using an alternative approach, whereby we directly cluster the cell-type frequency table generated before feeding into the LDA model. We were able to identify similar communities (**Figure S5D**) thereby validating the communities that we describe using an alternative approach. However, we believe the LDA model was more robust to noise compared to directly clustering the cell-type frequency table. The method is implemented under the *spatial_count* function and the LDA approach is implemented under the *spatial_lda* function in *scimap* python package.

Statistical tests

All statistical tests to infer P-value for significant differences ($P < 0.05$) in mean was performed using Python's *scipy* implementation of the t-test.

Data and software availability

Micro-region sequencing (mrSEQ) data is available via GEO (GSE171888). All full resolution images derived image data (e.g., segmentation masks) and all cell count tables will be eventually publicly released via the NCI-recognized repository for Human Tumor Atlas Network (HTAN; https://humantumoratlas.org/) at Sage Synapse. Several of the figure panels in this paper are available with text and audio narration for anonymous online browsing using MINERVA software, which supports zoom, pan, and selection actions without requiring the installation of software. All image analysis methods are implemented in a python package *'scimap'*, which is available open-source (https://pypi.org/project/scimap/).

Pre-Publication Data Access: We recommend the introductory MINERVA story HTA MEL Atlas 1: Introduction to the MEL Atlas. One of the "discoveries" in *Nirmal et al* (2021) is the identification of large scale contiguous graded expression patterns displayed by key melanoma markers and distinct localization of specific tumor-cell states within the tumor, both of which were discernable only with whole-slide imaging (see **Figure 3, 4**). Whole slide imaging is also an FDA requirement for any diagnostic application. The images in *Nirmal et al (2021)* comprise 20 whole-slide multiplexed images

(plus 16 H&E), each with a sample diameter extending up to ~2.9 cm. Fluorescence imaging of each section required the collection of ~15,200 four-channel megapixel images (450 to 1200 tiles for each section x ~20 CyCIF cycles) for a total of 3.0 x 10^5 tiles and ~2.3 TB of primary image data. Data collection is not a major challenge for a modern scanning microscope but data management requires special tools.

HTAN has developed a set of methods (also described in https://mcmicro.org/) to create single multi-dimensional OME-TIFF 6.0 image mosaics from all of the tiles and wavelengths that derive from imaging a single specimen. Thus, instead of thousands of tiles, users of our data need only access one multi-spectral image per specimen. This can be accomplished by download, transfer within the cloud (Amazon Web Services S3), or using the MINERVA browser described below. Single-cell data derived from images in *Nirmal et al* are in the form of one *Spatial Feature Tables* (Level 4 data) per specimen; these tables are analogous to count tables in scRNAseq.

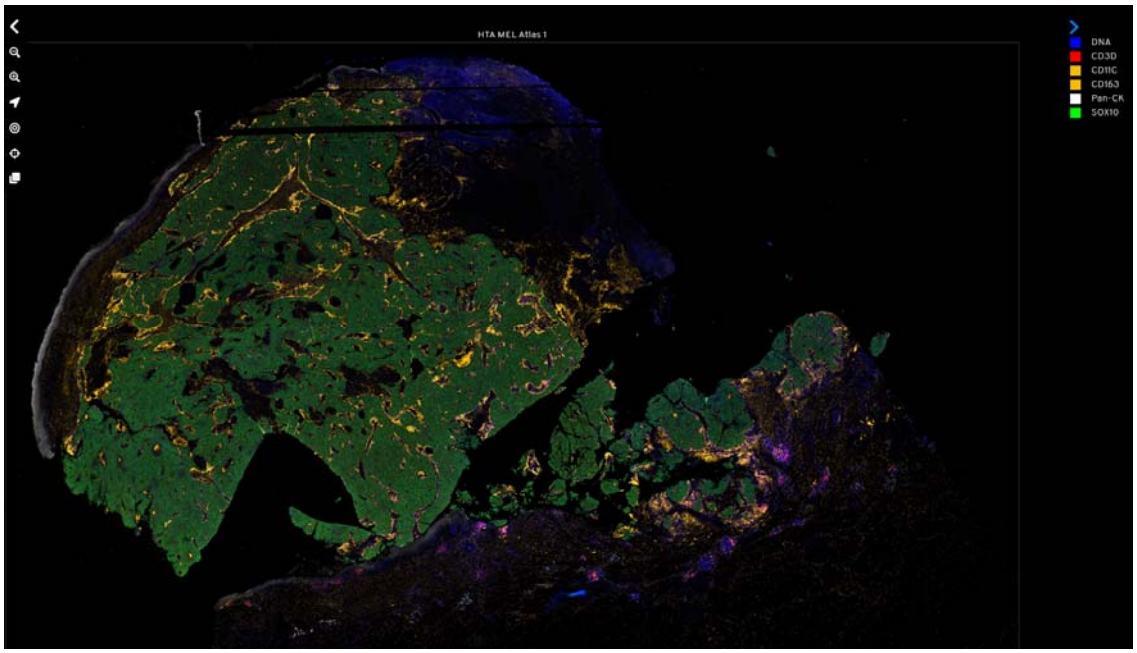

Fig 1. Exemplary MINERVA window of a "data overview" at low magnification for each analyzed tumor sample in the PCA dataset. All channels used for analyses or passed quality control can be accessed via a control panel to the right (not show). This window represents a fast way to review a minimally processed version of ~2.3 TB of Level 2 image data.

In-Browser Data Access: Gigapixel images cannot be opened with normal desktop software. HTAN has therefore created the open-source MINERVA software tool that functions like Google Maps but for tissue images. Both minimally processed Level 2 images (primary data) and guided narratives (an analog of figures) are available in MINERVA. We intend for the latter to be keyed to figure panels in a final manuscript, making the data more accessible and intelligible. All MINERVA stories are hosted on

AWS S3 and accessed via a web page hosted on GitHub. MINERVA can be opened in a browser and require no software installation so it presents no security risk:

- https://labspharm.github.io/HTA-MELATLAS-1/

Post-publication Data Access All primary and processed data in this paper, as well as all MINERVA stories) will be made publically available without restriction at or before the time of publication per NCI Human Tumor Atlas Network (HTAN) Moonshot policy. This will occur via the data portal at https://htan-portal-nextjs.vercel.app/, which will become an NCI resource for spatial 'omics similar to The Cancer Genome Atlas (TCGA).

Brief Description of MINERVA. MINERVA (Hoffer et al., 2020; Rashid et al., 2020) enables intuitive real-time exploration of very large (gigapixel) high-plex images on the cloud using a web browser. With MINERVA, users can pan around and magnify areas of an image and switch between channels. Users interested in the tool itself are directed to the documentation, the software publication, and a general description of digital docents.

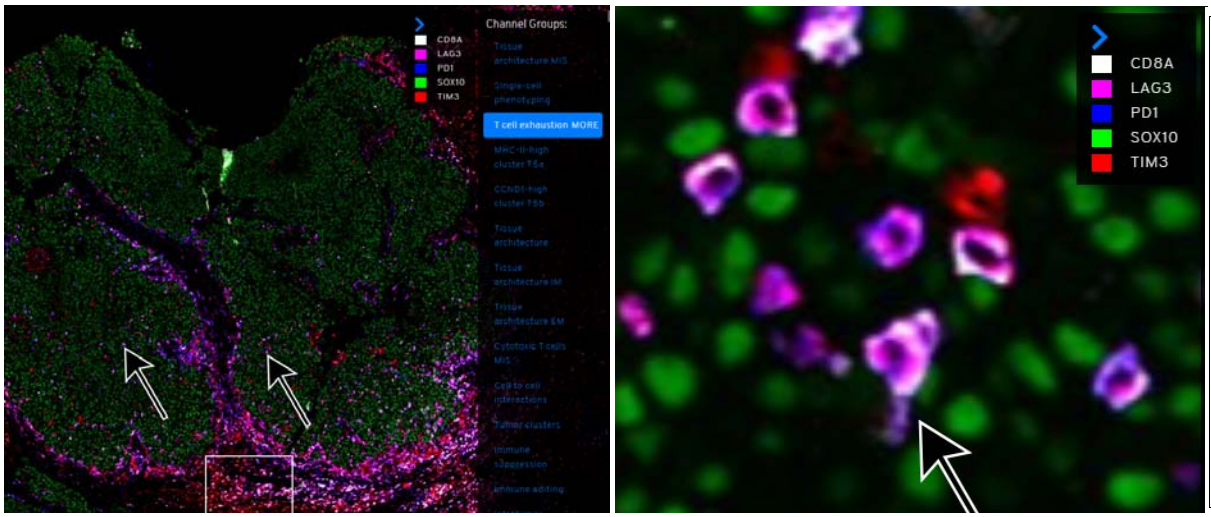

Fig 2. Varying zoom level in a MINERVA browser for the specimen MEL1-1 provides insight into immune infiltration; higher magnification (right) illustrates that the CD8+ lymphocytes infiltrating the tumor areas are terminally exhausted.

We provide two types of MINERVA stories with this paper.

- "***Data Overviews***" which provide access to minimally processed Level 2 images with annotation and interpretation kept to a bare minimum (Figures 1 and 2). Scaling is not necessarily optimal and artifacts have not been removed.

- **"*Data Explorations*"** which are like museum guides and exploit the digital docents in MINERVA to guide readers through the complexities of a large image via a series of narrated stories and waypoints (points of reference in the image that are used for navigation). Both written and audio narration are supported, as well as free exploration. These will be linked to individual figure panels in a final manuscript (an example is shown in Figure 3).

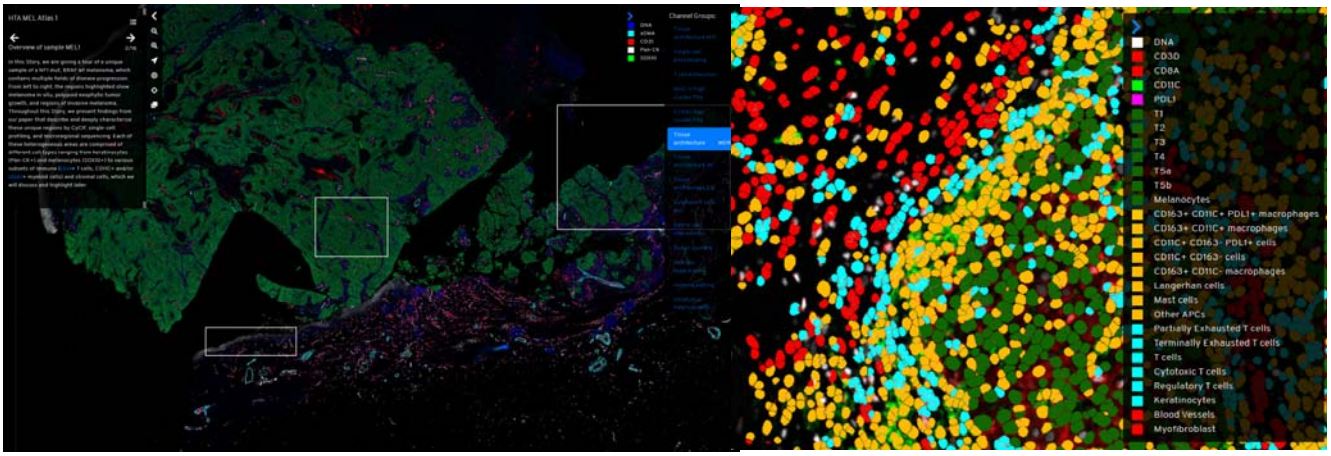

Fig. 3. MINERVA window for MEL1 "data exploration" (at low zoom, left) showing overall structure of section MEL1-1. Note that 16 different story way points are available (upper left panel) and the cells have been pseudo colored based on four functional or lineage markers (right). The right view highlights detailed cell type calling and clustering results. These represent types of Level 4 data.

Addendum: Proposed data levels for antibody-based multiplexed tissue Imaging

The concept of "data levels" (or tiers) was first developed by the Cancer Genome Atlas (TCGA) and Genomic Data Commons (GDC) to standardize the transformation of raw data (as generated by a measurement apparatus) into processed and interpreted data as used in research publications. This promotes uniform and reproducible data analysis and interpretation (Zhang et al, 2021). For TCGA and GDC data levels or tiers were defined in terms of a specific combination of processing level (raw, normalized, or integrated) and access level (controlled or open access). In the case of tissue images, these standards are only now being established, but de-identification is not considered a risk and only the extent of processing is considered in establishing a data level. As of April 2021, the Minimal Information and Tissue Imaging standard (MITI) is still in an "request for comment" period, but we expect the final data levels for multiplexed tissue images generated using antibody reagents to be close to what is described below.

Level 1 data comprise the raw numerical output of acquisition instruments (microscope, slide scanner, etc.). These data may be in a variety of vendor-specific formats, although all microscope vendors and

investigators are strongly encouraged to conform to universally recognized Bioformats standards. For a whole slide image, Level 1 will contain many individual image tiles (images recorded from different x, y positions in the specimen). FASTQ files are a common type of Level 1 data in genomics.

Level 2 data comprise full-resolution primary images in the universal OME-TIFF format that have undergone stitching, registration, illumination correction, background subtraction, intensity normalization, etc. to generate high-quality mosaic images. The processing of Level 1 data to generate Level 2 data must be performed using automated software routines (no human intervention), ideally open source, whose operation is transparent. The generation of an image mosaic from multiple image tiles using ASHLAR is a prototypical Level 1 to Level 2 transformation. BAM files are a common type of Level 2 data in genomics.

Level 3 data are the results of image processing and include segmentation masks, labeling by humans, or by software algorithms. The generation of Level 3 data may involve human interpretation, which should be recorded as part of the image metadata. mRNA expression levels are a common type of Level 3 genomic data. For tissue imaging, level 3 data types include:

- Level 3 Image mosaics that have been subjected to quality control, typically to remove uninformative or inaccurate channels (e.g., ones in which an antibody provides no useful data), and for cyclic methods, channels in which tissue damage has reached unacceptable levels.
- Segmentation masks, which are typically generated using software but subjected to some level of human oversight or, in the case of machine learning, to supervised training. The models used to generate masks should be recorded.
- MINERVA “Data Overviews” that present Level 2 and Level 3 images with as little additional interpretation as possible, and are designed to enable informed inspection of primary image data without the need for download.

Level 4 data are numerical data generated from processing Level 2 and 3 data, most commonly to create “spatial feature tables” describing marker intensities, cell coordinates, and other single-cell features (the analogy is with count tables in RNA sequencing).

Level 5 data are results (e.g., cell type annotation) derived from Levels 2-4 spatial feature tables, images. Typical level 5 data include:

- MINERVA "Data Explorations" that use digital docents and human-generated annotation to guide users through the features of a complex set of images. The analogy is with a traditional figure.
- Dimensionality-reduced version of Level 4 data including PCA models
- Learned models (other than segmentation models) from images or other numerical data
- Models that integrated image data with other data modalities

Supplementary Material

Supplementary Table 1. Patient characteristics.

Supplementary Table 2. Clinical data related to the analyzed specimens.

Supplementary Table 3. Distribution of Regions of Interest (ROI) by histopathological annotation and patient ID.

Supplementary Table 4. Distribution of the clinical samples MEL1-MEL13 used in each CyCIF experiment (experiments 1 to 5) and the corresponding antibody panels.

Supplementary Table 5. The criteria for identifying individual cell phenotypes in CyCIF experiments 1 and 2 (antibody panels presented in Table S4).

Supplementary Table 6. Gene and protein symbols and names and the differentially expressed genes between MIS and EM-IM or between EM and IM regions.

Supplementary Video 1. A synapse between a PDL1+ macrophage and a PD1+ CD8+ T cell.

Supplementary Minerva story 1. HTA MEL Atlas 1: Introduction to the MEL Atlas (https://labsyspharm.github.io/HTA-MELATLAS-1/stories/MEL1-abstract.html)

Supplementary Minerva story 2. HTA MEL Atlas 1: Deep Exploration of a Primary Melanoma (https://labsyspharm.github.io/HTA-MELATLAS-1/stories/MEL1-full-story.html)

References

Anderson, A.C., Joller, N., and Kuchroo, V.K. (2016). Lag-3, Tim-3, and TIGIT co-inhibitory receptors with specialized functions in immune regulation. Immunity *44*, 989–1004.

Aung, P.P., Nagarajan, P., and Prieto, V.G. (2017). Regression in primary cutaneous melanoma: etiopathogenesis and clinical significance. Lab. Invest. *97*, 657–668.

Baharlou, H., Canete, N.P., Cunningham, A.L., Harman, A.N., and Patrick, E. (2019). Mass Cytometry Imaging for the Study of Human Diseases—Applications and Data Analysis Strategies. Front. Immunol. *10*.

Bai, X., Fisher, D.E., and Flaherty, K.T. (2019a). Cell-state dynamics and therapeutic resistance in melanoma from the perspective of MITF and IFNγ pathways. Nat. Rev. Clin. Oncol. *16*, 549–562.

Bai, X., Fisher, D.E., and Flaherty, K.T. (2019b). Cell-state dynamics and therapeutic resistance in melanoma from the perspective of MITF and IFNγ pathways. Nat. Rev. Clin. Oncol. *16*, 549–562.

Baker, G.J., Muhlich, J.L., Palaniappan, S.K., Moore, J.K., Davis, S.H., Santagata, S., and Sorger, P.K. (2020). SYLARAS: A Platform for the Statistical Analysis and Visual Display of Systemic Immunoprofiling Data and Its Application to Glioblastoma. Cell Syst. *11*, 272-285.e9.

Balogh, K.N., Templeton, D.J., and Cross, J.V. (2018). Macrophage Migration Inhibitory Factor protects cancer cells from immunogenic cell death and impairs anti-tumor immune responses. PloS One *13*, e0197702.

Bauer, T., Zagórska, A., Jurkin, J., Yasmin, N., Köffel, R., Richter, S., Gesslbauer, B., Lemke, G., and Strobl, H. (2012). Identification of Axl as a downstream effector of TGF-β1 during Langerhans cell differentiation and epidermal homeostasis. J. Exp. Med. *209*, 2033–2047.

Bergman, W., van Voorst Vader, P.C., and Ruiter, D.J. (1997). [Dysplastic nevi and the risk of melanoma: a guideline for patient care. Nederlandse Melanoom Werkgroep van de Vereniging voor Integrale Kankercentra]. Ned. Tijdschr. Geneeskd. *141*, 2010–2014.

Blei, D.M., Ng, A.Y., and Jordan, M.I. (2003). Latent dirichlet allocation. J. Mach. Learn. Res. *3*, 993–1022.

Bosisio, F.M., Antoranz, A., van Herck, Y., Bolognesi, M.M., Marcelis, L., Chinello, C., Wouters, J., Magni, F., Alexopoulos, L., Stas, M., et al. (2020). Functional heterogeneity of lymphocytic patterns in primary melanoma dissected through single-cell multiplexing. ELife *9*.

Bray, M.A., Singh, S., Han, H., Davis, C.T., Borgeson, B., Hartland, C., Kost-Alimova, M., Gustafsdottir, S.M., Gibson, C.C., and Carpenter, A.E. (2016). Cell Painting, a high-content image-based assay for morphological profiling using multiplexed fluorescent dyes. Nat Protoc *11*, 1757–1774.

Brody, J.R., Costantino, C.L., Berger, A.C., Sato, T., Lisanti, M.P., Yeo, C.J., Emmons, R.V., and Witkiewicz, A.K. (2009). Expression of indoleamine 2,3-dioxygenase in metastatic malignant

melanoma recruits regulatory T cells to avoid immune detection and affects survival. Cell Cycle Georget. Tex *8*, 1930–1934.

Calvo, V., and Izquierdo, M. (2018). Imaging Polarized Secretory Traffic at the Immune Synapse in Living T Lymphocytes. Front. Immunol. *9*.

Cichorek, M., Wachulska, M., Stasiewicz, A., and Tymińska, A. (2013). Skin melanocytes: biology and development. Postepy Dermatol. Alergol. *30*, 30–41.

Cirenajwis, H., Lauss, M., Ekedahl, H., Törngren, T., Kvist, A., Saal, L.H., Olsson, H., Staaf, J., Carneiro, A., Ingvar, C., et al. (2017). NF1□mutated melanoma tumors harbor distinct clinical and biological characteristics. Mol. Oncol. *11*, 438–451.

Clark, W.H., Elder, D.E., Guerry, D., Braitman, L.E., Trock, B.J., Schultz, D., Synnestvedt, M., and Halpern, A.C. (1989). Model predicting survival in stage I melanoma based on tumor progression. J. Natl. Cancer Inst. *81*, 1893–1904.

Damsky, W.E., and Bosenberg, M. (2017). Melanocytic nevi and melanoma: unraveling a complex relationship. Oncogene *36*, 5771–5792.

Demirkan, G., Hood, T., Reeves, J., Norgaard, Z., Hoang, M., Warren, S., Piazza, E., Boykin, R., and Beechem, J. (2020). Enabling pathway analysis of RNA expression in formalin-fixed paraffin embedded tissues with the GeoMx DSP Platform. J. Biomol. Tech. JBT *31*, S18.

Du, J., Widlund, H.R., Horstmann, M.A., Ramaswamy, S., Ross, K., Huber, W.E., Nishimura, E.K., Golub, T.R., and Fisher, D.E. (2004). Critical role of CDK2 for melanoma growth linked to its melanocyte-specific transcriptional regulation by MITF. Cancer Cell *6*, 565–576.

Elder, D.E. (2006). Precursors to melanoma and their mimics: nevi of special sites. Mod. Pathol. Off. J. U. S. Can. Acad. Pathol. Inc *19 Suppl 2*, S4-20.

Fan, J., Slowikowski, K., and Zhang, F. (2020). Single-cell transcriptomics in cancer: computational challenges and opportunities. Exp. Mol. Med. *52*, 1452–1465.

Fattore, L., Ruggiero, C.F., Liguoro, D., Mancini, R., and Ciliberto, G. (2019). Single cell analysis to dissect molecular heterogeneity and disease evolution in metastatic melanoma. Cell Death Dis. *10*, 1–12.

Fei, F., Qu, J., Zhang, M., Li, Y., and Zhang, S. (2017). S100A4 in cancer progression and metastasis: A systematic review. Oncotarget *8*, 73219–73239.

Fu, Q., Chen, N., Ge, C., Li, R., Li, Z., Zeng, B., Li, C., Wang, Y., Xue, Y., Song, X., et al. (2019). Prognostic value of tumor-infiltrating lymphocytes in melanoma: a systematic review and meta-analysis. Oncoimmunology *8*.

Gaglia, G., Kabraji, S., Argyropoulou, D., Dai, Y., Wang, S., Bergholz, J., Coy, S., Lin, J.-R., Jeselsohn, R., Metzger, O., et al. (2021). Temporal and spatial topography of cell proliferation in cancer. BioRxiv 2021.05.16.443704.

Garraway, L.A., Widlund, H.R., Rubin, M.A., Getz, G., Berger, A.J., Ramaswamy, S., Beroukhim, R., Milner, D.A., Granter, S.R., Du, J., et al. (2005). Integrative genomic analyses identify MITF as a lineage survival oncogene amplified in malignant melanoma. Nature *436*, 117–122.

Goding, C.R., and Arnheiter, H. (2019). MITF-the first 25 years. Genes Dev. *33*, 983–1007.

Gookin, S., Min, M., Phadke, H., Chung, M., Moser, J., Miller, I., Carter, D., and Spencer, S.L. (2017). A map of protein dynamics during cell-cycle progression and cell-cycle exit. PLoS Biol. *15*.

Guerry, D., Synnestvedt, M., Elder, D.E., and Schultz, D. (1993). Lessons from tumor progression: the invasive radial growth phase of melanoma is common, incapable of metastasis, and indolent. J. Invest. Dermatol. *100*, 342S-345S.

Guimera, R.V. (2011). bcbio-nextgen: Automated, distributed next-gen sequencing pipeline. EMBnet.Journal *17*, 30.

Guitart, J., Lowe, L., Piepkorn, M., Prieto, V.G., Rabkin, M.S., Ronan, S.G., Shea, C.R., Tron, V.A., White, W., and Barnhill, R.L. (2002). Histological characteristics of metastasizing thin melanomas: a case-control study of 43 cases. Arch. Dermatol. *138*, 603–608.

Hannier, S., Tournier, M., Bismuth, G., and Triebel, F. (1998). CD3/TCR complex-associated lymphocyte activation gene-3 molecules inhibit CD3/TCR signaling. J. Immunol. Baltim. Md 1950 *161*, 4058–4065.

Haq, R., Yokoyama, S., Hawryluk, E.B., Jönsson, G.B., Frederick, D.T., McHenry, K., Porter, D., Tran, T.-N., Love, K.T., Langer, R., et al. (2013). BCL2A1 is a lineage-specific antiapoptotic melanoma oncogene that confers resistance to BRAF inhibition. Proc. Natl. Acad. Sci. U. S. A. *110*, 4321–4326.

Hauschild, A., Engel, G., Brenner, W., Gläser, R., Mönig, H., Henze, E., and Christophers, E. (1999). S100B protein detection in serum is a significant prognostic factor in metastatic melanoma. Oncology *56*, 338–344.

Hemon, P., Jean-Louis, F., Ramgolam, K., Brignone, C., Viguier, M., Bachelez, H., Triebel, F., Charron, D., Aoudjit, F., Al-Daccak, R., et al. (2011). MHC class II engagement by its ligand LAG-3 (CD223) contributes to melanoma resistance to apoptosis. J. Immunol. Baltim. Md 1950 *186*, 5173–5183.

Higgins, H.W., Lee, K.C., Galan, A., and Leffell, D.J. (2015). Melanoma in situ: Part II. Histopathology, treatment, and clinical management. J. Am. Acad. Dermatol. *73*, 193–203; quiz 203–204.

Hikawa, R.S., Kanehisa, E.S., Enokihara, M.M.S. e S., Enokihara, M.Y., and Hirata, S.H. (2014). Polypoid melanoma and superficial spreading melanoma different subtypes in the same lesion. An. Bras. Dermatol. *89*, 666–668.

Hiraoka, Y., Swedlow, J.R., Paddy, M.R., Agard, D.A., and Sedat, J.W. (1991). Three-dimensional multiple-wavelength fluorescence microscopy for the structural analysis of biological phenomena. Semin. Cell Biol. *2*, 153–165.

Hodis, E., Watson, I.R., Kryukov, G.V., Arold, S.T., Imielinski, M., Theurillat, J.-P., Nickerson, E., Auclair, D., Li, L., Place, C., et al. (2012). A Landscape of Driver Mutations in Melanoma. Cell *150*, 251–263.

Hoffer, J., Rashid, R., Muhlich, J.L., Chen, Y.-A., Russell, D.P.W., Ruokonen, J., Krueger, R., Pfister, H., Santagata, S., and Sorger, P.K. (2020). Minerva: a light-weight, narrative image browser for multiplexed tissue images. J. Open Source Softw. *5*, 2579.

Holmgaard, R.B., Zamarin, D., Li, Y., Gasmi, B., Munn, D.H., Allison, J.P., Merghoub, T., and Wolchok, J.D. (2015). Tumor-Expressed IDO Recruits and Activates MDSCs in a Treg-Dependent Manner. Cell Rep. *13*, 412–424.

House, I.G., Savas, P., Lai, J., Chen, A.X.Y., Oliver, A.J., Teo, Z.L., Todd, K.L., Henderson, M.A., Giuffrida, L., Petley, E.V., et al. (2020). Macrophage-Derived CXCL9 and CXCL10 Are Required for Antitumor Immune Responses Following Immune Checkpoint Blockade. Clin. Cancer Res. *26*, 487–504.

Huard, B., Mastrangeli, R., Prigent, P., Bruniquel, D., Donini, S., El-Tayar, N., Maigret, B., Dréano, M., and Triebel, F. (1997). Characterization of the major histocompatibility complex class II binding site on LAG-3 protein. Proc. Natl. Acad. Sci. U. S. A. *94*, 5744–5749.

Jackson, H.W., Fischer, J.R., Zanotelli, V.R.T., Ali, H.R., Mechera, R., Soysal, S.D., Moch, H., Muenst, S., Varga, Z., Weber, W.P., et al. (2020). The single-cell pathology landscape of breast cancer. Nature *578*, 615–620.

Jané-Valbuena, J., Widlund, H.R., Perner, S., Johnson, L.A., Dibner, A.C., Lin, W.M., Baker, A.C., Nazarian, R.M., Vijayendran, K.G., Sellers, W.R., et al. (2010). An oncogenic role for ETV1 in melanoma. Cancer Res. *70*, 2075–2084.

Jorgovanovic, D., Song, M., Wang, L., and Zhang, Y. (2020). Roles of IFN-γ in tumor progression and regression: a review. Biomark. Res. *8*, 49.

Keung, E.Z., and Gershenwald, J.E. (2018). The eighth edition American Joint Committee on Cancer (AJCC) melanoma staging system: implications for melanoma treatment and care. Expert Rev. Anticancer Ther. *18*, 775–784.

Konieczkowski, D.J., Johannessen, C.M., Abudayyeh, O., Kim, J.W., Cooper, Z.A., Piris, A., Frederick, D.T., Barzily-Rokni, M., Straussman, R., Haq, R., et al. (2014). A melanoma cell state distinction influences sensitivity to MAPK pathway inhibitors. Cancer Discov. *4*, 816–827.

Larkin, J., Chiarion-Sileni, V., Gonzalez, R., Grob, J.J., Cowey, C.L., Lao, C.D., Schadendorf, D., Dummer, R., Smylie, M., Rutkowski, P., et al. (2015). Combined Nivolumab and Ipilimumab or Monotherapy in Untreated Melanoma. N. Engl. J. Med. *373*, 23–34.

Larkin, J., Chiarion-Sileni, V., Gonzalez, R., Grob, J.-J., Rutkowski, P., Lao, C.D., Cowey, C.L., Schadendorf, D., Wagstaff, J., Dummer, R., et al. (2019). Five-Year Survival with Combined Nivolumab and Ipilimumab in Advanced Melanoma. N. Engl. J. Med. *381*, 1535–1546.

Levy, C., Khaled, M., and Fisher, D.E. (2006). MITF: master regulator of melanocyte development and melanoma oncogene. Trends Mol. Med. *12*, 406–414.

Li, T., Forbes, M.E., Fuller, G.N., Li, J., Yang, X., and Zhang, W. (2020). IGFBP2: integrative hub of developmental and oncogenic signaling network. Oncogene *39*, 2243–2257.

Lian, C.G., and Murphy, G.F. (2016). The Genetic Evolution of Melanoma. N. Engl. J. Med. *374*, 994–995.

Lian, C.G., Xu, Y., Ceol, C., Wu, F., Larson, A., Dresser, K., Xu, W., Tan, L., Hu, Y., Zhan, Q., et al. (2012). Loss of 5-hydroxymethylcytosine is an epigenetic hallmark of melanoma. Cell *150*, 1135–1146.

Lin, J.-R., Izar, B., Wang, S., Yapp, C., Mei, S., Shah, P.M., Santagata, S., and Sorger, P.K. (2018). Highly multiplexed immunofluorescence imaging of human tissues and tumors using t-CyCIF and conventional optical microscopes. ELife *7*, e31657.

Lin, J.-R., Wang, S., Coy, S., Tyler, M.A., Yapp, C., Chen, Y.-A., Heiser, C.N., Lau, K., Santagata, S., and Sorger, P.K. (2021). Multiplexed 3D atlas of state transitions and immune interactions in colorectal cancer. BioRxiv 2021.03.31.437984.

Liu, Z., Dou, C., Jia, Y., Li, Q., Zheng, X., Yao, Y., Liu, Q., and Song, T. (2015). RIG-I suppresses the migration and invasion of hepatocellular carcinoma cells by regulating MMP9. Int. J. Oncol. *46*, 1710–1720.

Love, M.I., Huber, W., and Anders, S. (2014). Moderated estimation of fold change and dispersion for RNA-seq data with DESeq2. Genome Biol. *15*, 550.

Maibach, F., Sadozai, H., Seyed Jafari, S.M., Hunger, R.E., and Schenk, M. (2020). Tumor-Infiltrating Lymphocytes and Their Prognostic Value in Cutaneous Melanoma. Front. Immunol. *11*.

Maier, T., Güell, M., and Serrano, L. (2009). Correlation of mRNA and protein in complex biological samples. FEBS Lett. *583*, 3966–3973.

Maliga, Z., Nirmal, A.J., Ericson, N.G., Boswell, S.A., U'Ren, L., Podyminogin, R., Chow, J., Chen, Y.-A., Chen, A.A., Weinstock, D.M., et al. (2021). Micro-region transcriptomics of fixed human tissue using Pick-Seq.

Manci, E.A., Balch, C.M., Murad, T.M., and Soong, S.J. (1981). Polypoid melanoma, a virulent variant of the nodular growth pattern. Am. J. Clin. Pathol. *75*, 810–815.

Martincorena, I., Roshan, A., Gerstung, M., Ellis, P., Loo, P.V., McLaren, S., Wedge, D.C., Fullam, A., Alexandrov, L.B., Tubio, J.M., et al. (2015). High burden and pervasive positive selection of somatic mutations in normal human skin. Science *348*, 880–886.

Metzemaekers, M., Vanheule, V., Janssens, R., Struyf, S., and Proost, P. (2017). Overview of the Mechanisms that May Contribute to the Non-Redundant Activities of Interferon-Inducible CXC Chemokine Receptor 3 Ligands. Front. Immunol. *8*, 1970.

Mihm, M.C., and Mulé, J.J. (2015). Reflections on the Histopathology of Tumor-Infiltrating Lymphocytes in Melanoma and the Host Immune Response. Cancer Immunol. Res. *3*, 827–835.

Mojic, M., Takeda, K., and Hayakawa, Y. (2017). The Dark Side of IFN-γ: Its Role in Promoting Cancer Immunoevasion. Int. J. Mol. Sci. *19*.

Moreci, R.S., and Lechler, T. (2020). Epidermal structure and differentiation. Curr. Biol. CB *30*, R144–R149.

Moriarty, W.F., Kim, E., Gerber, S.A., Hammers, H., and Alani, R.M. (2016). Neuropilin-2 promotes melanoma growth and progression in vivo. Melanoma Res. *26*, 321–328.

Murtas, D., Maric, D., De Giorgi, V., Reinboth, J., Worschech, A., Fetsch, P., Filie, A., Ascierto, M.L., Bedognetti, D., Liu, Q., et al. (2013). IRF-1 responsiveness to IFN- γ predicts different cancer immune phenotypes. Br. J. Cancer *109*, 76–82.

Mus, L.M., Lambertz, I., Claeys, S., Kumps, C., Van Loocke, W., Van Neste, C., Umapathy, G., Vaapil, M., Bartenhagen, C., Laureys, G., et al. (2020). The ETS transcription factor ETV5 is a target of activated ALK in neuroblastoma contributing to increased tumour aggressiveness. Sci. Rep. *10*, 218.

Nirmal, A.J., Regan, T., Shih, B.B., Hume, D.A., Sims, A.H., and Freeman, T.C. (2018). Immune Cell Gene Signatures for Profiling the Microenvironment of Solid Tumors. Cancer Immunol. Res. *6*, 1388–1400.

Noe, J.T., and Mitchell, R.A. (2020). MIF-Dependent Control of Tumor Immunity. Front. Immunol. *11*, 609948.

O'Donnell, J.S., Teng, M.W.L., and Smyth, M.J. (2019). Cancer immunoediting and resistance to T cell-based immunotherapy. Nat. Rev. Clin. Oncol. *16*, 151–167.

Oh, S.A., Wu, D.-C., Cheung, J., Navarro, A., Xiong, H., Cubas, R., Totpal, K., Chiu, H., Wu, Y., Comps-Agrar, L., et al. (2020). PD-L1 expression by dendritic cells is a key regulator of T-cell immunity in cancer. Nat. Cancer *1*, 681–691.

Oudin, M.J., and Weaver, V.M. (2016). Physical and Chemical Gradients in the Tumor Microenvironment Regulate Tumor Cell Invasion, Migration, and Metastasis. Cold Spring Harb. Symp. Quant. Biol. *81*, 189–205.

Paluskievicz, C.M., Cao, X., Abdi, R., Zheng, P., Liu, Y., and Bromberg, J.S. (2019). T Regulatory Cells and Priming the Suppressive Tumor Microenvironment. Front. Immunol. *10*.

Peng, Q., Qiu, X., Zhang, Z., Zhang, S., Zhang, Y., Liang, Y., Guo, J., Peng, H., Chen, M., Fu, Y.-X., et al. (2020). PD-L1 on dendritic cells attenuates T cell activation and regulates response to immune checkpoint blockade. Nat. Commun. *11*, 4835.

Propper, D.J., Chao, D., Braybrooke, J.P., Bahl, P., Thavasu, P., Balkwill, F., Turley, H., Dobbs, N., Gatter, K., Talbot, D.C., et al. (2003). Low-dose IFN-gamma induces tumor MHC expression in metastatic malignant melanoma. Clin. Cancer Res. Off. J. Am. Assoc. Cancer Res. *9*, 84–92.

Qi, T.F., Guo, L., Huang, M., Li, L., Miao, W., and Wang, Y. (2020). Discovery of TBC1D7 as a Potential Driver for Melanoma Cell Invasion. Proteomics *20*, e1900347.

Rashid, R., Chen, Y.-A., Hoffer, J., Muhlich, J.L., Lin, J.-R., Krueger, R., Pfister, H., Mitchell, R., Santagata, S., and Sorger, P.K. (2020). Online narrative guides for illuminating tissue atlas data and digital pathology images. BioRxiv 2020.03.27.001834.

Rey, S.J. (2001). Mathematical Models in Geography. In International Encyclopedia of the Social & Behavioral Sciences, N.J. Smelser, and P.B. Baltes, eds. (Oxford: Pergamon), pp. 9393–9399.

Rogers, K.W., and Schier, A.F. (2011). Morphogen gradients: from generation to interpretation. Annu. Rev. Cell Dev. Biol. *27*, 377–407.

Schapiro, D., Sokolov, A., Yapp, C., Muhlich, J.L., Hess, J., Lin, J.-R., Chen, Y.-A., Nariya, M.K., Baker, G.J., Ruokonen, J., et al. (2021). MCMICRO: A scalable, modular image-processing pipeline for multiplexed tissue imaging. BioRxiv 2021.03.15.435473.

Shaffer, S.M., Dunagin, M.C., Torborg, S.R., Torre, E.A., Emert, B., Krepler, C., Beqiri, M., Sproesser, K., Brafford, P.A., Xiao, M., et al. (2017). Rare cell variability and drug-induced reprogramming as a mode of cancer drug resistance. Nature *546*, 431–435.

Shain, A.H., Yeh, I., Kovalyshyn, I., Sriharan, A., Talevich, E., Gagnon, A., Dummer, R., North, J., Pincus, L., Ruben, B., et al. (2015). The Genetic Evolution of Melanoma from Precursor Lesions. N. Engl. J. Med. *373*, 1926–1936.

Shih, B.B., Nirmal, A.J., Headon, D.J., Akbar, A.N., Mabbott, N.A., and Freeman, T.C. (2017). Derivation of marker gene signatures from human skin and their use in the interpretation of the transcriptional changes associated with dermatological disorders. J. Pathol. *241*, 600–613.

Smithy, J.W., Moore, L.M., Pelekanou, V., Rehman, J., Gaule, P., Wong, P.F., Neumeister, V.M., Sznol, M., Kluger, H.M., and Rimm, D.L. (2017). Nuclear IRF-1 expression as a mechanism to assess "Capability" to express PD-L1 and response to PD-1 therapy in metastatic melanoma. J. Immunother. Cancer *5*, 25.

Smoller, B.R. (2006). Histologic criteria for diagnosing primary cutaneous malignant melanoma. Mod. Pathol. Off. J. U. S. Can. Acad. Pathol. Inc *19 Suppl 2*, S34-40.

Spranger, S., Spaapen, R.M., Zha, Y., Williams, J., Meng, Y., Ha, T.T., and Gajewski, T.F. (2013). Up-Regulation of PD-L1, IDO, and Tregs in the Melanoma Tumor Microenvironment Is Driven by CD8+ T Cells. Sci. Transl. Med. *5*, 200ra116.

Stoltzfus, C.R., Filipek, J., Gern, B.H., Olin, B.E., Leal, J.M., Wu, Y., Lyons-Cohen, M.R., Huang, J.Y., Paz-Stoltzfus, C.L., Plumlee, C.R., et al. (2020). CytoMAP: A Spatial Analysis Toolbox Reveals Features of Myeloid Cell Organization in Lymphoid Tissues. Cell Rep. *31*, 107523.

Subramanian, A., Tamayo, P., Mootha, V.K., Mukherjee, S., Ebert, B.L., Gillette, M.A., Paulovich, A., Pomeroy, S.L., Golub, T.R., Lander, E.S., et al. (2005). Gene set enrichment analysis: a knowledge-based approach for interpreting genome-wide expression profiles. Proc. Natl. Acad. Sci. U. S. A. *102*, 15545–15550.

Sudhan, D.R., Pampo, C., Rice, L., and Siemann, D.W. (2016). Cathepsin L inactivation leads to multimodal inhibition of prostate cancer cell dissemination in a preclinical bone metastasis model. Int. J. Cancer *138*, 2665–2677.

Sui, H., Shi, C., Yan, Z., and Wu, M. (2016). Overexpression of Cathepsin L is associated with chemoresistance and invasion of epithelial ovarian cancer. Oncotarget *7*, 45995–46001.

Sun, X., Cheng, G., Hao, M., Zheng, J., Zhou, X., Zhang, J., Taichman, R.S., Pienta, K.J., and Wang, J. (2010). CXCL12/CXCR4/CXCR7 Chemokine Axis and Cancer Progression. Cancer Metastasis Rev. *29*, 709–722.

Swann, J.B., and Smyth, M.J. (2007). Immune surveillance of tumors. J. Clin. Invest. *117*, 1137–1146.

Swetter, S.M., Tsao, H., Bichakjian, C.K., Curiel-Lewandrowski, C., Elder, D.E., Gershenwald, J.E., Guild, V., Grant-Kels, J.M., Halpern, A.C., Johnson, T.M., et al. (2019). Guidelines of care for the management of primary cutaneous melanoma. J. Am. Acad. Dermatol. *80*, 208–250.

Tanese, K., Hashimoto, Y., Berkova, Z., Wang, Y., Samaniego, F., Lee, J.E., Ekmekcioglu, S., and Grimm, E.A. (2015). Cell Surface CD74-MIF Interactions Drive Melanoma Survival in Response to Interferon-γ. J. Invest. Dermatol. *135*, 2775–2784.

Theocharidis, A., van Dongen, S., Enright, A.J., and Freeman, T.C. (2009). Network visualization and analysis of gene expression data using BioLayout Express(3D). Nat. Protoc. *4*, 1535–1550.

Thomas, N.E., Busam, K.J., From, L., Kricker, A., Armstrong, B.K., Anton-Culver, H., Gruber, S.B., Gallagher, R.P., Zanetti, R., Rosso, S., et al. (2013). Tumor-infiltrating lymphocyte grade in primary melanomas is independently associated with melanoma-specific survival in the population-based genes, environment and melanoma study. J. Clin. Oncol. Off. J. Am. Soc. Clin. Oncol. *31*, 4252–4259.

Tirosh, I., Izar, B., Prakadan, S.M., Wadsworth, M.H., 2nd, Treacy, D., Trombetta, J.J., Rotem, A., Rodman, C., Lian, C., Murphy, G., et al. (2016). Dissecting the multicellular ecosystem of metastatic melanoma by single-cell RNA-seq. Science *352*, 189–196.

Valle, D., Baiser, B., Woodall, C.W., and Chazdon, R. (2014). Decomposing biodiversity data using the Latent Dirichlet Allocation model, a probabilistic multivariate statistical method. Ecol. Lett. *17*, 1591–1601.

Vivas-García, Y., Falletta, P., Liebing, J., Louphrasitthiphol, P., Feng, Y., Chauhan, J., Scott, D.A., Glodde, N., Chocarro-Calvo, A., Bonham, S., et al. (2020). Lineage-Restricted Regulation of SCD and Fatty Acid Saturation by MITF Controls Melanoma Phenotypic Plasticity. Mol. Cell *77*, 120-137.e9.

Wu, Q.W. (2016). Serpine2, a potential novel target for combating melanoma metastasis. Am. J. Transl. Res. *8*, 1985–1997.

Xiong, T., Pan, F., and Li, D. (2019). Expression and clinical significance of S100 family genes in patients with melanoma. Melanoma Res. *29*, 23–29.

Yapp, C., Novikov, E., Jang, W.-D., Chen, Y.-A., Cicconet, M., Maliga, Z., Jacobson, C.A., Wei, D., Santagata, S., Pfister, H., et al. (2021). UnMICST: Deep learning with real augmentation for robust segmentation of highly multiplexed images of human tissues. BioRxiv 2021.04.02.438285.

Zhai, L., Bell, A., Ladomersky, E., Lauing, K.L., Bollu, L., Sosman, J.A., Zhang, B., Wu, J.D., Miller, S.D., Meeks, J.J., et al. (2020). Immunosuppressive IDO in Cancer: Mechanisms of Action, Animal Models, and Targeting Strategies. Front. Immunol. *11*.

Zollinger, D.R., Lingle, S.E., Sorg, K., Beechem, J.M., and Merritt, C.R. (2020). GeoMx^{TM} RNA Assay: High Multiplex, Digital, Spatial Analysis of RNA in FFPE Tissue. Methods Mol. Biol. Clifton NJ *2148*, 331–345.

Figure 1

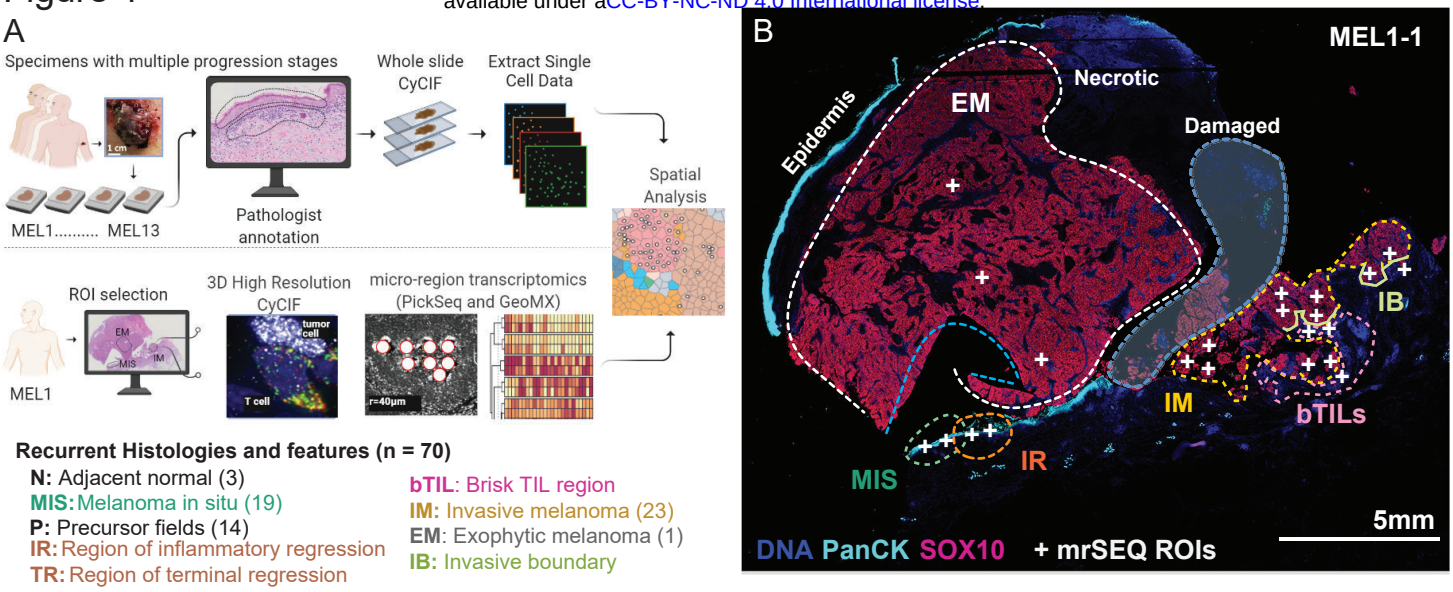

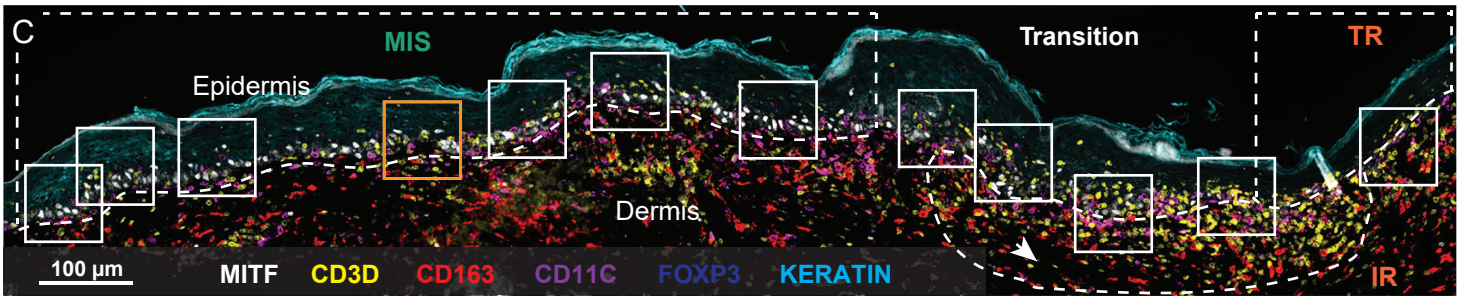

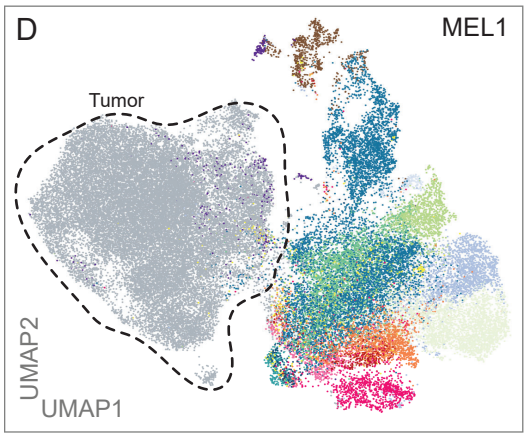

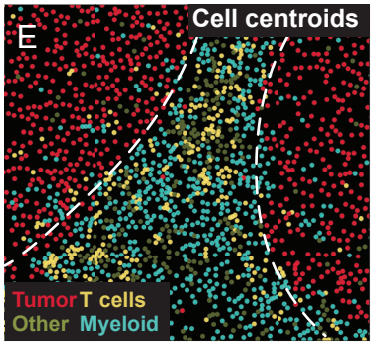

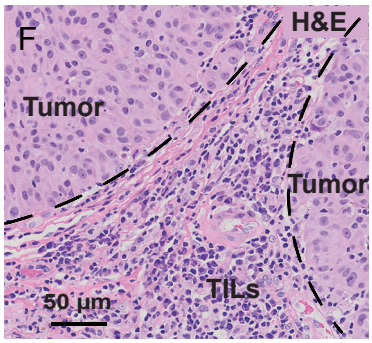

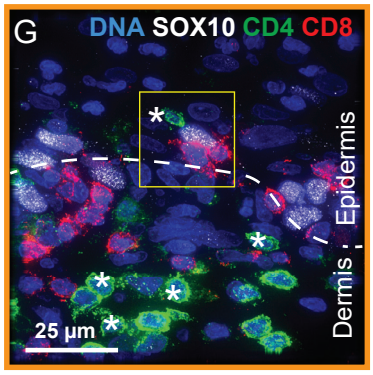

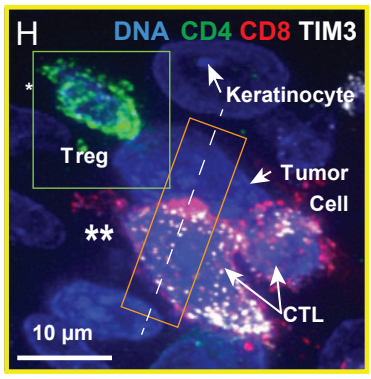

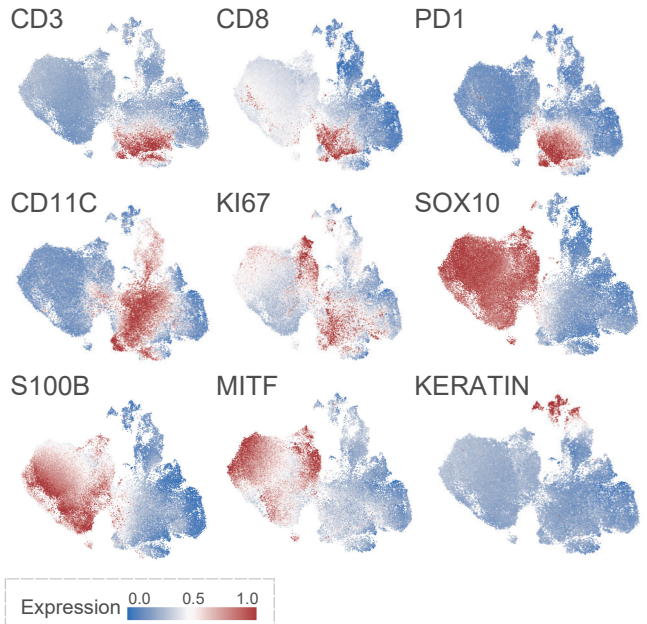

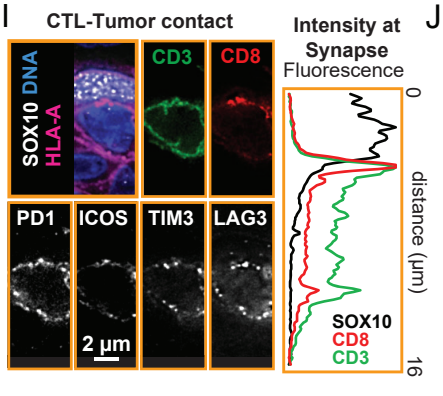

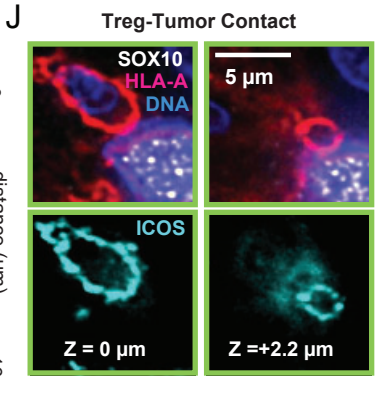

Figure S1

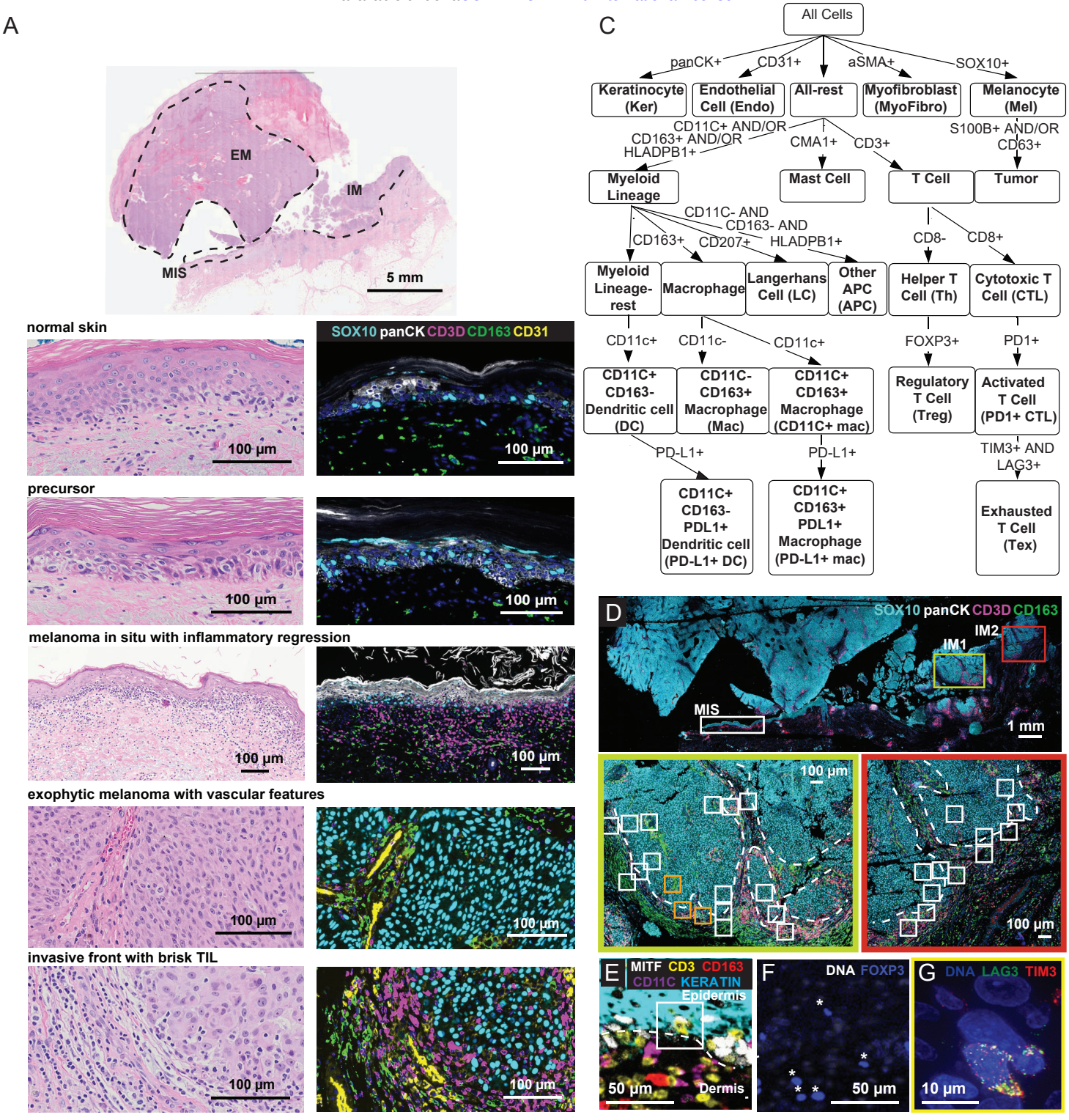

Figure 2

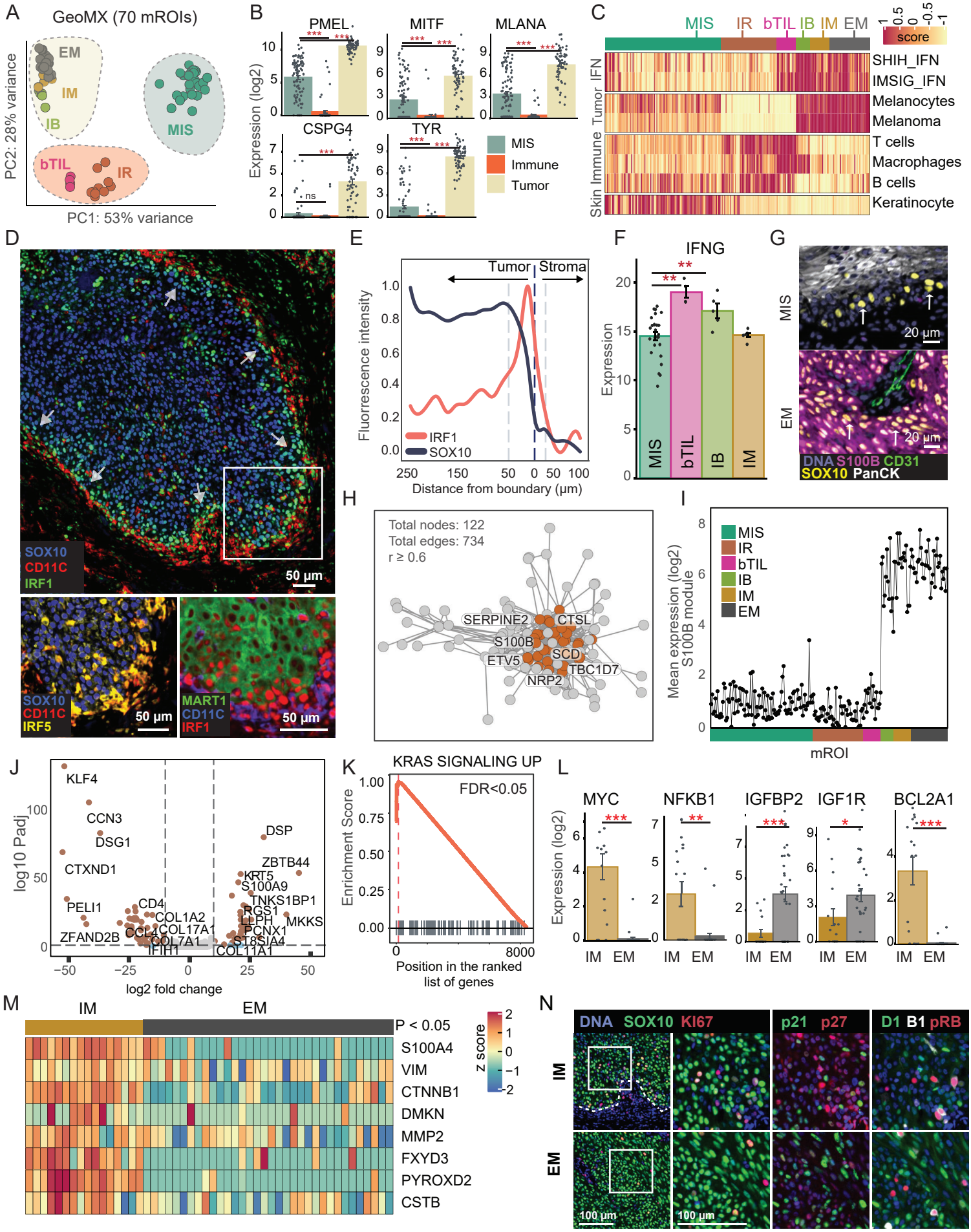

Figure S2

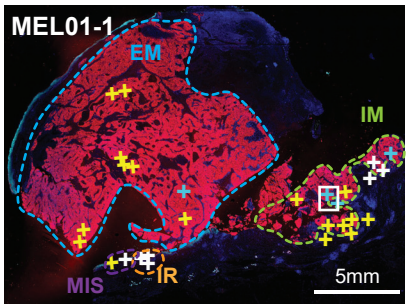

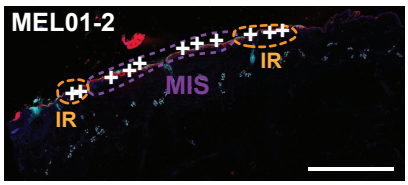

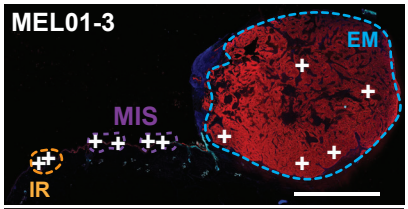

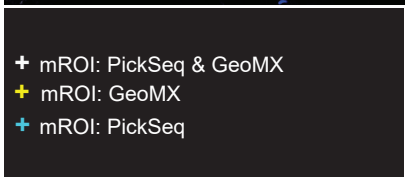

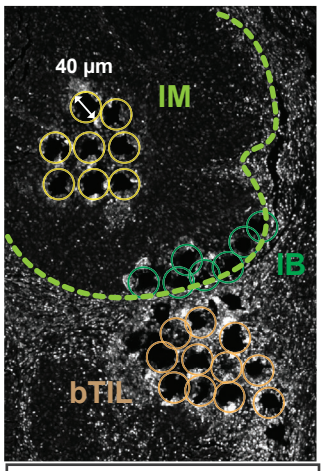

	PickSeq	GeoMX
MEL01-1		
MIS	12	4
IR	16	1
IM	16	6
IB	12	5
bTIL	16	4
EM	3	9
MEL01-2		
MIS	32	12
IR	21	8
EM	14	-
MEL01-3		
MIS	53	10
IR	10	1
EM	17	10

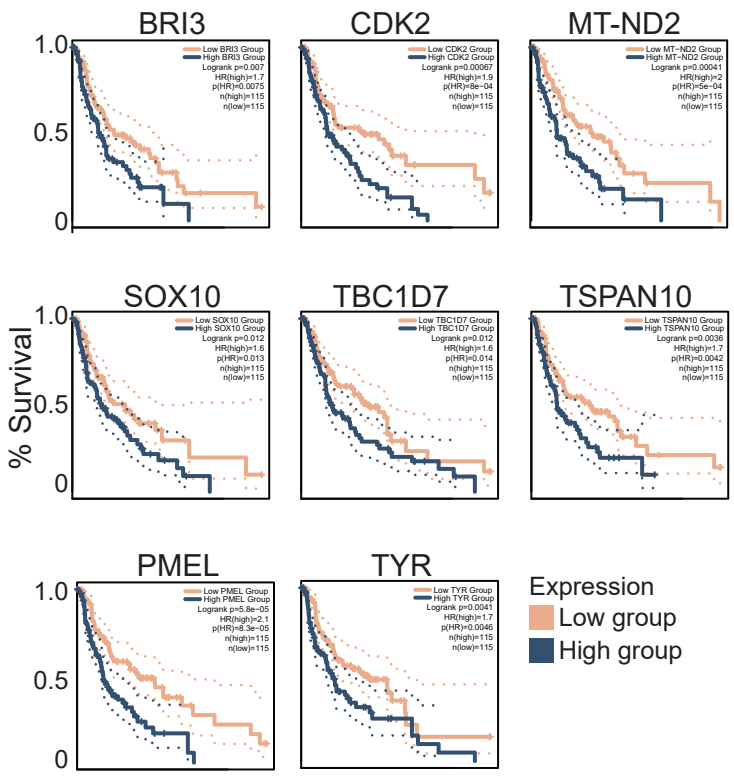

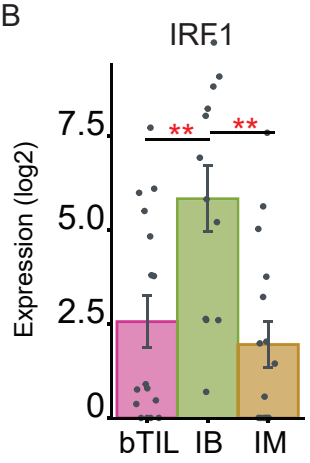

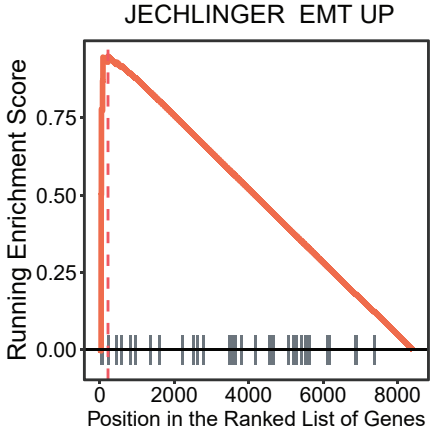

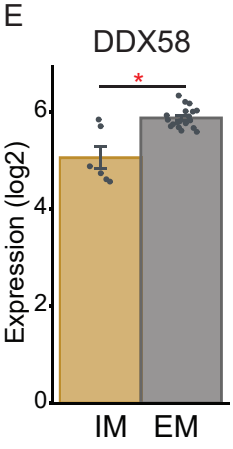

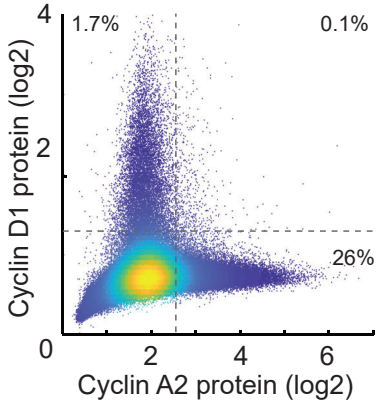

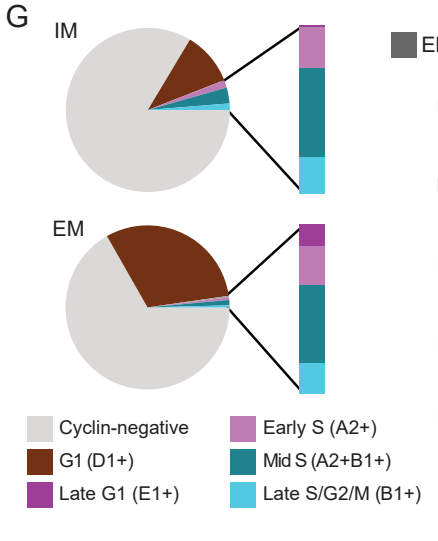

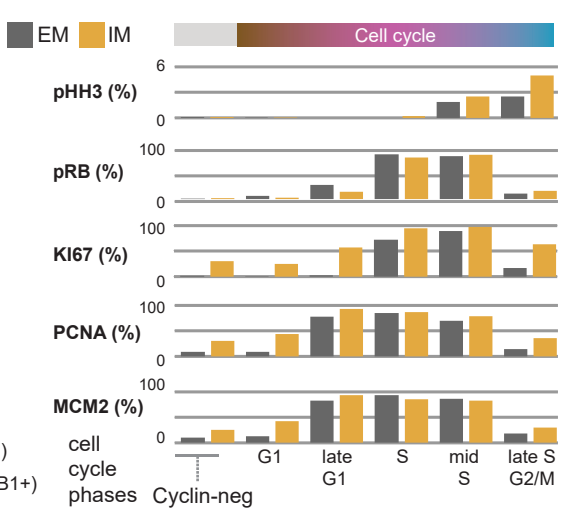

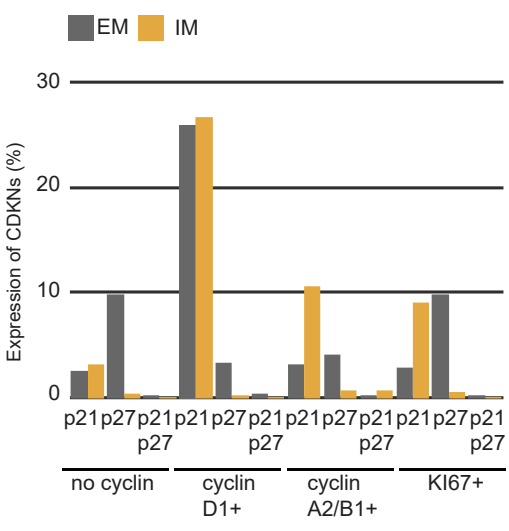

Figure 3

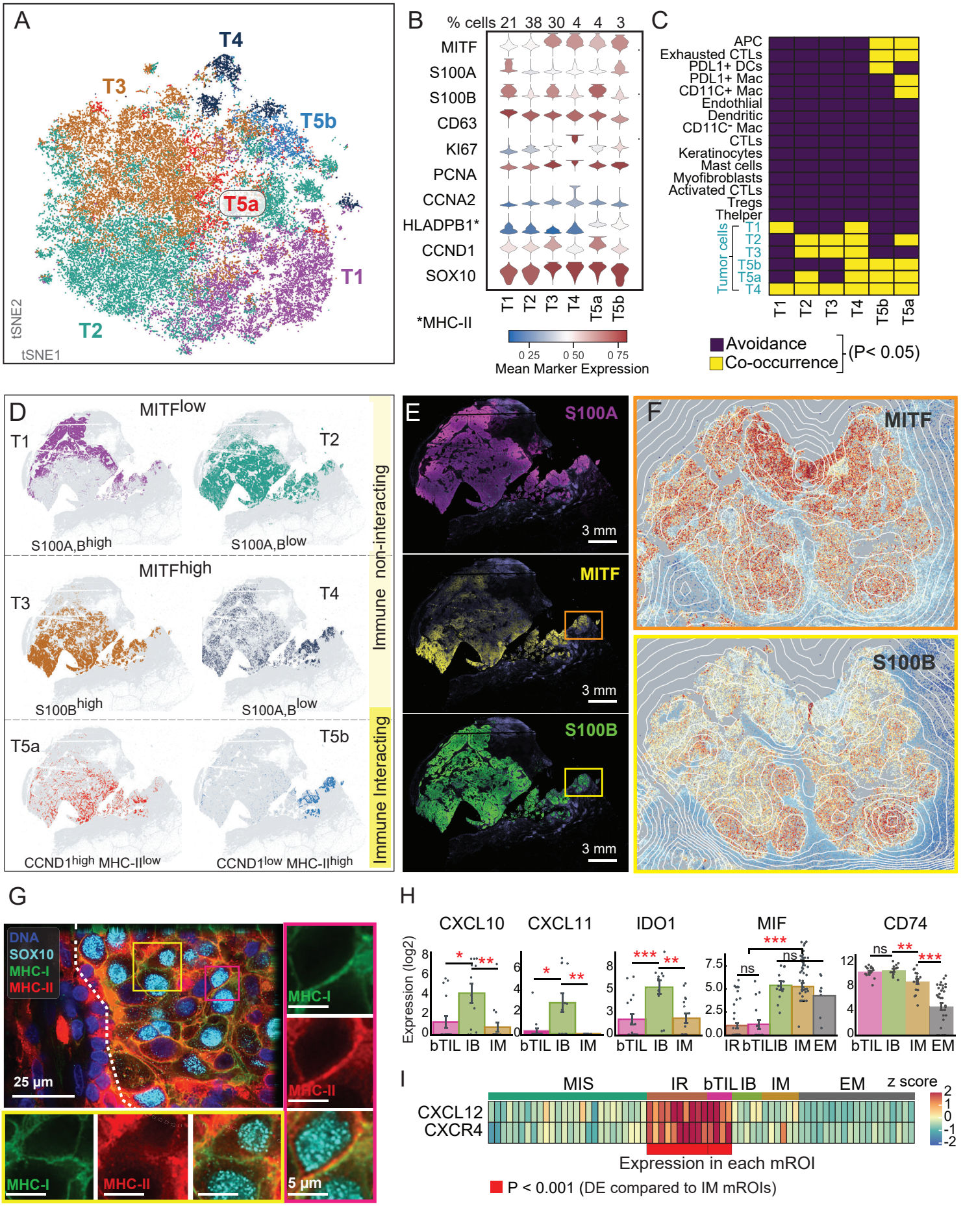

Figure S3

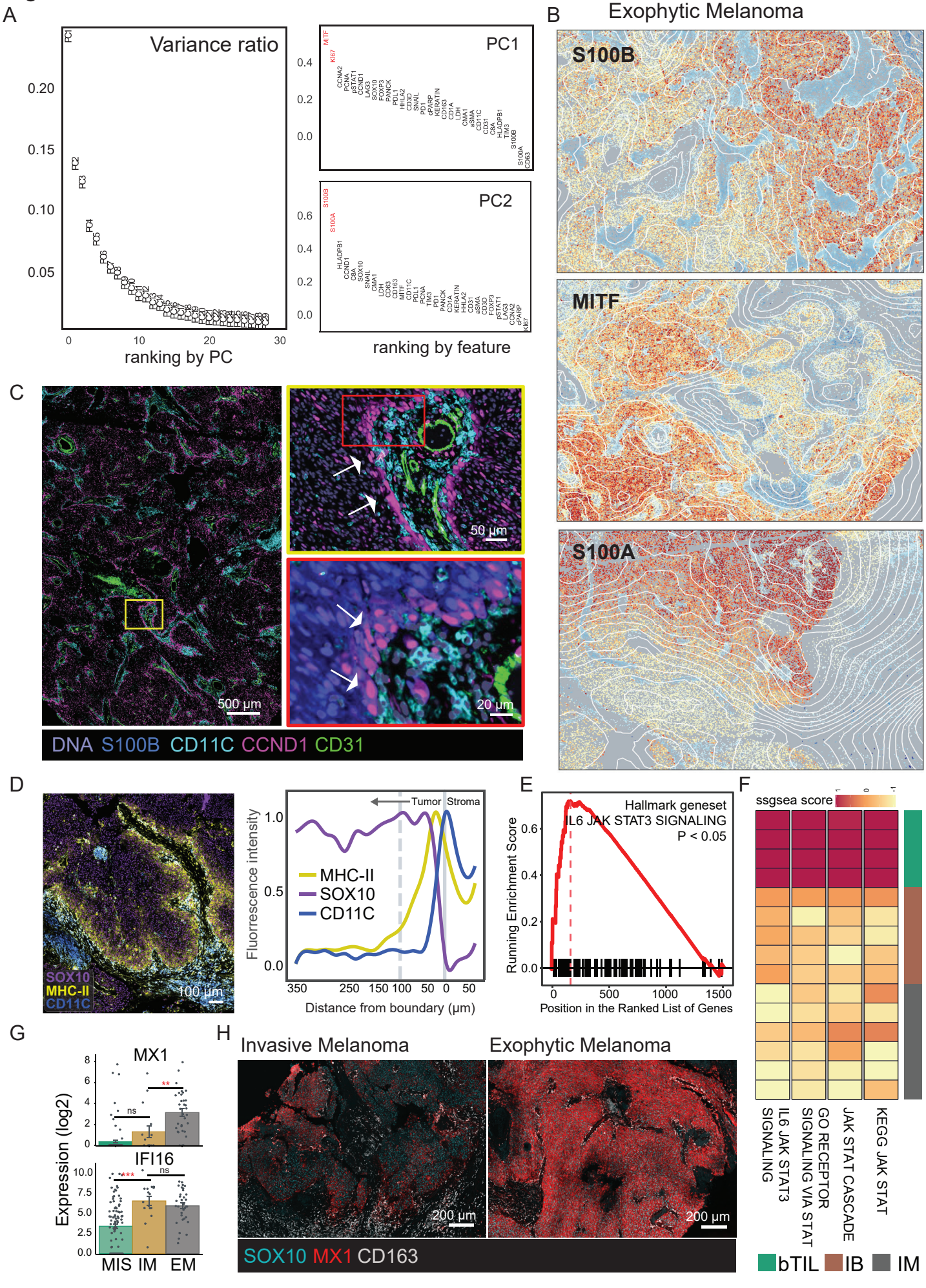

Figure 4

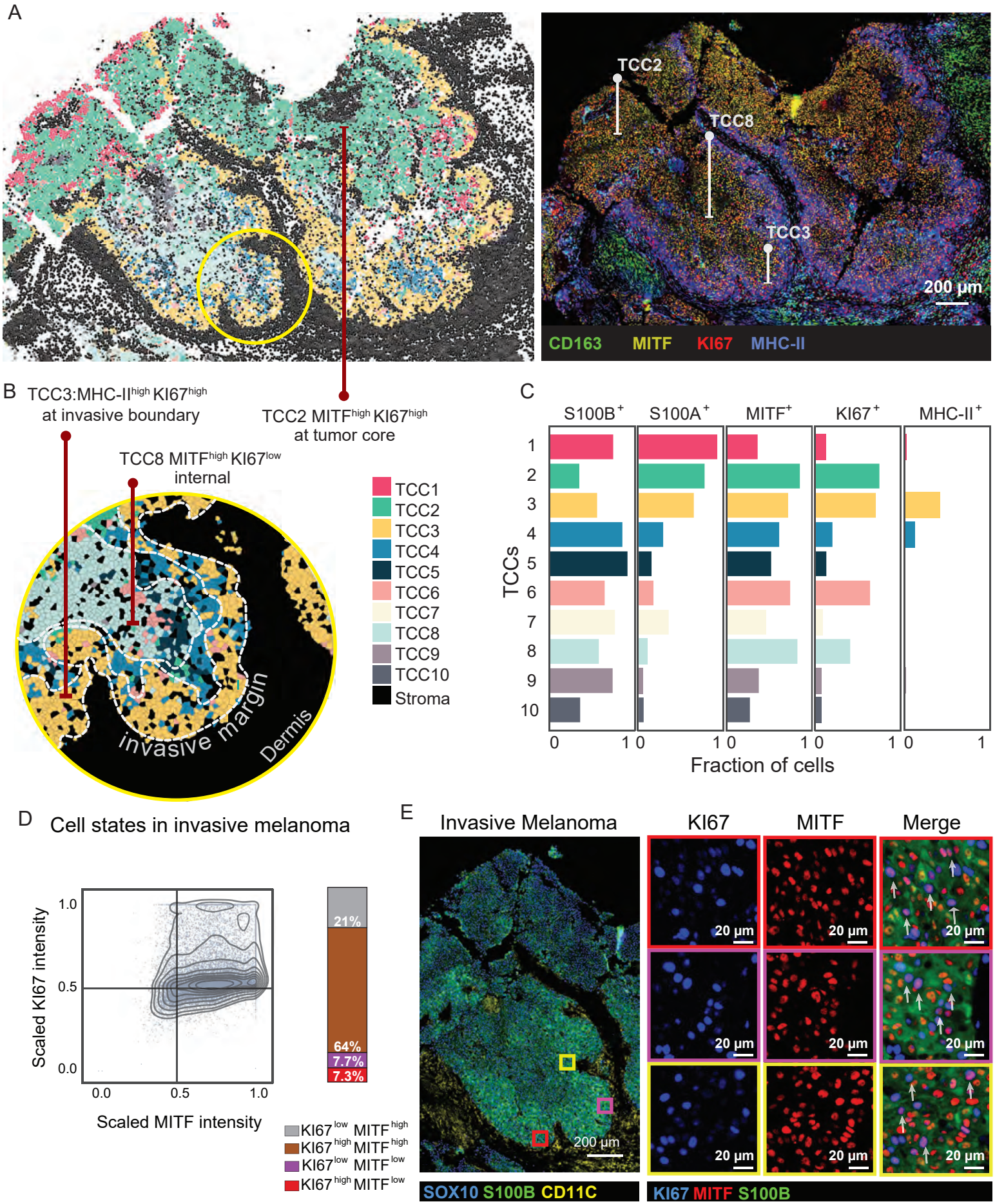

Figure S4

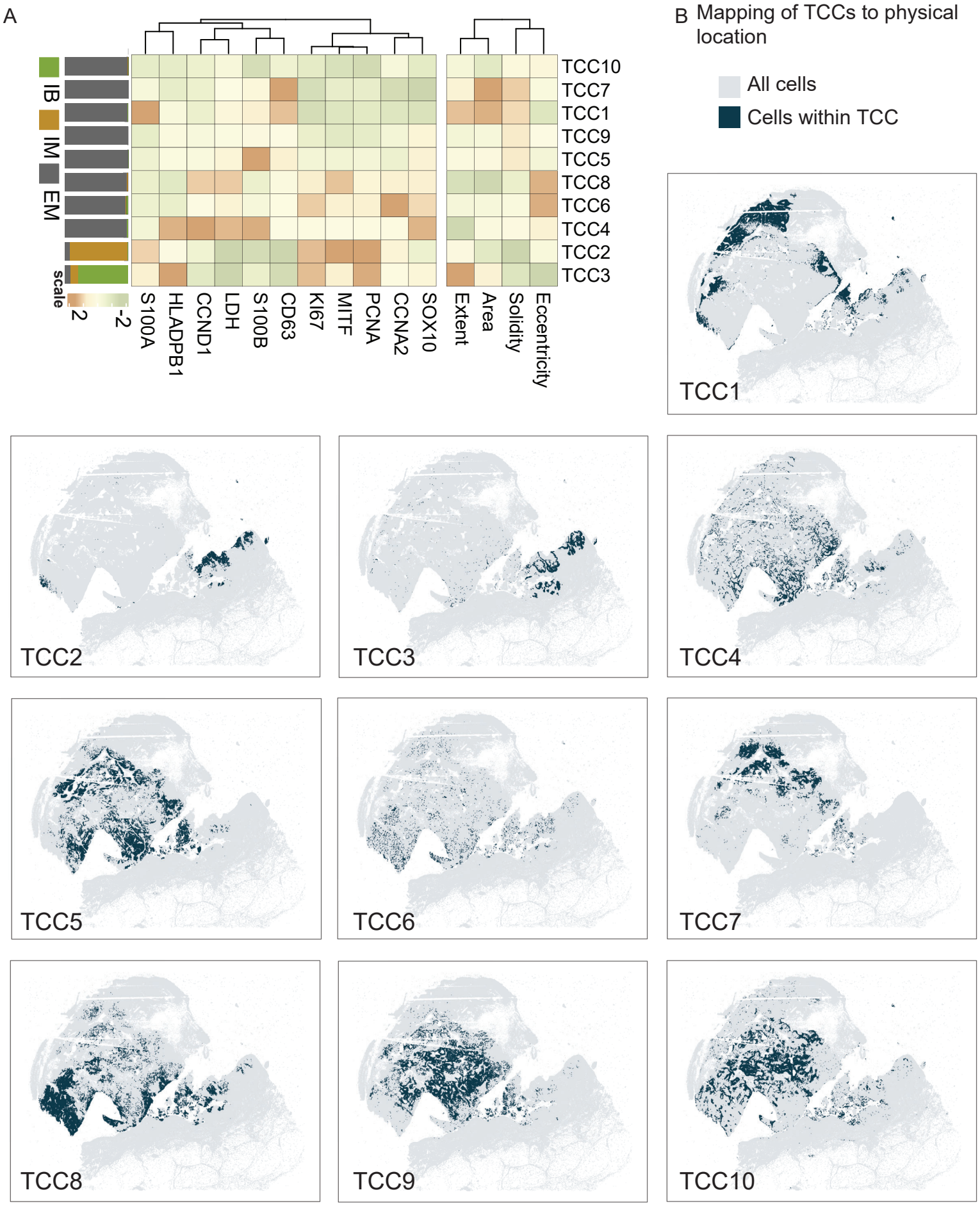

Figure 5

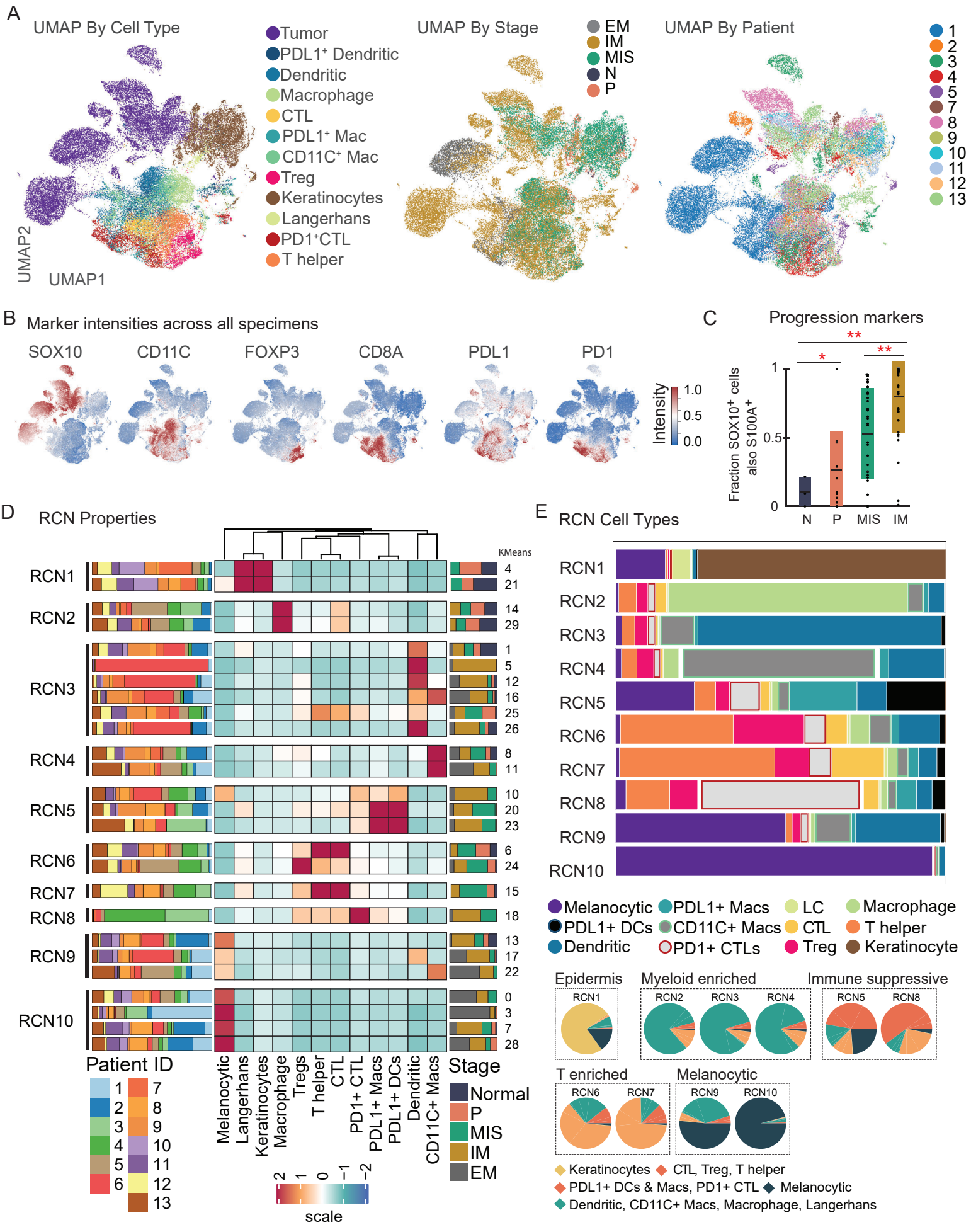

Figure S5

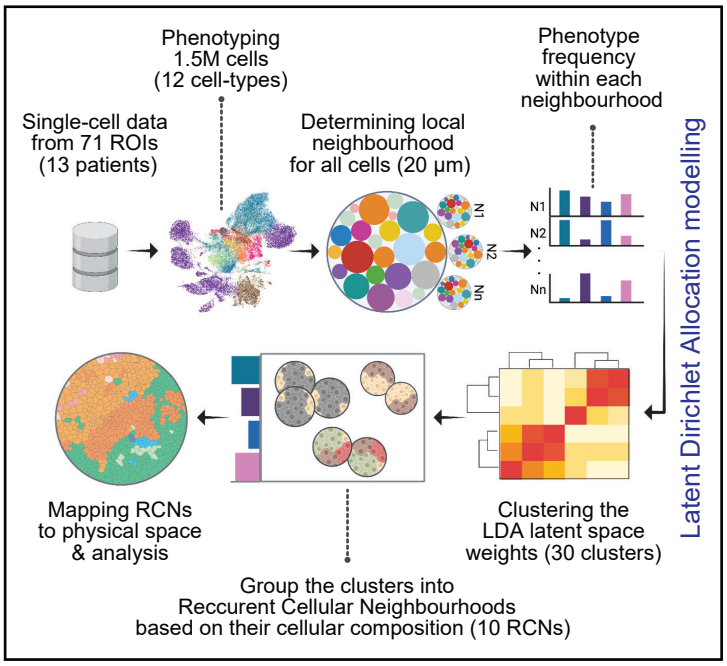

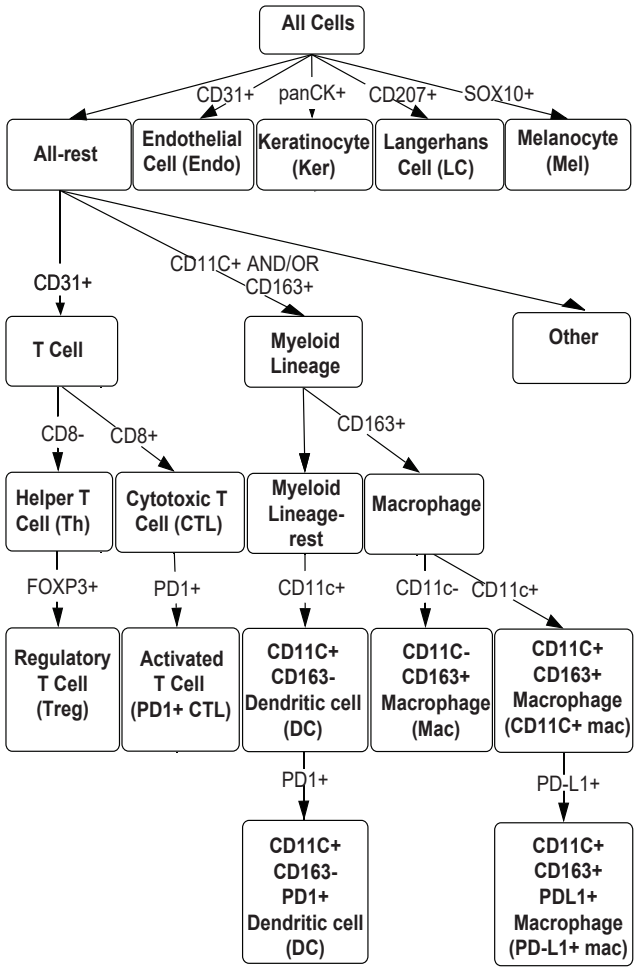

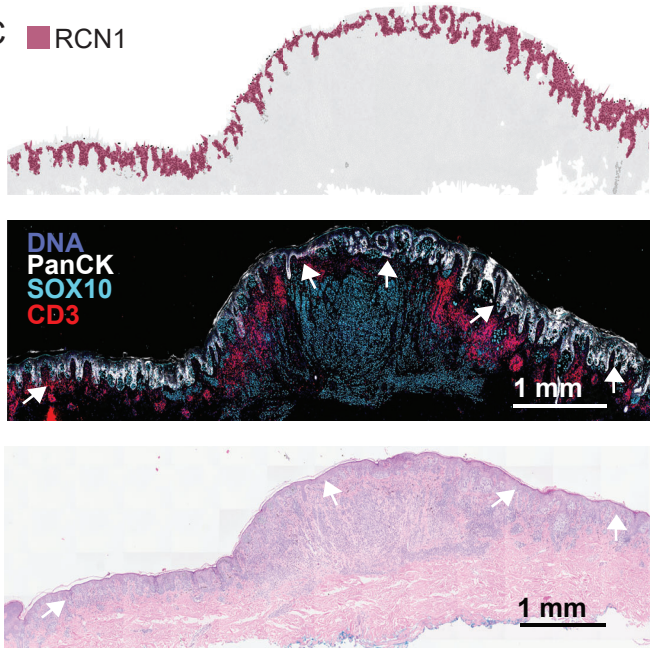

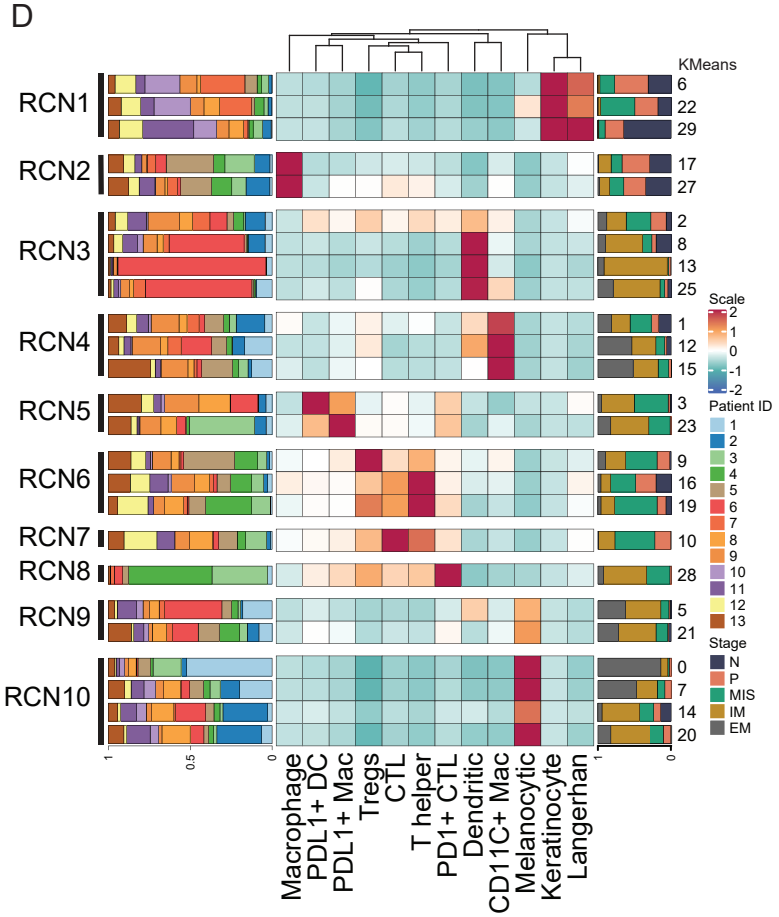

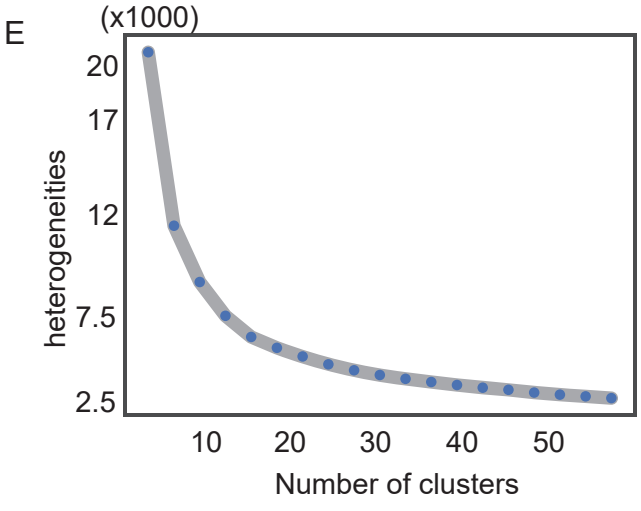

Figure 6

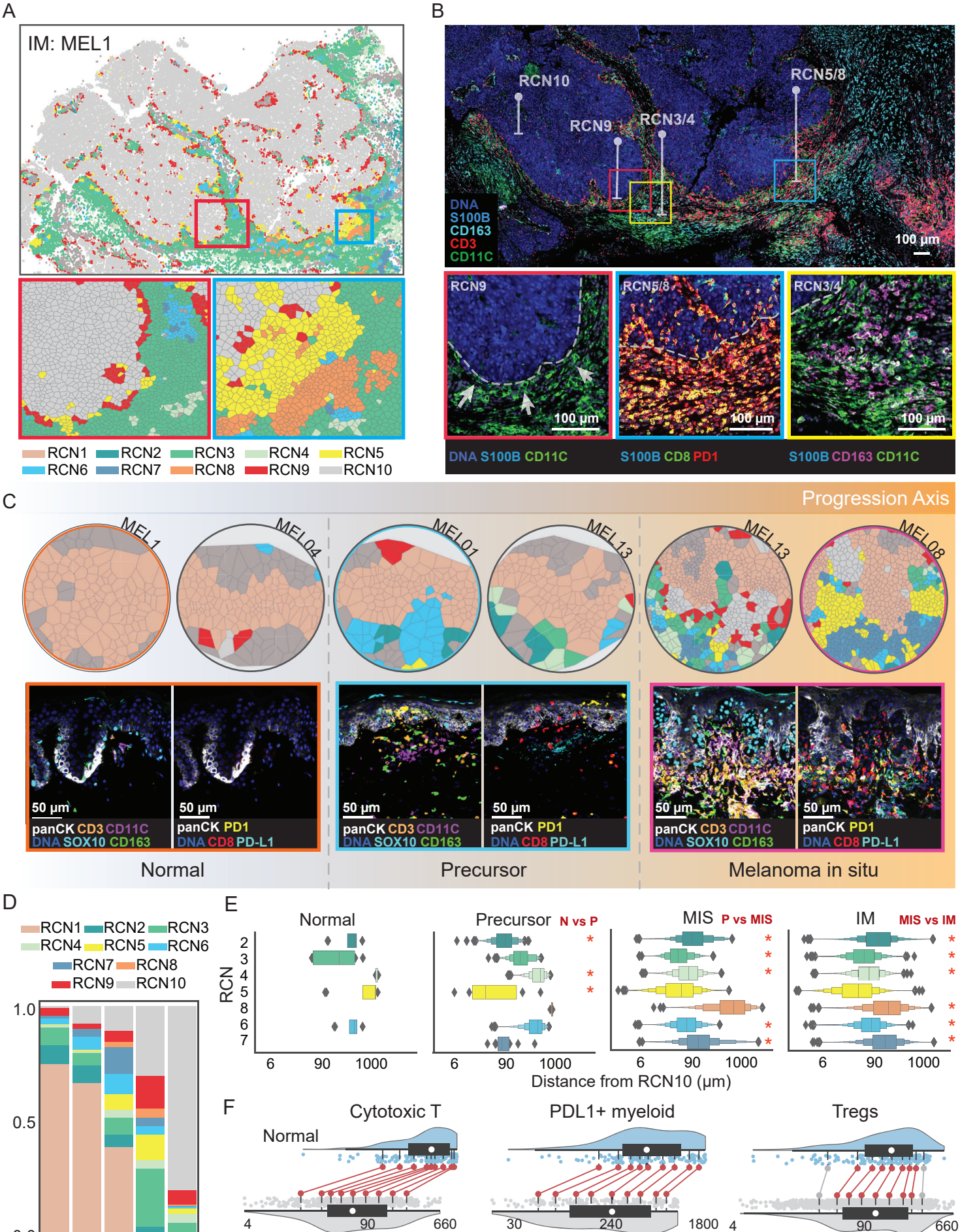

Figure S6

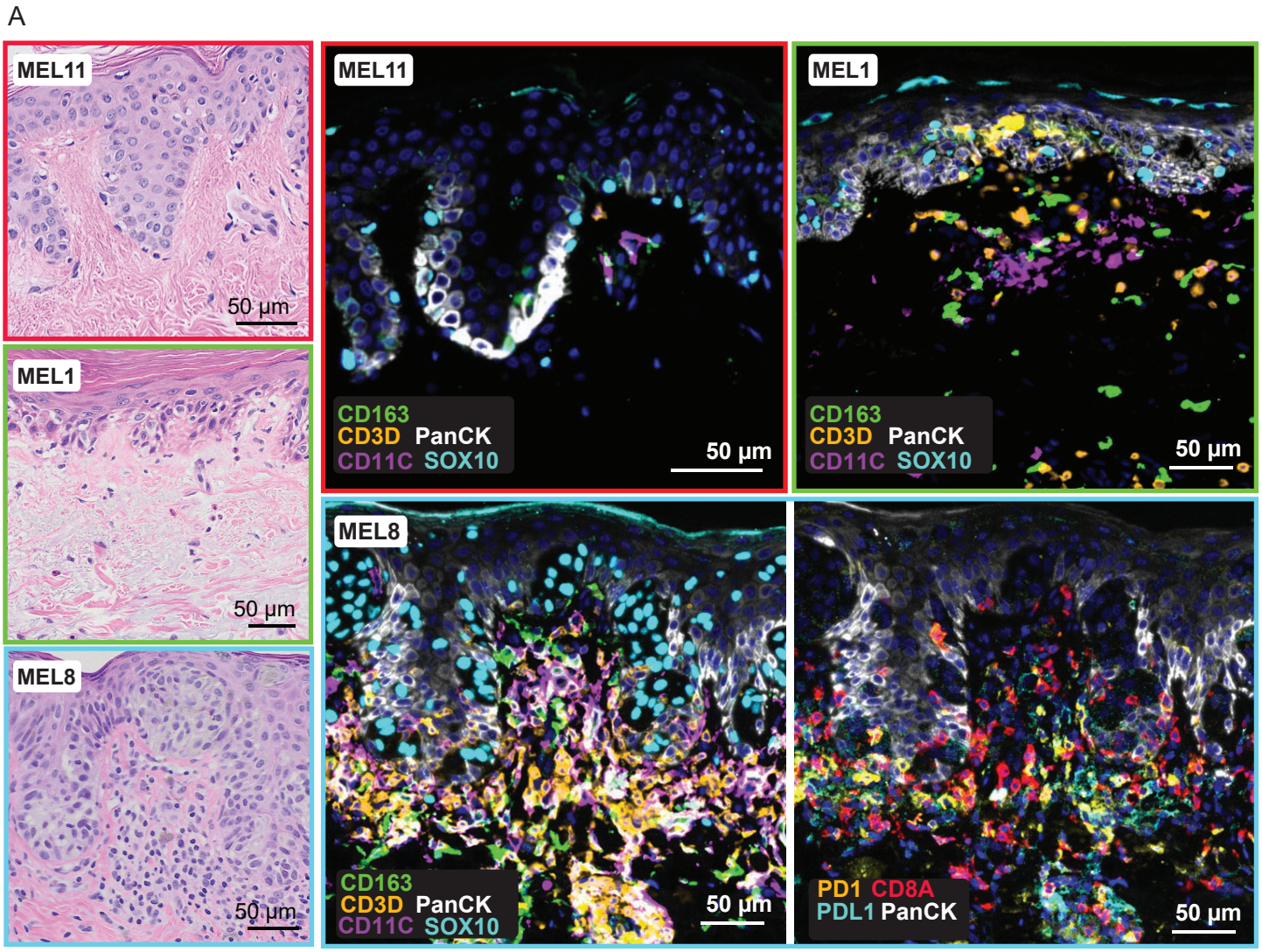

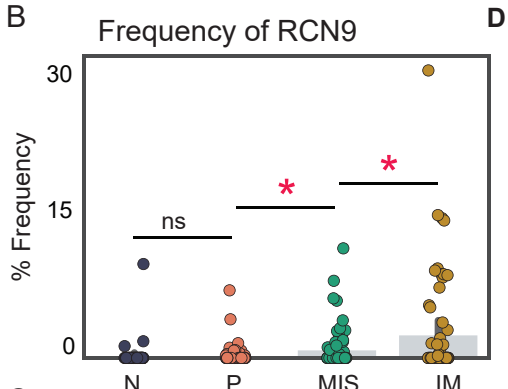

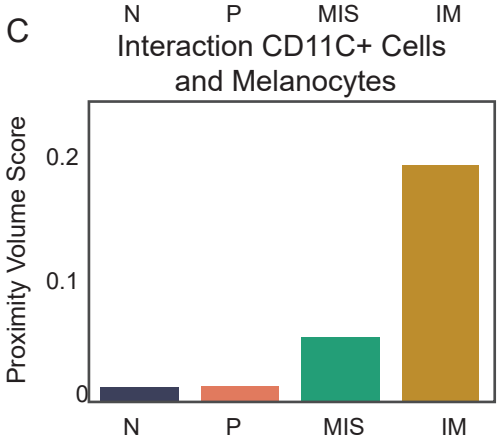

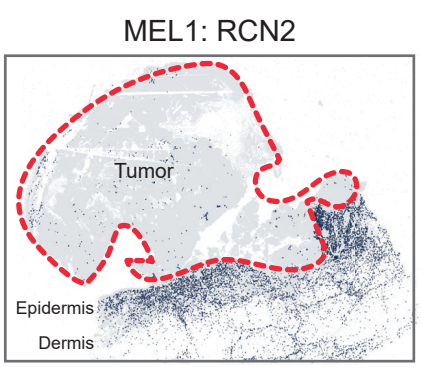

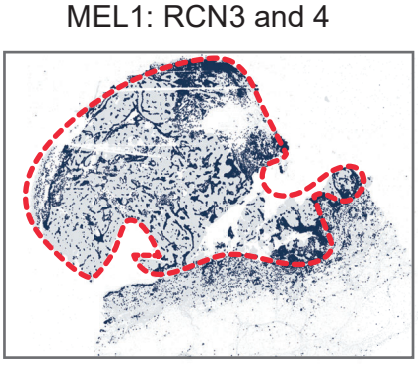

E Differences between stages

	N v P	P v MIS	P v IM	MIS v IM
RCN1	0.001	0.826	0.002	0.001
RCN2	0.057	0.072	0.004	0.232
RCN3	0.198	0.001	0.055	0.480
RCN4	0.020	0.001	0.000	0.160
RCN5	0.195	0.001	0.001	0.145
RCN6	0.061	0.002	0.001	0.752
RCN7	0.140	0.004	0.001	0.825
RCN8		0.200	0.027	0.180
RCN9	0.720	0.026	0.001	0.029
RCN10	0.331	0.174	0.000	0.001

P-value 0 0.05 ns

Figure 7

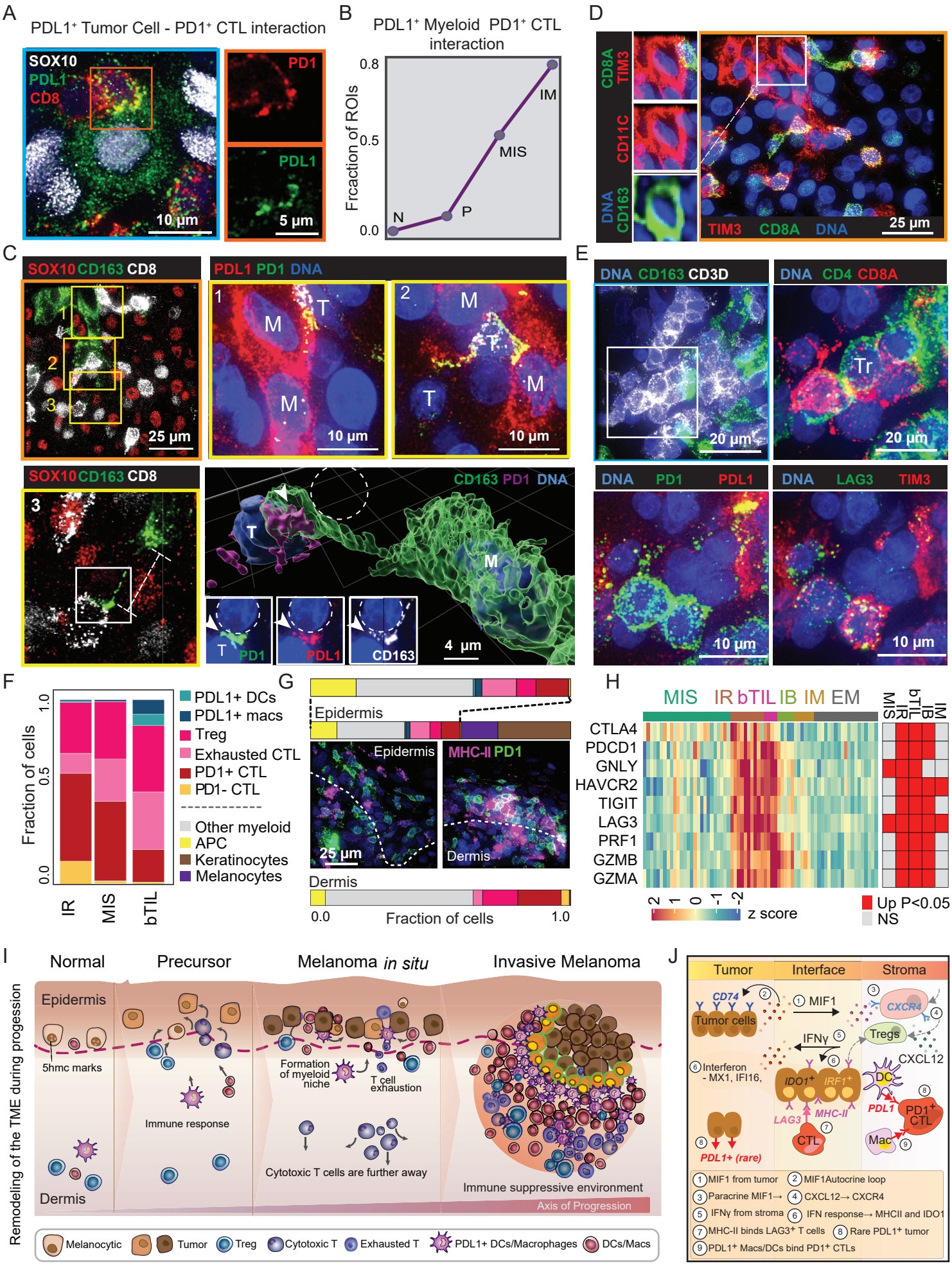

Figure S7